The Interactions of Graphene Oxide with Biological and Artificial Cell Membranes

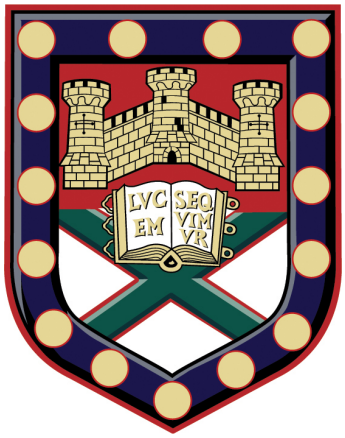

Submitted By

Lauren A. Denton

Ph.D. in Physics

University of Exeter

September 2016

Submitted by Lauren Denton to the University of Exeter as a thesis for the degree of Doctor of Philosophy in Physics in Sept 2016.

I certify that all material in the thesis which is not my own work has been identified and that no material has previously been submitted and approved for the award of a degree by this or any other University.

Signature: …….. (Lauren Denton)

ABSTRACT

Graphene is an atomically thin carbon nanomaterial, with a honeycomb structure. It has generated enormous scientific interest since its discovery in 2004. Graphene has a set of unique properties, which has made it a highly suitable material for the potential use in electronic devices, photonics and bioapplications, including the use in a new generation of biosensors, over the past few years. Graphene has already demonstrated high sensitivity to various biological molecules which come into contact with its surface. However, there have been virtually no studies of the mechanisms of the interactions between graphene and biological materials, particularly the cell membrane, the biological component which will be in direct contact with graphene. Understanding these interactions is central to the use of graphene-based materials in drug delivery systems and its biological safety and is also relevant to the development of many types of biosensors.

The work presented in this thesis provides an insight into the fundamental interactions between graphene oxide (GO), and graphene-based materials, with the cell membrane. By using model membrane systems, the aim is to reveal how GO interacts with cell membranes, the extent to which it affects the structure of the membrane, with the potential to further research the biological processes that occur at the membrane. Studies on Langmuir monolayers, using lipid mixtures representative of the composition of the inner and outer leaflets of a typical cell membrane, found that the nature of GO interaction with biological membranes may be dependent on the lipid composition, with results suggesting significant repulsive forces between GO and negatively charged phospholipids. The second model membrane system investigated were lipid bilayer vesicles. Two preparations of vesicles were used, one containing only neutral phosphatidylcholine lipids and the other containing two types of neutral lipid, as well as cholesterol and a stabilising molecule. GO was shown to permeate both vesicles without causing complete lysis. This suggests GO interacts specifically with at least one type of neutral lipid molecule within the vesicle bilayer. This is further supported through an investigation into GO interactions with a real cell membrane. In red blood cells (RBC's) the interaction of GO increases membrane

stiffness, but does not cause haemolysis, suggesting that it does not penetrate the biological membrane. This suggests GO is interacting with the outer lipid of the membrane, but it is possible the negatively charged lipids in the inner leaflet of the membrane prevent the GO from entering the cell. The increase in membrane stiffness suggests GO is interacting with the lipids altering the properties of the membrane.

ACKNOWLEDGEMENTS

I would like to thank Dr D. Horsell, Prof. C.P. Winlove, Dr P.G. Petrov, Dr S.J. Green, Dr L. Mahe, Prof A.T.A Jenkins, Dr M. Laabei, Dr N.T. Thet, Dr M. Bokori-Brown, Dr E. Green, D. Colridge, Dr B. Sarri, Dr S. Purushothaman, Dr A. Perry, Dr K. Kurtis, Dr J. Dorney, Dr M. Vardaki, Dr S. Hornett, Dr S. Zanjani-pour, R. Edginton Dr N. Jayakrupakar, Dr B. Gardner, Dr I. Iping Petterson, Dr N. Garrett, L. Clark, L. Fullwood, to all of my family and especially to Lewis.

CONTENTS

LIST OF FIGURES

LIST OF TABLES

LIST OF ABBREVIATIONS

ADE	Area Difference Elasticity
AFM	Atomic Force Microscopy
BAM	Brewster Angle Microscopy
BDD	Boron-Doped Diamond
BSA	Bovine Serum Albumin
CF	Carboxyfluorescein
CHO	Cholesterol
CVD	Chemical Vapour Deposition
DODAB	Dioctadecyldimethylammonium Bromide
DOPC	1,2-Dioleoyl-*sn*-Glycero-3-Phosphocholine
DOTAP	1,2-Dioleoyl-3-Trimethylammonium-Propane (chloride salt)
DPPC	1,2-Dipalmitoyl-*sn*-Glycero-3-Phosphocholine
DPPE	1,2-dipalmitoyl-*sn*-glycero-3-phosphoethanolamine
DSEPC	1,2-Distearoyl-*sn*-Glycero-3-Ethylphosphocholine Chloride
DSPA	1,2-Distearoyl-*sn*-Glycero-3-Phosphate Sodium Salt
DSPC	1,2-Distearoyl-*sn*-Glycero-3-Phosphocholine
FET	Field-Effect Transistor
GIXD	Grazing Incidence X-ray Diffraction
GO	Graphene Oxide
GUV	Giant Unilamellar Vesicle
HEPES	4-(2-Hydroxyethyl)-1-Piperazineethanesulfonic Acid
HOPG	Highly Ordered Pyrolytic Graphite
HPHT	High Pressure High Temperature
ITO	Indium Tin Oxide
LB	Langmuir – Blodgett
LUV	Large Unilamellar Vesicle
MLV	Multilamellar Vesicle
PBS	Phosphate Buffer Solution
PC	Phosphatidylcholine
PE	Phosphatidylethanolamine
PS	Phosphatidylserine

POPC	1-Palmitoyl-2-Oleoyl-*sn*-Glycero-3-Phosphocholine
POPG	1-Palmitoyl-2-Oleoyl-*sn*-Glycero-3-Phospho-(1'-*rac*-Glycerol)
RBC	Red Blood Cell
rGO	Reduced Graphene Oxide
ROS	Reactive Oxygen Species
SEM	Scanning Electron Microscopy
SM	Sphingomyelin
SUV	Small Unilamellar Vesicle
TCDA	10, 12-Tricosadiynoic Acid

OVERVIEW OF THESIS

Chapter 1 introduces graphene, explaining the important properties relevant to understand its biological applications, the different sources of graphene and allotropes of carbon. The biological cell membrane structure and properties will be described. Previous literature investigating the interactions of graphene with biological cells is presented, including the different effects of graphene reported, with an introduction to graphene biosensors, identifying where there are gaps in the previous research. There are three main experiments [Chapters 2 – 4] conducted in this thesis which were chosen to provide complementary results in this research.

Chapter 2 describes studies on the interaction of graphene with lipid monolayers, providing structural information about how graphene oxide interacts with mixed-lipid monolayers, mimicking the lipid composition of the inner and outer leaflet of the cell membrane. The aims are to determine the mechanisms of the cell interactions using a Langmuir trough, and also to prepare Langmuir Blodgett films for biosensor applications.

Chapter 3 investigates the permeability of graphene oxide with model bilayer membranes, using two preparations of bilayer vesicles. Optical density measurements and fluorescence techniques are used to measure permeability changes to the bilayer.

Chapter 4 extends this study to a real cell membrane, that of the red blood cell. In addition to fluctuation spectroscopy, haemoglobin absorbance is investigated, as well as using Raman spectroscopy to determine the location of graphene oxide within the cell.

Chapter 5 concludes the work and includes suggestions for future experiments that can resolve some of the inconclusive results within our work such as GO biocompatibility.

Chapter 1 Background

1.1 Properties of Graphene

Graphene is one atom thick, planar sp^2-bonded carbon honeycomb crystal. Each carbon atom is bound to three neighbouring carbons, with a bond length of 1.42 Å, and all bond angles at 120° (1) (2) [Figure 1.1]. Graphene has two structural regions: the basal plane, and the edge. Edges form from breaks in the graphene structure, leaving a one-atom thick line of carbon atoms with dangling bonds that can be utilised for functionalisation of graphene.

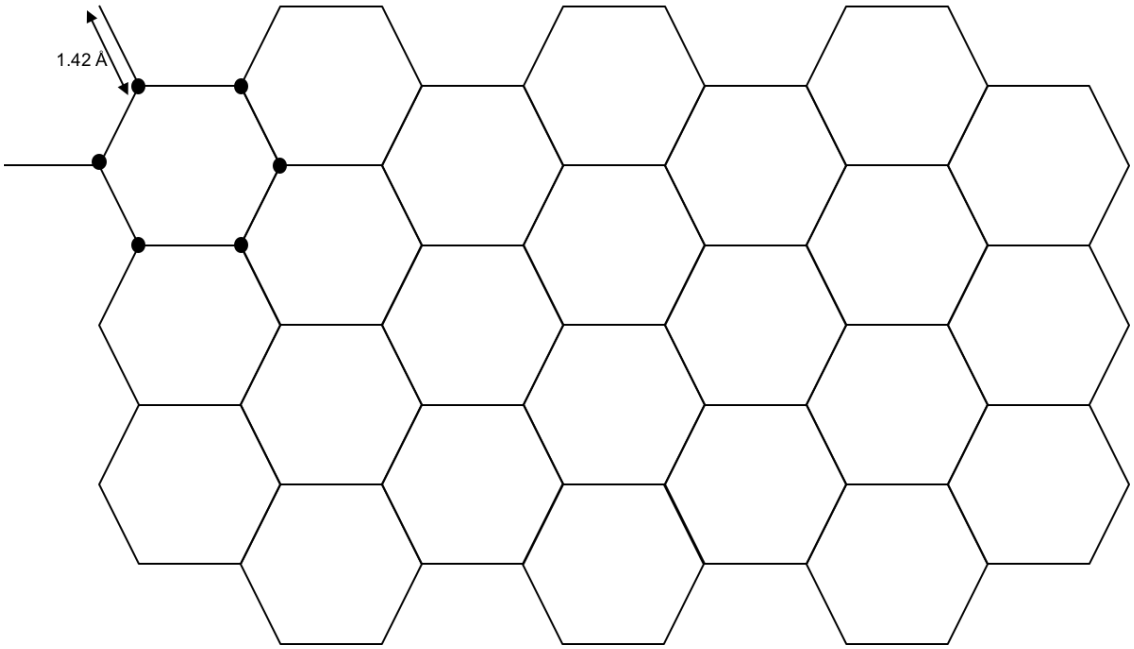

Figure 1.1 Polyaromatic honeycomb structure of graphene

Graphene, known theoretically since 1947, was first isolated in 2004 by Andre Geim and Konstantin Novoselov (3), for which they won the Nobel Prize in Physics in 2010. Since then, graphene has generated a lot of attention due to its many interesting and exciting properties, reviewed by Geim and Novoselov (4), and its use in applications in many different fields such as: condensed matter and

high–energy Physics (5) (6) (7), material science (8) (9), electronics (10) and many bioapplications including biosensing (11) (12).

Its unusual properties make it a unique material to consider when looking at potential applications in the biomedical field. It is chemically inert so cannot be destroyed by solvents or acids. It is electrically conductive so can be used as a sensing surface either as an electrode for electrochemical sensing, or as the conductive channel of a field-effect transistor. It also exhibits high optical transparency.

The mechanical properties of graphene are important when considering its potential to be integrated into flexible sensing platforms and when interacting with biological cells. The mechanical properties of monolayer graphene have been measured, finding the strength to be 130 GPa and a high Young's modulus of 1.0 $\pm$ 0.1 TPa (13). This compares to chemically modified graphene (obtained by reducing GO using a hydrogen plasma) which has been reported to have a Young's modulus of 0.25 $\pm$ 0.15 TPa (14). The Young's modulus, otherwise known as the elastic modulus, measures the resistance of a material to elastic deformation. The high Young's modulus calculated for graphene is indicative of a flexible material. However, mechanical properties can be influenced by surface defects such as overlapped grain boundaries, pinhole and microcracks, with several papers reporting the behaviour of graphene with such defects (15) (16). One simple defect of graphene is caused by missing carbon atoms within the honeycomb lattice. If many carbon atoms are missing the graphene could become energetically unstable. If an odd number of atoms are missing dangling bonds will be present within the graphene structure, leaving the graphene more unstable and reactive. The strong reactivity can weaken the mechanical stability of the graphene (15). As well as high flexibility, graphene also has a large surface to volume ratio, the importance of which will be explained in Section 1.5.1.

The wettability of the surface of graphene is important in determining its biocompatibility. Graphene is reported to be hydrophobic (17) determined by wetting graphene films and measuring the contact angle of the droplet [Figure 1.2]

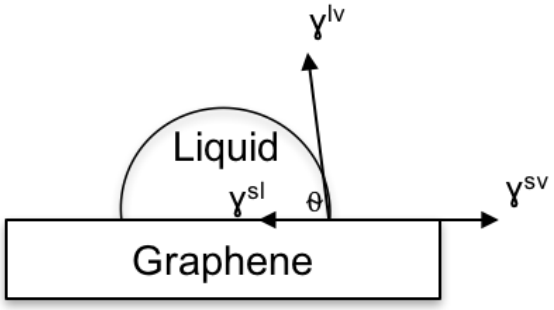

Figure 1.2 Water droplet on the surface of graphene. The contact angle θ is used to determine the wettability.

described by Young's equation,

$$\gamma^{sv} = \gamma^{sl} + \gamma^{lv} \cos\theta \tag{1.1}$$

where θ is the contact angle, γ^{sl} is the solid/liquid interfacial free energy, γ^{sv} is the solid surface free energy and γ^{lv} is the liquid surface free energy. These terms collectively represent the surface tension between the liquid and solid surface measuring the hydrophobic forces (18). The contact angle of water on graphene has been calculated to be approximately 100°, making graphene more hydrophobic than graphite, which has a contact angle of ~ 90° (17). Factors that can affect the water contact angle include physical roughness of the surface or topology, contaminants on the surface, and chemical functionalisation. Because of the structure of graphene, it is possible to manipulate its wettability through functionalisation of the surface for specific applications. For example, Schneider *et al.* assembled a pyrene ethylene glycol monolayer on the surface of graphene, forming a hydrophilic surface, preventing DNA from adsorbing to the graphene through π-π interactions, allowing graphene nanopores to detect single-stranded DNA using the ion current passing through the pore (19). The wettability is an important property when considering the biocompatibility of graphene. Due to its hydrophobicity, it proves difficult to obtain stable aqueous dispersions of graphene, and this could potentially limit its use in biological applications. In this thesis, graphene oxide [Section 1.2.3], will be investigated due to its hydrophilic nature.

Another interesting property of graphene is the ability to tailor the chemical reactivity of the surface. The electronic structure of graphene is the basis of its

chemical properties. Manipulating the surface chemistry for a specific application is of great importance since the chemical composition impacts the electronic structure, as well as the chemical reactivity. As previously mentioned, graphene is chemically inert. This is due to its giant stabilised delocalised π bonding system, where 6 unpaired π-electrons are shared between the 6 carbon atoms of the ring creating regions of electron density above and below the plane of the ring.

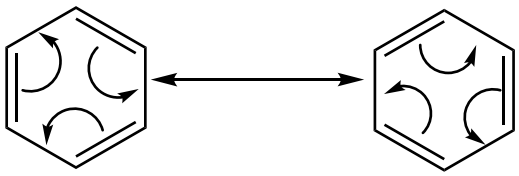

Shown below are the remaining p orbitals (the other orbitals involved in sp^2 hybridisation), one on each carbon atom, which overlap to generate 6 molecular orbitals.

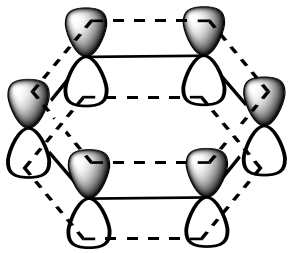

This structure allows for functionalisation of graphene through π-π interactions which occurs with other aromatic molecules above or below the benzene plane, where p orbitals can also overlap, generating an attractive force. Other π-interactions can occur such as metal-π interactions where there is a non-covalent interaction with the region of electron densities, and polar-π interactions. Although, defects within the graphene plane can alter the electronic structure, changing the chemical properties. One common reaction that alters graphene properties is the oxidation of graphene to graphene oxide, which will be described in the next section.

Graphene can be prepared through several different methods. The different methods can be broadly categorised into sections described below. For further detail on graphene preparation see the review paper “A Roadmap for Graphene” (20).

1.2 Preparation of Graphene

1.2.1 Exfoliated and CVD Graphene

Geim and Novoselov (3) initially used the mechanical exfoliation technique in order to obtain single layer graphene. This is achieved by peeling layers of graphene away from a block of graphite using scotch tape. It is more likely that thin graphite stacks are pulled away from the bulk graphite, so it requires multiple exfoliation steps to achieve single layer graphene. The single layer graphene on the tape can then be transferred to a solid substrate, where optical microscopy is required to identify the single layers, by locating the flakes and measuring the optical contrast between the flake and the substrate. This method can produce single-layer graphene as well as a range of multi-layers. Further analysis of the graphene flakes via atomic force microscopy (AFM), for example, can be used to measure the thickness of the flakes through height profiles of the samples. This process gives samples with the best electronic and optical properties, however, the size of the flakes produced are not suitable for large scale applications.

The next method for preparing graphene samples involves the growth of graphene via chemical vapour deposition (CVD) on a metal substrate such as nickel or copper, from carbon-containing gases. It can be used to form mono- or multilayer graphene sheets. For many applications, CVD graphene must be transferred to an insulating substrate. However, this transfer process can cause structural defects, impurities and tearing, which affect the physical properties of graphene. This method has already been shown to produce graphene on a meter-scale (21), but is of a poorer quality compared to exfoliated graphene. It can also be expensive to produce CVD graphene on this larger scale due to a large consumption in energy (20).

1.2.2 Graphene Oxide and Reduced Graphene Oxide

Graphene is naturally hydrophobic, meaning it is non-dispersible in water. However, when oxidised it forms graphene oxide (GO) which is hydrophilic and easily dispersible in water [Figure 1.3].

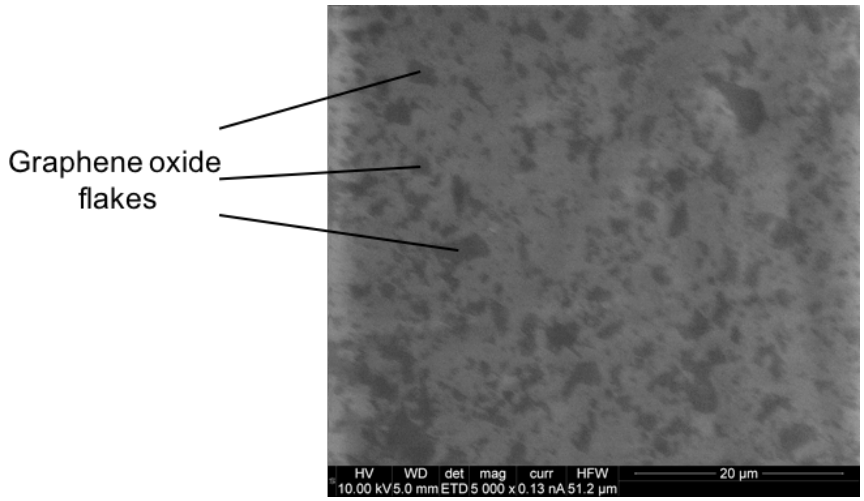

Figure 1.3 SEM image of graphene oxide flakes. 1 mg/ml graphene oxide was dispersed in water and sonicated for 1h, then centrifuged at 10,000 rpm for 10 min.

Due to the polar oxygen-containing groups on the GO surface (hydroxyl, epoxy and carboxyl functional groups), hydrogen bond formation can take place between the GO and water, forming stable GO suspensions. GO is usually prepared using a method based on the proposed method by Hummers and Offeman, which produces GO through the treatment of graphite flakes with potassium permanganate, sodium nitrate and sulfuric acid, at temperatures below 45°C (22). Oxidation of graphene breaks the network of conjugated bonds, and delocalised π-electrons. This renders GO insulating as the conductivity of graphene relies on its continuous sp^2 carbon network. GO sheets are also atomically rough due to this functionalisation. Mkhoyan *et al*. also found that the degree of oxidation fluctuates at the nanometre-scale (23).

GO has been described as a random distribution of oxidised areas with oxygen-containing functional groups, combined with non-oxidised regions where most of carbon atoms preserve sp^2 hybridisation (24). However, the precise structure of GO is still unclear, with several proposed structural models (25) (26) (27). The widely accepted model is that of Lerf and Klinowski (26) (27), with the

hydroxyl, epoxy, and carboxyl groups covering the GO plane and edges. The reactive functional groups of graphene oxide make it a good candidate for use in many applications through chemical functionalisation.

Graphene oxide sheets can be reduced to graphene, known as reduced graphene oxide (rGO). A variety of chemical methods can be used to reduce graphene oxide, the most common uses hydrazine monohydrate (24). Reducing graphene oxide with strong reducing agents, such as lithium aluminium hydride, is challenging due to possible side-reactions with the solvents graphene oxide is dispersed in. The reduction of GO aims to remove all oxygen-containing groups and other defects, as well as restoring the π-bond network to recover some of the important graphene properties, including its electrical conductivity. Different reduction processes will restore the graphene structure and properties to different extents, affecting the final properties of the rGO, usually only resulting in partial reduction. This method leaves the graphene with structural defects; however, this could be advantageous for electrochemical applications as it has been shown that the electrochemistry of graphene occurs at the edges, or at defects in the basal plane (28).

1.3 Allotropes of Carbon

Two other allotropes of carbon have been used in this thesis, highly oriented pyrolytic graphite (HOPG) and diamond [Figure 1.4].

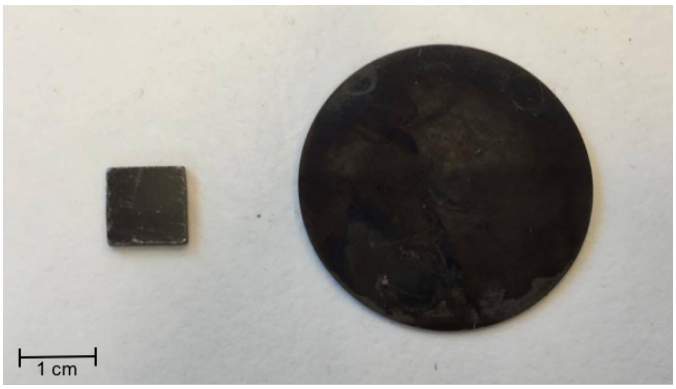

Figure 1.4 Image showing substrates of Highly Oriented Pyrolytic Graphite, HOPG (left), and Boron-Doped Diamond, BDD (deposited on a silicon substrate) (right).

Graphite consists of layers of graphene held together by weak van der Waal's forces, allowing the layers to slide over one another and thereby making graphite a soft material. In contrast, diamond consists of a tetrahedral network of covalently-bonded sp^3 carbon atoms and is one of the hardest natural materials [Figure 1.5].

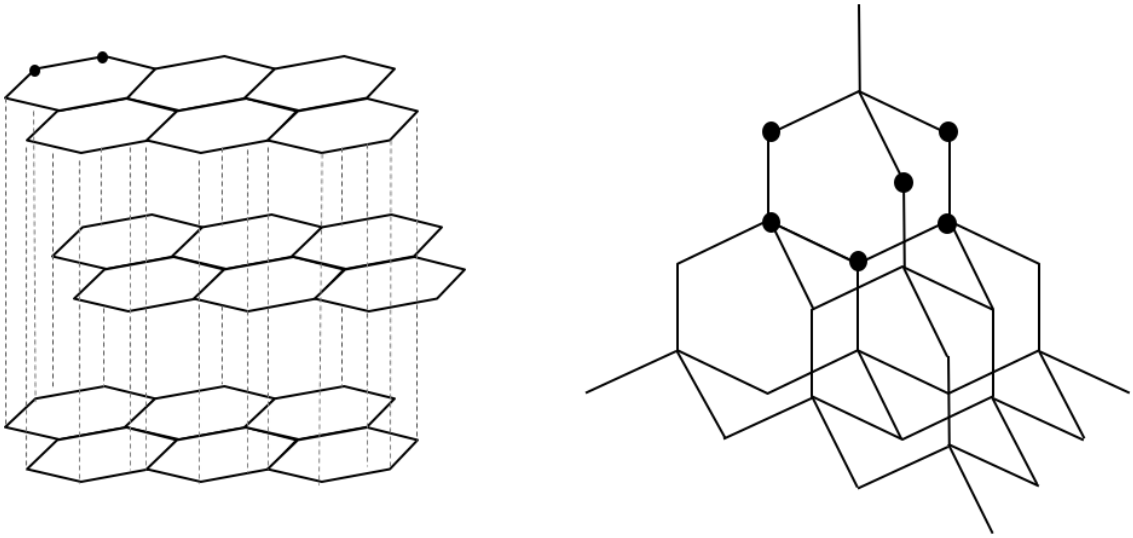

Figure 1.5 The carbon structure of graphite (left) and diamond (right). The graphite is formed from atomically thin sp^2 graphene layers held together by van der Waal's forces, indicated by the dotted lines. Diamond is a covalent tetrahedral structure of sp^3 carbon atoms.

Natural graphite exhibits a lot of defects. HOPG is a highly pure and ordered form of graphite. It is synthesised using a technique called pyrolysis, by heat treatment of pyrolytic carbon. It is characterised by a mosaic spread angle, describing the alignment of the graphite crystals. A low mosaic spread is indicative of a well aligned sample. When synthesising HOPG, additional tensile stress is applied in the basal plane to improve alignment of the crystals. Because of its layered structure, HOPG can be cleaved by pressing tape onto the surface then pulling it off taking a thin layer of HOPG leaving a clean surface that is atomically smooth and highly stable. HOPG is a conductive material, with its conductivity determined by the quality of the HOPG surface. With an increase in defects on the surface, a decrease in conductivity is observed (29), showing the need for a planar surface. Like graphene, HOPG is also reported to be hydrophobic. Kozbial *et al.* found a contact angle of 64.4 $\pm$ 2.9°. Hydrophobicity is said to increase due to contamination from hydrocarbons adsorbing to the surface (30). Graphene films have also shown the ability to tailor its surface to achieve superhydrophobicity (contact angle ~ 160°) by sonicating in acetone, and superhydophilicity (contact angle ~ 10°) by sonicating in water (31).

The electrochemical properties of HOPG have been of great interest, particularly when looking at similarities and differences between the

electrochemistry of HOPG and graphene, as they share the same basic carbon structure. HOPG is also a frequently used source for exfoliated graphene. Further knowledge of the electrochemical properties of HOPG will give an understanding of a variety of processes such as carbon surface functionalisation (32) and electrocatalysis (33). The basal plane of HOPG has already been used as an electrode support for various applications (34) (35), including biosensing [Section 1.5.2], but there have been conflicting reports on the electrochemistry of the basal surface. Until recently, it was generally thought that the basal plane had very low activity (36), with the step edges present across the HOPG surface providing all the electron transfer sites. A thorough study of the electrochemical properties of HOPG was conducted by Patel *et al.* using different grades of HOPG and varying in step-edge height and coverage. They found the same electrochemical behaviour on all substrates and fast electron transfer on the pristine basal plane (37).

For this thesis, the diamond used is doped with boron. The properties of boron-doped diamond (BDD) are determined by the chemical quality of the surface, the level of boron-doping and its physical structure. Diamond itself is insulating, but when doped with boron will become conductive. Boron is the most widely used dopant, due to its low charge carrier activation energy of 0.37 eV (38). Boron films are usually prepared via chemical vapour deposition or the high pressure, high temperature (HPHT) process, where some of the carbon atoms in the diamond structure are substituted with boron, which gives the diamond electrical conductivity. Boron is introduced to the diamond through boron-containing substances such as diborane or trimethylborane. Low doping levels gives the diamond p-type semi-conductor properties (39) (40) whereas at high levels it acts as a semi-metal. This differs from other dopants such as phosphorus or nitrogen which produce n-type semiconductors. The general observation from previous work is that the conductivity of BDD is strongly dependent on the doping level. An increase in crystal imperfections has also been observed from boron-doping (41). High quality BDD has also shown excellent electrochemical properties, which allows it to be used as an electrode in a range of applications (42) (43). Its role in biosensors is described in Section 1.5.2.

The next section introduces the biological cell, describing in detail the structure and properties of the cell membrane. It includes details of all

components of the cell membrane: lipid composition and different classes of lipids and the membrane proteins and cytoskeleton. The mechanical properties of the cell membrane will also be explained. A review of the previous research investigating the interaction of graphene with biological cells is also given.

1.4 The Biological Cell

Biological cells, discovered by Robert Hooke in 1665, form the basic functional and structural unit of all biological organisms [Figure 1.6].

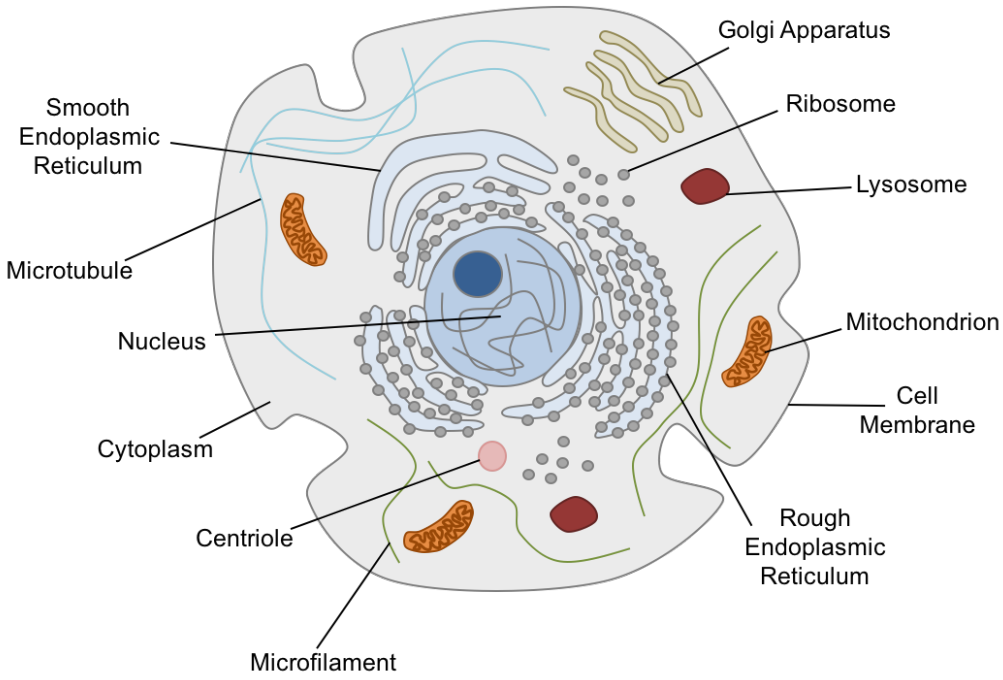

Figure 1.6 Diagram of a 2-dimensional eukaryotic cell, showing the different organelles present within a typical cell.

The adaptation of cells has led to many types of cells with different functional roles working in many different environments. The most important cellular structure for the work of this thesis is the cell membrane, which is relatively similar in structure in all cells.

1.4.1 The Cell Membrane

The cell plasma membrane, forming its external surface, is one of the main components of all biological cells. Organelles in eukaryotic cells are also bound by membranes of similar structure. Many of the cell's important activities occur at the cell membrane, or involve highly specific transport processes through it. The cell membrane acts as a mechanical and chemical barrier between the inside of the cell, and its surroundings. It controls what can pass into the cell, and prevents the diffusion of other molecules. The other functions of the cell membrane include: the sorting and transportation of molecules; recognition; transmission and transduction of signals; and expression of genetic identity. There is great diversity in molecular composition and organisation of biological membranes, specific to these different functions.

1.4.2 The Structure of Biological Cell Membranes

A typical cell membrane consists of a lipid bilayer stabilised by hydrophobic interactions, which may be coupled on its inner surface to a protein network known as the cytoskeleton. Within the lipid bilayer, there are various types of proteins embedded, with a range of functions, some of which are anchored to the cytoskeleton providing mechanical support for the cell [Figure 1.7].

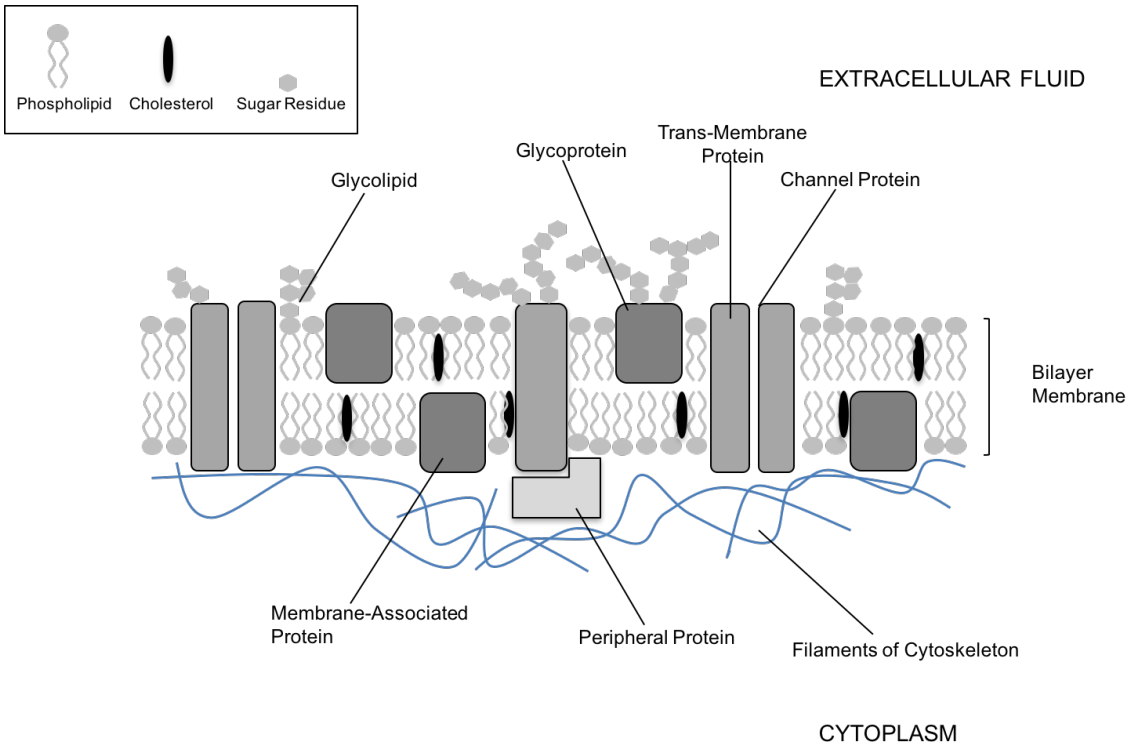

Figure 1.7 A typical biological membrane structure. The membrane is formed of a phospholipid bilayer, also containing other lipid molecules such as cholesterol. Examples of the different phospholipid structures are given in Figure 1.8. There are also various proteins serving different structural and physiological functions. Some of the integrated proteins act as attachment points for the cytoskeleton protein network.

1.4.3 The Phospholipid Bilayer

Cell membranes have complex lipid compositions varying between cells, depending on their purpose. The phospholipids are the most abundant lipid in most cell membranes. They are amphiphilic molecules, consisting of a hydrophilic head group, and hydrophobic fatty acid chains [Figure 1.8].

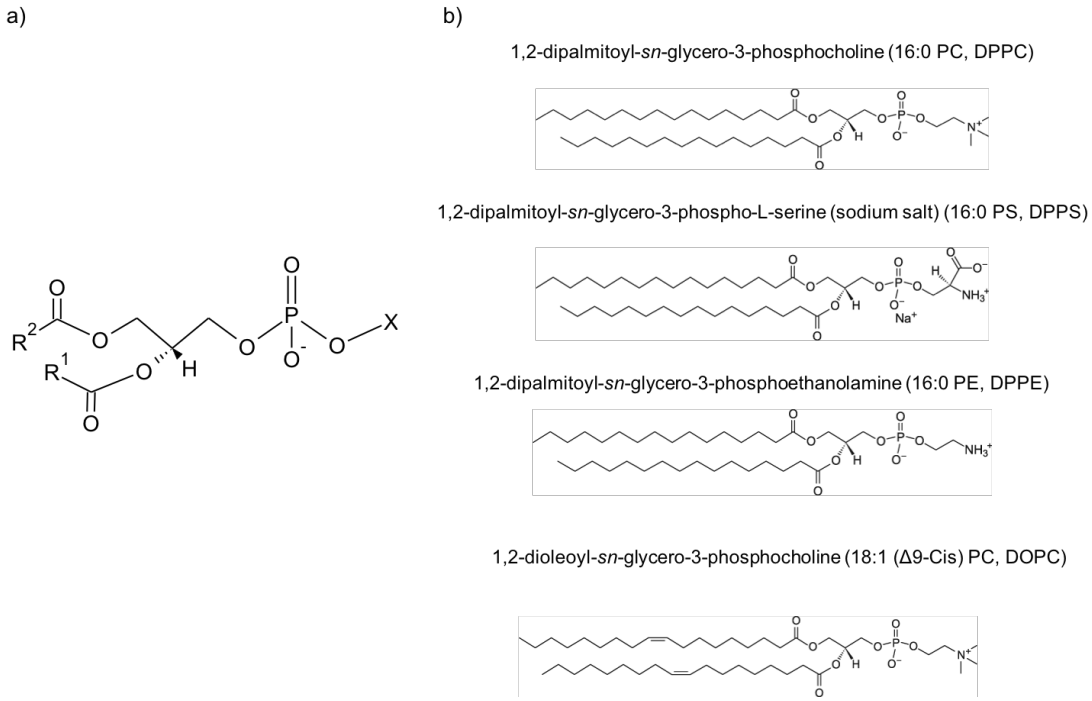

Figure 1.8 a) Basic structure of a phospholipid. R1 and R2 represent fatty acids, normally containing 12-20 carbons and one or more unsaturated bonds. X represents a more hydrophilic group such as a choline forming the head group b) The full structures of the primary phospholipids used in this thesis (from Avanti Polar Lipids, Inc. *(44)*).

Phospholipid bilayers spontaneously form due to the hydrophobic interactions of the lipid tails, forming a barrier between the inside of the cell, and the outside. They arrange so that the hydrophilic head groups are on the inside and outside of the cell, with a hydrophobic region in between, minimising the interactions between the hydrophobic tails and the surrounding water molecules. Phospholipids consist of a phosphate head group, containing either a glycerol or sphingosine base, and two fatty acid chains. Phospholipids are characterised by their head group and, also, by the number, length and degree of saturation of the fatty acid chains. The primary head groups include choline, serine, glycerol, ethanolamine, inositol and phosphatic acid. For example, a commonly used phospholipid 16:0 PC (1,2-dipalmitoyl-*sn*-glycero-3-phosphocholine or DPPC) has a choline head group, attached to two identical 16-carbon saturated fatty acid chains [Figure 1.8]. The size of the lipid head group and the degree of saturation of the fatty acid chains will affect their packing within the membrane and influence the curvature of the membrane.

Lipid systems can form a variety of two-dimensional phases, from gaseous to solid. They can undergo temperature-dependent phase transitions and the temperature at which these occur is specific to each lipid species. The phospholipid bilayer is generally described as a 2-dimensional liquid. This is because the lipids are free to move around on the 2-dimensional surface of the membrane. However, this picture is complicated by the proteins associated with the membrane and by formation of lipid domains (45) and lipid rafts (46) within the membrane.

In 1972, Singer and Nicholson proposed the fluid-mosaic model demonstrating the membrane structure, giving evidence of the organisation of lipids and proteins within the membrane based on thermodynamic analysis of the hydrophobic interactions. The molecules organise into a structure that gives the lowest free energy (47) [Figure 1.9].

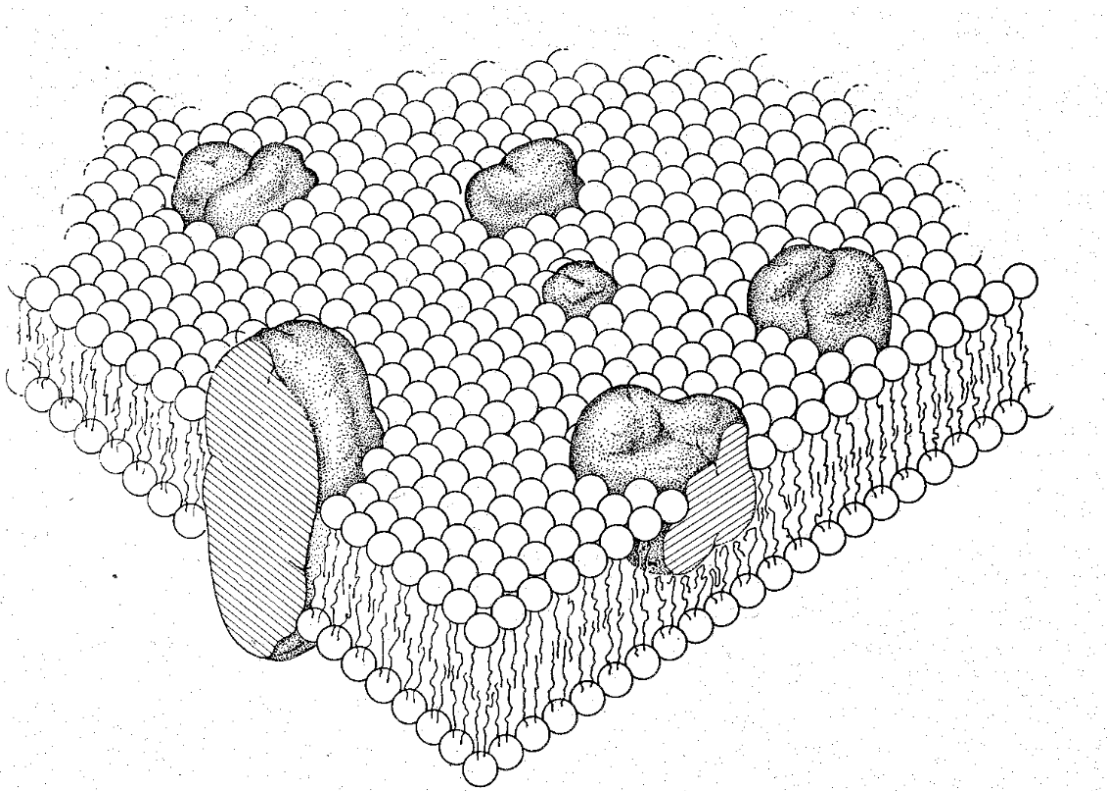

Figure 1.9 The Fluid Mosaic Model as proposed by Singer and Nicholson showing the phospholipid bilayer with embedded membrane proteins (from *(47)*).

The cell membrane is asymmetrical (48) (49) (50) with different lipids distributed in the two halves of the bilayer. The asymmetrical distribution of lipids

is fundamental to many cellular processes. The two different monolayers are known as the inner and outer leaflet of the membrane. For example, the membrane of human erythrocytes contains almost all the sphingomyelin [Section 1.4.5] and PC in its outer leaflet. Lipids with neutral or negatively charged head groups are found in the inner leaflet. The membrane actively maintains this lipid asymmetry, as well as the asymmetry between proteins and other structures.

1.4.4 Other Membrane Lipids

Although the phospholipids are the most abundant lipid in the cell membrane, there are other lipids that contribute to the membrane. Cholesterol is a lipid molecule also found in cell membranes, differing in percentage between membranes (~ 30-50 mol%). It is defined as amphipathic, containing a hydrophilic region and a lipophilic region. Due to the structure of cholesterol [Figure 1.10], it is classed as a sterol, with the network of hydrocarbon rings being a signature to all steroid hormones and a short hydrocarbon chain that easily intercalates into the lipid bilayer. It is a vital component of cell membranes and is also used by cell to synthesise other steroids.

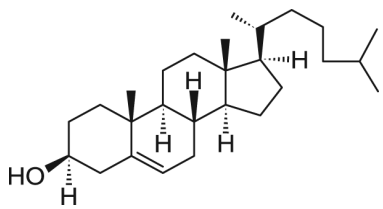

Figure 1.10 The molecular structure of Cholesterol, one of the membrane lipids (from Avanti Polar Lipids, Inc. *(44)***).**

Cholesterol decreases the permeability of the membrane by increasing the hydrophobicity of the barrier to polar molecules and also helps strengthen the bilayer. It is also important for the formation of domains within biological membranes. Cholesterol intercalates between acyl chains of phospho- and glyco-lipids in the membrane, resulting in a decrease in area per molecule that may promote phase separation within the bilayer, favouring interactions with saturated

chains. Cholesterol is able to move rapidly between the different leaflets of the membrane, due to a lower free-energy barrier compared to phospholipids (51). Cholesterol will also favour interactions with sphingolipids, another lipid molecule found in the cell membrane, which tend to have longer, more saturated hydrocarbon chains. According to the “Umbrella Model” the preferential mixing of cholesterol with sphingolipids is due to shielding of non-polar cholesterol, from the polar sphingolipid head groups (52) (53), as opposed to intermolecular interactions. These interactions further contribute to domain formation.

Sphingolipids are a class of lipids with an amino-alcohol backbone, a polar head group and two non-polar tails. Their basic structure has allowed for vast modification producing a class of lipids with diverse structure and function [Figure 1.11].

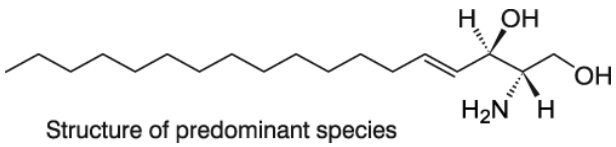

Figure 1.11 The structure of the predominant species, sphingosine, present in all sphingolipids (from Avanti Polar Lipids, Inc. *(44)***).**

Sphingolipids located in the cell membrane play important roles in the structure of the membrane, in signal transmission and cell recognition, as well as serving as adhesion sites for extracellular proteins.

1.4.5 Lipid Bilayer Mechanics

The mechanical properties of a cell membrane influence the structure and function of the cell. Characterising these mechanical properties provides an insight into the physiological state of the membrane, important for studying the effects of disease or administration of drugs, for example. In the context of this thesis, they are likely to influence the interaction of the membrane with graphene. The mechanical properties of a thin membrane are described as one of three types of deformation: in-plane extension at a constant area (shear), bending or curvature change, and area expansion (stretching) (54) [Figure 1.12].

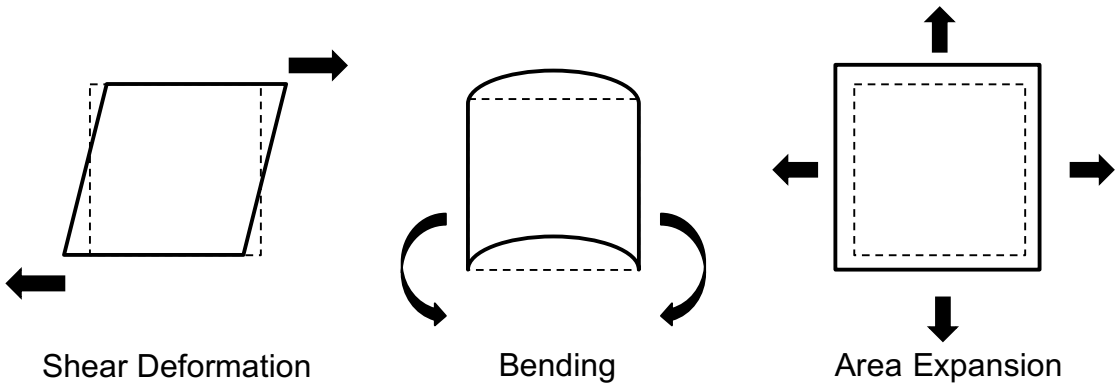

Figure 1.12 The deformations of a 2-D membrane: shear, bending and area expansion.

There are two widely used models used to investigate membrane elasticity. They are giant vesicles and the red blood cell (RBC), which consists of a representative cell membrane encapsulating a haemoglobin solution. Giant vesicles have a low bending modulus and a shear modulus close to zero, whereas the RBC membrane is supported by the cytoskeleton, increasing both moduli, producing a more rigid membrane. A detailed explanation of this will be given in Chapter 4.

1.4.6 Lipid Monolayers

Much of our understanding of the physical properties of membranes has emerged from studies on lipid monolayers. They form readily at air-liquid and liquid-liquid interfaces due to the amphiphilic nature of the molecules, which self-organise in one phase or another. Work on these monolayers relevant to this project is reviewed in Chapter 2. Because the phospholipid bilayer of the cell membrane can be considered as two weakly interacting monolayers, the phase behaviour of lipid monolayers can be loosely used to describe that of lipid bilayers. However, other factors within the bilayer can also contribute to changes in phase and must be considered. These considerations include: stresses induced by membrane curvature, as well as curvature driven phase separation and curvature induced by changes in lipid composition, and lipid ‘flip-flop’, where lipids can move from one leaflet of the bilayer to another.

Although there are difficulties in accurately comparing the properties of monolayers and bilayers, the monolayer is an important tool in research. Monolayer systems can be used to measure various phase transitions of pure phospholipids and more complex lipid systems, further described in Chapter 2. In biological membranes these transitions are important to understand, since the properties of a membrane can change dramatically.

1.4.7 Membrane Proteins and the Cytoskeleton

Within the cell membrane there are various types of proteins, with various different functions, that also contain hydrophobic and hydrophilic regions, like the phospholipids. This allows for proteins to interact with the membrane, whether they are able to sit inside the membrane or attach to the outside of the membrane, with parts anchored into the cell. Integral (trans-membrane) proteins have hydrophobic domains which span the phospholipid bilayer, whereas peripheral (membrane-associated) proteins have smaller domains which intercalate in only one half of the bilayer [Figure 1.6]. These proteins are generally involved in cell-cell signalling. Integral proteins may form domains within the membrane, some form channels or pores to assist in transporting molecules in and out of the cell, usually specific to the type of ion or solute. Other integral channel proteins use active transport to move molecules in and out of the cell against concentration gradients.

The proteins that are most important to cell membrane mechanics are those that are attached to the cytoskeleton. The cytoskeleton is the network of proteins surrounding the cell, providing structural support, as well as having important roles in cell mitosis and meiosis, intracellular transport of cell organelles and the transduction of chemical and physical signals into the cell.

1.4.8 Graphene Interacting with Biological Cells

This main aim of the work in this thesis is to investigate the interactions between graphene and biological cells. Initial research has already been carried

out investigating the antibacterial properties of graphene (55) (56) (57). Akhavan and Ghaderi found bacterial cell membrane damage through direct contact of the sharp edges of graphene nanowalls and the bacteria, showing reduced graphene oxide to be more toxic than graphene oxide (55). Hu *et al*. (56) reported graphene and graphene oxide solutions effectively inhibit bacterial growth as well as severe membrane damage to *E. coli* cells, with GO exhibiting a slightly stronger antibacterial effect. It was suggested the cause of damage was due to oxidative stress, caused by a disturbance in the balance between the production of reactive oxygen species (ROS) and the cells antioxidant defences (58), or by physical damage. They also demonstrated cellular uptake of graphene oxide in a mammalian cell line, A549, a human lung carcinoma epithelial cell line, finding graphene oxide inside the endosome of the cytoplasm, suggesting internalisation via endocytosis with minimal cytotoxicity (56). rGO exhibited significantly higher cytotoxicity. Krishnamoorthy *et al.* agree, generally, with previously reported mechanisms of toxicity. However, they also present results suggesting graphene specifically disrupts the outer membrane of the bacteria, leading to cell death (57). It is important to consider the interactions of these graphene-based materials with bacteria, however, as already shown by Hu *et al.*, it is possible graphene will interact differently when in contact with mammalian cells, due to structural and functional differences.

Reports of toxicity of graphene oxide towards mammalian cells have also been presented. Chang *et al.* investigated the toxicity of graphene oxide towards A549 cells finding graphene oxide did not enter the cells, nor exhibit cytotoxicity towards the cell. However, at high concentrations, graphene oxide only induces slight loss in cell viability, concluding graphene oxide to be a safe material at the cellular level (59). There has also been research conducted investigating the toxicity of graphene oxide towards human erythrocytes, the red blood cells. Liao *et al*. showed size and dose-dependent haemolytic activity of graphene oxide. Low haemolytic activity was observed with aggregated graphene sheets (60). By measuring the haemoglobin absorbance, the authors were able to determine the percentage of haemolysis in a cell population, and therefore the toxicity. However, little detail is given on how the graphene is interacting with the cell to cause cell lysis. The differences in observations of toxicity and interactions show the necessity to further investigate the mechanisms of interactions.

Another one of the aims of this research is to understand the interactions of graphene with biomolecules and cells that are relevant to its use in biosensors, which will be discussed in the next section.

1.5 Biosensors

Biosensors are used to detect a range of biologically active molecules, sensitively and selectively. They are of great importance in various fields such as security and environmental safety, as well as point-of-care analyses within health care, with a strong demand to produce highly selective and sensitive, cost-effective sensors. Biosensors are devices that use a biological component to detect biological materials, and convert the information into an analytically useful signal. They are constructed from two elements: a receptor and a transducer. The receptor generally consists of a biological component, such as DNA or a protein, which has a specific interaction with another molecule. The receptor is the recognition element of a biosensor. A biological response is induced on recognition of the specific biomolecule. The transducer converts the information into a measurable signal, proportionate to the concentration of the biomolecule [Figure 1.13].

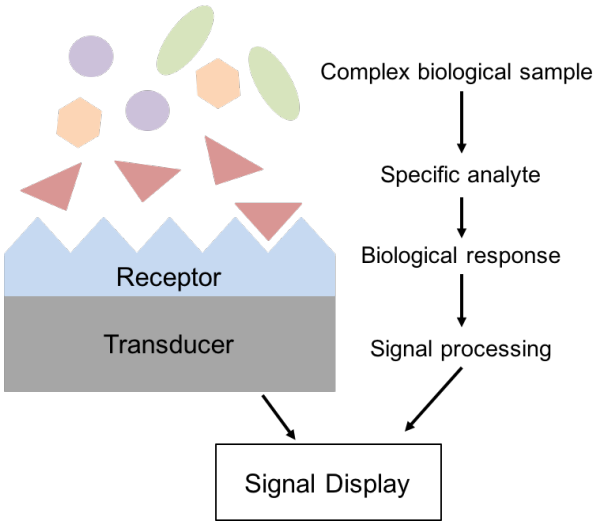

Figure 1.13 An example of a biosensor showing the biological recognition of a specific molecule which activates the receptor to produce a biological response, which is amplified and processed by the transducer to give a readable signal.

1.5.1 Graphene Biosensors

Carbon-based nanomaterials, especially graphene, have attracted a great research interest in the field of biosensing. There have been several review articles published on the use of graphene in biosensing (28) (11) (61). Described here are the important properties of graphene that contribute to its use as a sensing platform, as well as some examples of the different types of biosensor graphene has been used in.

The properties of graphene make it an excellent material for the use in biosensing devices. Graphene flexibility is important for the development of biosensors that are portable, wearable and possibly implantable, such that the final biosensor could be applied to a curved surface, *eg.* a surface on the human body. For graphene to be used in various biosensing systems, the graphene surface may require functionalisation in order to immobilise particular biomolecules, for example, antibodies. Graphene can form covalent bonds, as well as π-π stacking interactions which binds any aromatically linked receptor molecules through non-covalent attractive forces between aromatic rings, which are all advantageous for surface functionalisation allowing a range of molecules

to attach to its surface. Graphene's large surface to volume ratio allows for increased loading of the specific biomolecules to the surface to enhance the sensitivity of the biosensor. As graphene is also electrically conductive and optically transparent, it can be used as an electrochemical, conductive or optical transducer. The combination of these properties gives potential advantages for use of graphene in biosensors.

Field-effect Transistors (FETs) are one type of biosensor that, constructed with graphene, has shown great potential. FETs measure the change in electric charge distribution at the receptor. In an FET, the charge carrier density in the graphene can be controlled by a voltage applied to the transistor gate. Molecules on the surface of the graphene exchange charge with it, with the gate allowing the charge exchange to be measured. Graphene-based FETs have been used in the detection of DNA molecules, due to the charged phosphate backbone of the DNA. Dong *et al*. showed the detection of DNA hybridisation, with single base specificity, by using CVD graphene transistors functionalised with probe-DNA to measure the charge transfer between the DNA and graphene (62).

Electrochemical impedance has been used in biosensing platforms showing high sensitivity. Graphene, functionalised with hairpin-DNA via π-π stacking between the ring of the nucleobase and the graphene, has been used for the detection of DNA hybridisation (63), by measuring electrochemical changes when the DNA hybridises with the complementary target. Electrochemical biosensors are highly sensitive to electroactive molecules, and also highly selective in that different molecules can be oxidised or reduced at different potentials. Electrochemical reactions occur at the interface between the electrolyte solution and the electrode surface. With graphene, electron transfer can occur at the edges or at defects in the basal plane. Graphene's large surface area can facilitate a large number of defect sites, increasing electroactive sites. Graphene has been utilised in many glucose-sensing mechanisms used for diagnoses of diseases such as diabetes. The enzyme glucose oxidase is used as the biorecognition element immobilised on the graphene surface. It oxidises glucose to gluconic acid and hydrogen peroxide, the latter can be directly measured providing useful for glucose detection (2). There have also been developments toward non-enzymatic graphene-glucose biosensors using metal/metal oxide based catalysts. The presence of glucose is determined by the

electrooxidation of glucose to glucolactone caused by the redox reaction of the metal (12). This method has been developed to eliminate several problems which arise when using enzymes (eg. glucose oxidase) including; pH; temperature; humidity and toxic chemicals which could denature the enzyme (64).

Graphene has also been used in fluorescence biosensors due to its ability to quench fluorescence. It has been previously used in the detection of thrombin (65). In this work, graphene was functionalised with an aptamer labelled with a fluorescent dye. Fluorescence recovery was measured when the thrombin attached to the aptamer. As well as biomolecules, graphene has been used to detect whole single cells. Ang, *et al.* have developed a graphene transistor, functionalised with specific biorecognition proteins, integrated with a microfluidic channel, to allow a "flow-catch-release" sequence to detect malaria-infected red blood cells. A change in graphene conductivity indicates an infected cell has been "captured" (66).

Although graphene biosensors have exhibited good sensitivity and selectivity, there are still many challenges to overcome in order to develop consistent and reproducible graphene sensors for large-scale manufacturing, critical for commercialisation. This next section describes two other carbon materials that have also been used as a sensing platform within biosensing devices.

1.5.2 HOPG and BDD Biosensors

In this thesis, HOPG has been used to provide a model for graphene biosensing, as it can be considered as multi-layer graphene. As described in section 1.3, HOPG has advantageous electrochemical properties that can be used in biosensor applications. Like graphene-based biosensors, it is important that specific biomolecules are immobilised on the HOPG surface in order for specific detection. Previously, HOPG, functionalised by π-stacking of pyrene-based linker molecules attached to antibodies, has been used as a label-free electrochemical impedance biosensor to detect the sepsis marker procalcitonin by measuring the charge-transfer resistance between the redox probe, and the HOPG surface (67). HOPG has also been functionalised with pyrene for

immobilising DNA on its surface for use as an electrochemical DNA-sensor (68) (34).

BDD has also been used in this thesis due its great potential as an electrochemical biosensor. BDD biosensors exhibit a low and stable background current which gives improved signal-to-background and signal-to-noise ratio, and a low limit of detection. It also has a wide working potential window. The diamond surface is chemically and mechanically stable resisting severe morphological changes. It also exhibits good electrochemical activity and a fast response time. BDD biosensors have been shown to be highly sensitive and specific, reproducible, as well as exhibiting long-term stability and good biocompatibility (69) (70). They have been used to detect a variety of biomolecules including important neurotransmitters (70).

Chapter 2 Langmuir Monolayer Studies and Langmuir-Blodgett Deposition

In this chapter, I will be discussing experiments carried out looking at the interactions of Langmuir monolayers formed from membrane phospholipids and solutions of graphene oxide. I will also be describing the experimental formation of lipid bilayers onto graphene and other carbon substrates, using both the vesicle fusion method and Langmuir-Blodgett deposition.

The aim of this experiment is first to clarify the mechanisms of interaction between phospholipids and GO to inform later studies on the interactions of GO with cells. A further aim is to establish whether bilayers can be formed on model carbon substrates. Firstly, to determine the arangement of phospholipids on a solid carbon surface and, secondly, whether the bilayers have sufficient integrity for potential use in electrochemical detectors.

2.1 Introduction

2.1.1 Langmuir Monolayers

Langmuir monolayers are widely used for studying the chemical and physical surface properties of insoluble monolayers of amphiphilic molecules at the air-water interface. Primarily, they are used to obtain pressure-area isotherms for lipid monolayers to measure the phase behaviour and dynamics of different lipid systems. They also allow the possibility to generate and control lateral surface pressure in order to appropriately model biological membranes with a surface pressure of ~ 30 - 35 mN/m.

Monolayers have been extensively used to study the physical properties of the individual lipids of the plasma membrane and interactions between them, providing a powerful tool to examine the behaviour and roles of lipids in biological cell membranes. It is important to consider the structural arrangement of the lipid

molecules within the membrane, to understand the different roles of the lipids. There is a great interest, in particular, in investigating the phospholipid systems found in biological membranes. Different lipid compositions will have a preferred molecular packing arrangement, serving specific roles in the function of the membrane such as the mechanical properties, two-dimensional phase behaviour, or the formation of lipid domains and rafts. Evidence suggests the lipids in most biological membranes are in a fluid phase (71), a property vital to many cell processes.

There have been many studies characterising phase behaviour of pure and mixed lipid monolayers using pressure-area isotherms (72) (73), as well as utilising other techniques such as fluorescence microscopy, Brewster angle microscopy (BAM), grazing incidence x-ray diffraction (GIXD) and dipole potential measurements which can be used, for example, to monitor domain formation (74). It is important to note that analysis of mixed lipid monolayers can be complicated due to the presence of lipid domains in equilibrium or non-equilibrium metastable domains. Using microscopy techniques together with the construction of pressure-area isotherms, it is possible to work with lipids extracted from a specific cell membrane, and compare the domain formation of well-characterised pure lipid systems with the complex lipid system of the cell membrane to identify the role of specific lipids in domain formation.

Langmuir monolayers have also been extensively used as a model membrane system to investigate biological reactions in two-dimensions, the effects of proteins and other biomolecules on molecular organisation, viscoelasticity and electrostatic interactions. The first such attempt extracted lipids from erythrocyte ghost cell membranes (cell-like structure consisting of only a membrane), and compared the area of the monolayer to the surface of the ghost cells. This found the monolayer area to be half of the area measured for the ghost cell membrane, suggesting that the cell membrane consists of two monolayers (75). Another excellent example utilising the Langmuir model system was a study of the lipid composition of lung surfactant (76). Lung surfactant is a naturally occurring monolayer with a complex mixture of lipids and proteins, which forms at the air-alveolus interface. The most abundant lipid being DPPC, which is widely agreed as the lipid responsible for the near-zero surface tension at the alveolar surface at the end of exhalation. This is an essential property of the lung

surfactant which increases surface pressure as the alveolar area decreases, thus preventing lung collapse (76). The Langmuir monolayer is able to mimic some of the properties of lung surfactant, such as the ability to lower surface tension, and the re-spreading of lipids during inhalation, aided by a surfactant protein.

Langmuir monolayers have also been used to study the interactions of lipid monolayers with molecules such as proteins added to the subphase below. Importantly, they have been used to investigate interactions of lipids with anticancer drugs for the optimisation of drug delivery (77), as well as the interactions of proteins with brain lipid extracts when investigating neurodegenerative diseases (78).

Another method for studying lipid-protein interactions incorporates the protein with the lipids before monolayer formation. This has been used to understand the aggregation of peptides characteristic of Alzheimer's disease, within a lipid membrane. The peptides investigated include amyloid beta proteins (and amyloid forming proteins) which are produced in the lipid membrane causing neuronal death (79). Adsorption of these peptides into a Langmuir monolayer were studied to determine the nature of the interaction to investigate the mechanism and origin of Alzheimer's disease. They measured surface pressure and surface potential – area isotherms to give information on the interactions between the lipids and peptides. An increase in surface pressure was observed on adsorption of the peptides/proteins indicating attractive forces between the two molecules. Combining this study with other spectroscopic techniques can further characterise the structure of the monolayer and determine the orientation of the lipids of the monolayer to give a greater insight to the mechanisms in which the peptides act within the membrane (80).

In addition to studying lipid monolayers, other amphiphilic molecules that form a monolayer at the air-water interface can be studied. Previous research, for example, has utilised the Langmuir monolayer technique to analyse the surface chemistry properties and structural behaviour of particular enzymes (81) and hormones including insulin using the same characterisation techniques used to study lipid monolayers (82).

2.1.2 Langmuir Trough Construction

The Langmuir trough is shown schematically in Figure 2.1. The trough and barriers are made of a hydrophobic material such as Teflon. The trough is filled with a fluid subphase to produce a meniscus bounded by the trough and the barriers. The barriers are controlled mechanically to allow for accurate adjustment of the trough area.

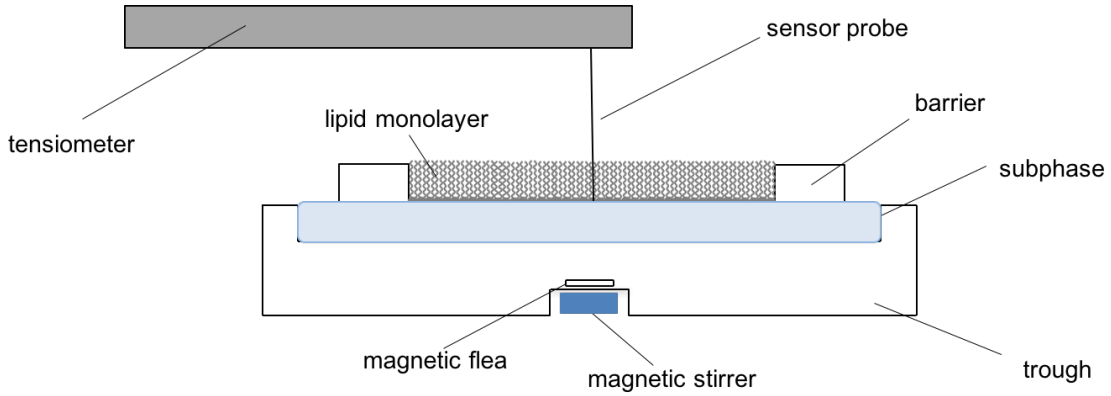

Figure 2.1 The Langmuir Trough. The two moveable barriers are used to adjust the surface area of the trough, and compress and relax the lipid monolayer spread on the liquid subphase. The sensor probe measures the 2-dimensional surface pressure. The magnetic flea and stirrer are used to evenly distribute solutes added to the subphase.

A lipid monolayer is spread over the surface of the subphase between the two barriers, to allow for compression and relaxation of the monolayer. This directly controls the surface concentration (area/molecule). The changes in molecular packing of the lipids during compression are observed by a change in surface pressure (π) Surface pressure is defined as the difference between the surface tension of the pure subphase, and the surface tension of the Langmuir film:

$$\pi = \gamma_0 - \gamma(c) \tag{2.1}$$

where γ_0 is the surface tension of pure water (72.8 mN/m at 20°C), and γ is the surface tension of the film-covered surface, as a function of concentration (c). Surface tension is measured as the downward force on a probe in contact with, but not immersed in, the air-water interface. To eliminate uncertainties arising

from the contact angle of the meniscus at the probe, the probe has to be completely wetted by the surface of the film *i.e.* a contact angle of zero. The surface pressure and trough area are plotted against each other to produce a pressure-area isotherm.

2.1.3 Surface Pressure – Area Isotherms

The lipid phase behaviour of the films is usually characterised by the construction of pressure-area isotherms, in which the area/molecule ($Å^2$) is changed sufficiently slowly to achieve equilibrium at each pressure. The lipid monolayer can exist in different phases and undergo phase transitions. The isotherm shows distinct phase regions with their characteristic gradients. Phase coexistence appears as a plateau in the isotherm, an ideal first order transition [Figure 2.2].

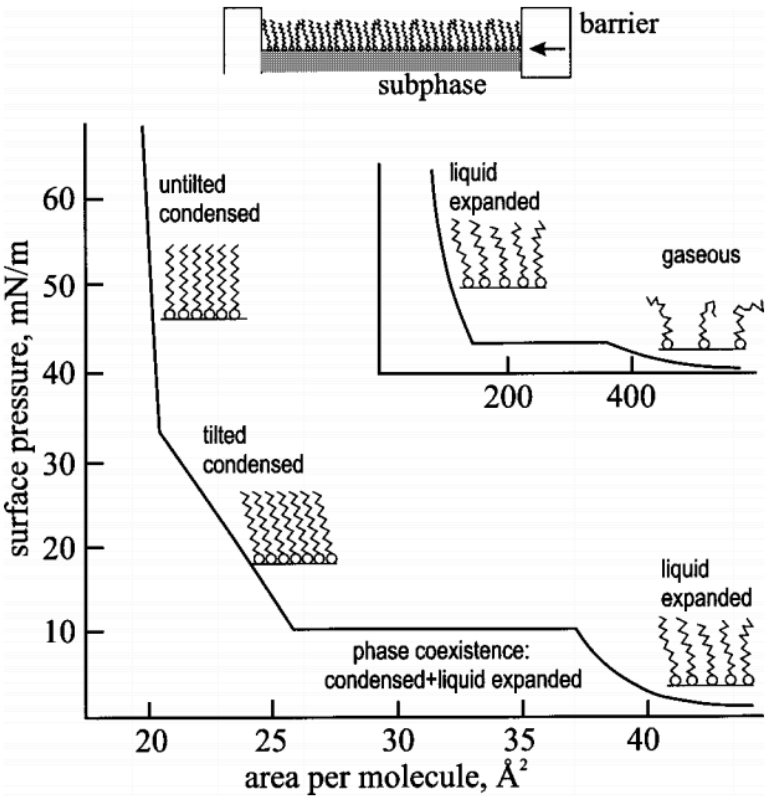

Figure 2.2 A generalised π-A isotherm of a Langmuir monolayer, showing the molecular arrangement of lipids at the distinct phase regions during compression. From *(83)*.

The lipids can exist in phases ranging from gaseous to solid with increasing pressure. At low pressures, the monolayer is said to be in the gaseous phase. Molecules on the surface are widely spread and disordered. Compression of the film triggers a phase transition to the liquid-expanded phase where molecules remain disordered and fluid. Further compression induces another phase transition to the liquid-condensed state, also known as the tilted-condensed state. At higher pressures, the monolayer can reach the untilted-condensed phase (the solid phase). Molecules in the final phases are ordered, with the molecules in the solid phase almost perpendicular to the surface, as opposed to the tilted orientation of the molecules in the liquid-condensed phase. When in the solid phase, further compression can lead to the monolayer collapsing. Molecules are forced out of the monolayer at these high surface pressures and form disordered multilayers on the surface. Changes in the gradient (incremental elastic modulus) in the isotherm indicates a change in phase which are determined by intermolecular interactions including van der Waal's forces between hydrocarbon chains and attractive or repulsive electrostatic or steric interactions between head groups.

The dilational modulus, $\in$, also known as the surface elasticity modulus (84), can be used with the π-A isotherm to give a better understanding of the mechanical properties of the lipid monolayer:

$$\epsilon = \frac{d\gamma}{d\ln A} = \frac{-d\pi}{dA/A} \tag{2.2}$$

It describes the change in surface tension, γ, produced by the corresponding change in surface area, *A,* of the monolayer. A plot of the dilational modulus vs surface pressure can provide further information on the subtle features in the phase behaviour as well as details on the rigidity of the monolayer upon compression (85).

2.1.4 Studying the Interaction of Graphene and Lipids

There has been only a single application of the Langmuir monolayer to the study of graphene interactions with lipids. Shanghao Li, *et al.* investigated interactions between graphene oxide and five lipids with different head groups carrying different charges (Dioctadecyldimethylammonium bromide (DODAB), 1,2-Distearoyl-*sn*-glycero-3-ethylphosphocholine chloride salt (DSEPC), 1,2-distearoyl-*sn*-glycero-3-phosphocholine (DSPC), 1,2-distearoyl-*sn*-glycero-3-phosphate sodium salt (DSPA) and stearic acid). They found that graphene oxide can be incorporated into positively charged monolayers, but not neutral or negatively charged monolayers. This led them to conclude that the cellular uptake of graphene oxide is due to biological processes such as endocytosis, rather than phospholipid interaction, due to a lack of positively charged lipids present in biological membranes (86). However, the cell membrane contains a complex mixture of lipids [Chapter 1] and this conclusion seems premature. An aim of the present work is, therefore, to investigate the interactions of graphene with lipid mixtures representative of those in the inner and outer leaflets of the plasma membrane of a typical cell.

2.1.5 Supported – Lipid Bilayers

Supported-lipid bilayers are another commonly used system to model the cell membrane. Depositing model membranes onto solid substrates allows studies of biological processes that occur at the cellular level, as well as the potential to be used in biosensor applications. Described here are two of the methods proposed to deposit the membranes: the vesicle fusion method and Langmuir-Blodgett (LB) deposition.

In the vesicle fusion method, lipid bilayer vesicles are allowed to adsorb to a solid support when they spontaneously rupture, forming a bilayer on the surface. This method has been used by Tzusuki *et al* (87). They investigated formation of DOPC lipid membranes to determine a structural model in which lipid mono- and bilayers arrange on a reduced graphene oxide support. Their results

suggest that an initial monolayer is deposited onto rGO, but loosely arranged with a tilted orientation [Figure 2.3].

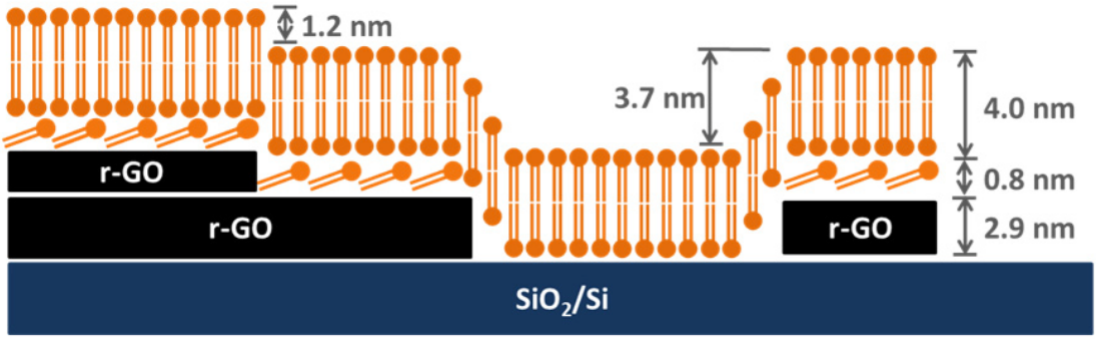

Figure 2.3 Tzusuki et al. proposed arrangement of lipid layers on reduced graphene oxide supported on SiO_2/Si. Substrates were incubated with vesicle suspensions, spontaneously forming lipid layers. From *(87)*.

The limitations of this approach, particularly important in the development of biosensors, are that surface coverage of the substrate is generally incomplete and that the lipid packing density cannot be controlled. This technique has also been used to deposit lipid layers onto graphene for sensing applications (88), which will be discussed in Section 2.1.6.

Langmuir-Blodgett deposition overcomes the limitations of the vesicle fusion method. The apparatus [Figure 2.4] allows the substrate to be drawn through a Langmuir monolayer transferring part of the monolayer to the substrate. By setting the initial surface pressure and using a feedback system to keep it constant (by altering the barrier separation during the substrate movement), the lateral packing of the monolayer can be controlled. The orientation of the initial lipid monolayer is controlled by the hydrophobicity of the substrate. Hydrophilic substrates must be immersed in the subphase, before the lipid monolayer has been added, enabling a lipid monolayer to be deposited as the substrate is raised through the surface. Hydrophobic substrates are held above the subphase, then lowered through the monolayer, to allow lipid deposition. By repeated dipping, multilayers can be formed [Figure 2.5].

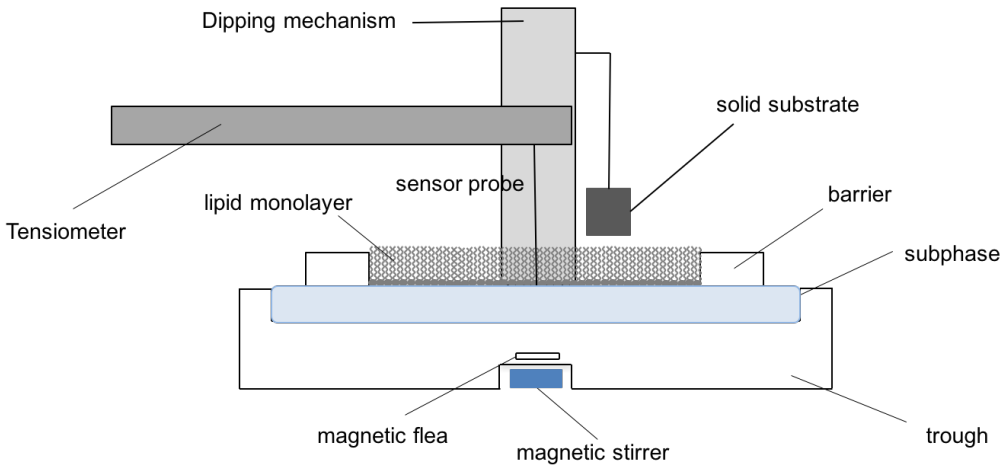

Figure 2.4 The Langmuir trough set up for Langmuir-Blodgett deposition. A controlled dipping mechanism is used to control the movement of the substrate through the lipid monolayer on the trough surface.

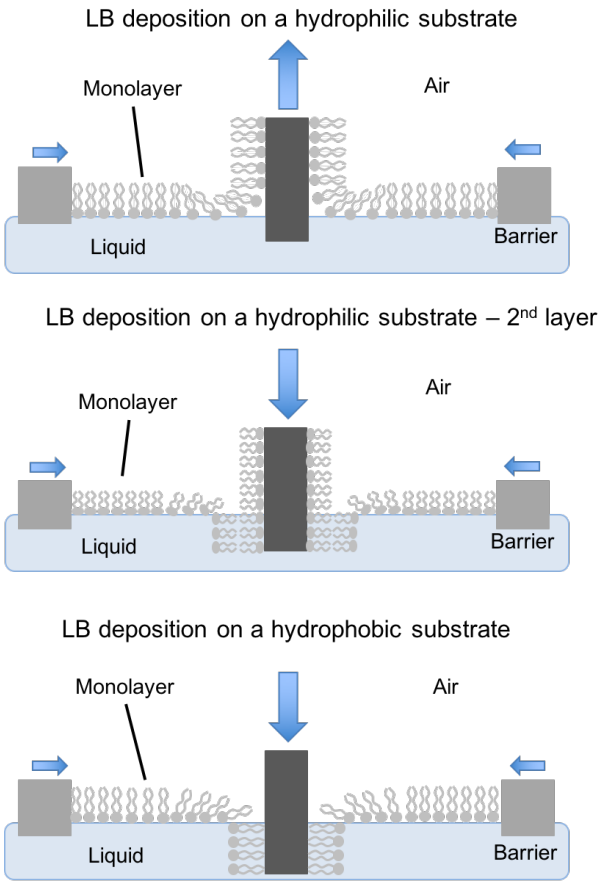

Figure 2.5 Diagram showing different lipid deposition on different surfaces. First, a hydrophilic surface raising through the lipid monolayer. Second, the same hydrophilic surface lowered through the monolayer, depositing a second layer on the surface. Third, a hydrophobic surface lowered through the lipid layer to deposit a monolayer.

2.1.6 Electrochemical Biosensors

Electrochemistry is a sensitive and inexpensive technique used to selectively detect electroactive analytes. Graphene is an attractive substrate for these sensors offering the prospect of combining electrochemical detection with another modality such as optical sensing. Graphene can also be produced with a low environmental impact and at a low cost. Because many biomolecules target the cell membrane, the concept for this sensor is to form a membrane mono- or bilayer mimicking a cell membrane on the graphene surface to detect the interaction of the target molecule through measuring changes in electron transfer, for example. Electron transfer between a solution species and an electrode can be affected by several factors: the properties of the solution species, its rate of diffusion through the electrolyte solution, and the presence of adsorbed species. In this case a phospholipid mono/bilayer can restrict electron contact with the surface of electrode, blocking electron transfer. It is this blocking effect that offers potential detection methods.

Ideal electrochemical detection requires a three-electrode system: a reference, a counter and a working electrode. The redox reaction being studied occurs at the working electrode. The reference electrode, usually Ag/AgCl, maintains a constant potential at the working electrode and the current flowing between the working electrode and a counter electrode is measured using a potentiostat [Figure 2.6].

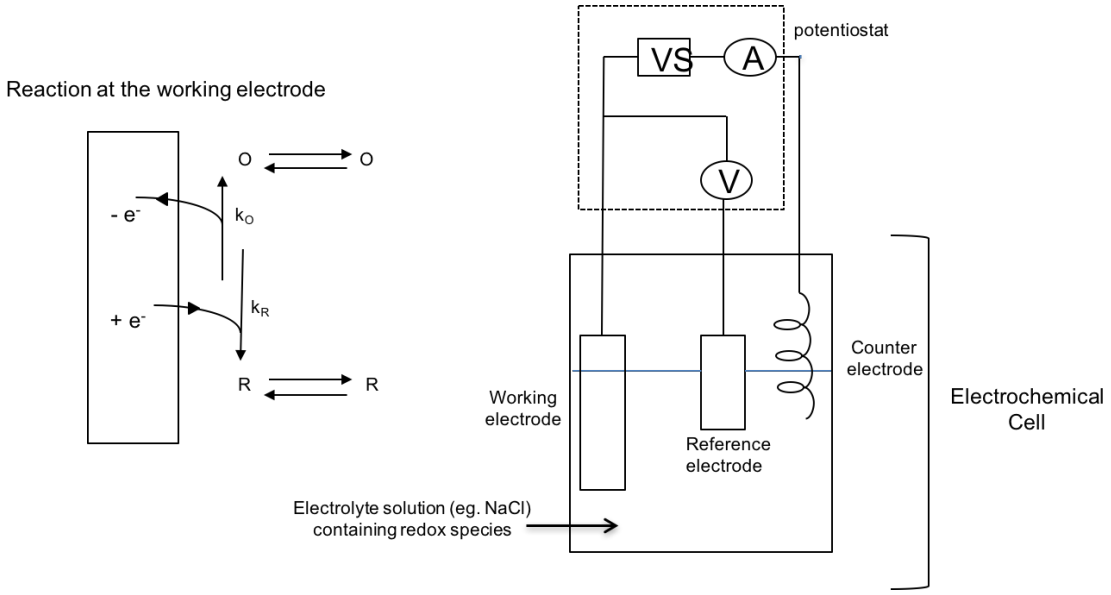

Figure 2.6 Three-electrode electrochemical cell (right) and a simple redox reaction occurring at the working electrode (left). O is the oxidised species, R is the reduced species, e^- is a single electron, k_o is the oxidation reaction rate constant and k_R the reduction reaction rate constant.

Shown in Figure 2.6 is a simple scheme of the redox reaction that occurs at the working electrode:

$$O + ne \underset{k_O}{\overset{k_R}{\rightleftarrows}} R$$

where *O* and *R* are the oxidised and reduced forms of the redox couple at the interface of the working electrode and *n* is the number of electrons exchanged between *O* and *R*. k_R *and* k_O are the reaction rate constants for the reduction and oxidation reactions.

Potentiometric devices measure the potential at the sensor interface, determined by the Nernst equation which governs the relationship between analyte concentration and potential in these reactions:

$$E_{cell} = E^0_{cell} - \frac{RT}{nF} ln \frac{[R]_\infty}{[O]_\infty} \quad (2.3)$$

where E_{cell} is the zero-current cell potential, E^0_{cell} is the formal potential contribution to the cell, *R* is the universal gas constant, *T* is the temperature in degrees Kelvin, *n* is the charge number of the electrode reaction, *F* is the Faraday constant, and [R]/[O] is the ratio of ion concentration at the anode to ion concentration at the cathode.

The electrochemical method used in this thesis is cyclic voltammetry. Cyclic voltammetry obtains information by applying a potential at the working electrode and then measuring the resulting current. The resulting current is then plotted against the applied potential [Figure 2.7].

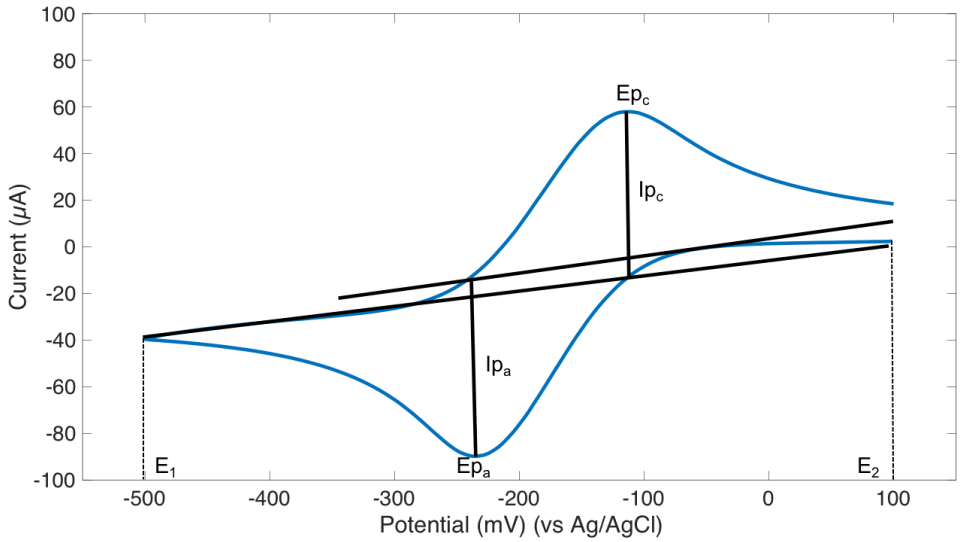

Figure 2.7 Cyclic voltammogram at a HOPG electrode in 0.1 M ruthenium hexamine at a scan rate of 50 mV/s, with an Ag/AgCl reference electrode and a Pt counter electrode. Ip_c and Ip_a are the cathodic and anodic current peaks. Ep_c and Ep_a are the cathodic and anodic peak positions and E_1 and E_2 are the potential limits of the voltammogram.

Cyclic voltammetry gives information about the redox potential and electrochemical reaction rates of analyte solutions. By considering the current peak ratio, $\frac{Ipc}{Ipa}$, and the current peak potential separation, $\Delta E_p = E_{pc} - E_{pa}$, the reversibility of the redox reaction can be assessed. For rapid, reversible systems, the current peat ratio is equal to one, and the peak potential separation $\sim \frac{59.2}{n}$ mV at 25°C, where n is the number of electrons transferred.

There have been a number of measurements on phospholipid bilayers supported on substrates such as glassy carbon, silicon dioxide (SiO_2) and gold (89), often with the aim of producing rapid point-of-care detectors (90). A small

number of sensors utilise graphene as a platform due to the ease of lipid mono- and bilayer formation on graphene, through non-covalent hydrophobic interactions between the lipids and the graphene whilst maintaining the desired properties of graphene. Liu *et al.* have developed a fluorescence biosensor to detect phospholipase D activity, an enzyme that catalyses the hydrolysis of the phospholipid, phosphatidylcholine into choline and phosphatic acid, important for understanding and regulating many biological processes (91). Other research has been conducted investigating bactericidal activity of antimicrobial peptides on neutral POPC, negatively charged POPC:POPG (2:1) and positively charged DOPC:DOTAP (2:1) bilayers (88). In the majority of these studies, bilayers were formed by vesicle fusion, leading to concerns about the integrity and uniformity of the layers. In this research we used the Langmuir-Blodgett technique to address these problems.

2.2 Experimental Methods

2.2.1 Glassware Preparation

All beakers used were first cleaned using Decon 90, then rinsed and sonicated with deionised water for 20 mins (Ultrawave Sonicator). This was then followed by rinsing and sonication in ethanol for a further 20 mins. Once sonication ended, the ethanol was disposed of, and the beakers were dried in a hot oven. The Hamilton syringe and glass vials, which were used to store lipids, were cleaned, firstly with deionised water followed by methanol then chloroform. With each cycle of cleaning, 5 – 10 rinses of the syringe were carried out.

2.2.2 Preparation and Characterisation of Graphene Oxide Suspension

Graphene oxide dry platelets (Graphene Supermarket, flake size 0.5 – 5 μm, thickness 1.1 ± 0.2 nm, 79% carbon 20% oxygen) were dispersed in nanopure water (18.2 MΩ) giving a 6 mg/ml concentration of graphene oxide (in order to achieve a concentration of 0.1 mg/ml once added to the subphase of the trough). The graphene oxide was sonicated for 1h, then centrifuged at 10,000 rpm for 10 minutes, to remove any aggregated graphene. The graphene oxide flakes were characteristed using scanning electron microscopy (FEI NanoBeam, SEM) on a metal substrate, Raman spectroscopy (Witec Alpha300 R Raman Imaging System) and atomic force microscopy (NT-MDT, Ntegra Aura).

To record Fourier Transform – Infrared (FT-IR) spectra of GO, the GO sample was prepared using the KBr disc technique. GO flakes were mixed with dry KBr powder (approximately 0.2 – 1 % of total mass GO) using a pestle and mortar and poured into the sample holder. The KBr disk was pressed using a hydraulic press. The KBr disk was then inserted into the IR sample holder and the spectra were ran using an IRTracer-100 in transmittance mode. The spectra were recorded using LabsolutionsIR software.

2.2.3 Microelectrophoresis of Graphene Oxide

To determine the charge of the GO flakes, a flow chamber was adapted for microelectrophoresis measurements [Figure 2.8]. The flow chamber was set up on a microscope stage. 150 µl of 1 mg/ml GO solution in water was added to the flow chamber and allowed 10 mins to settle.

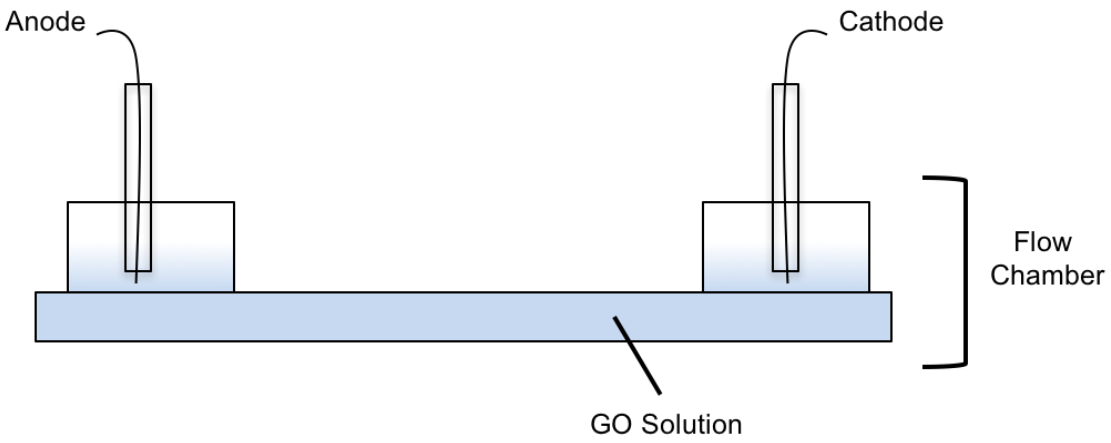

Figure 2.8 The flow chamber with the GO solution flowing between the two electrodes. By applying a voltage across the two electrodes, the charge of the GO flakes can be determined by tracking the direction of movement of the flakes.

The two electrodes were placed in opposite sides of the chamber, ensuring full contact with the GO solution. A voltage of 2V was applied across the two electrodes. Videos were then recorded using bright-filed microscopy (Leica DMFLS, 63X objective) to track the direction of movement of the graphene oxide flakes.

2.2.4 Lipid Preparation for Langmuir Monolayer

All lipid solutions were stored in glass vials sealed with Parafilm at a temperature of approximately -20°C. Various compositions of lipid mixture were used in this series of experiments. Lipid mixtures that best represent the lipid compositions of the inner and outer leaflets of biological membranes were used for the first set of experiments. These mixtures were delivered in chloroform to assure a

homogenous mixture, at a concentration of 1 mg/ml (Avanti Polar Lipids). The lipid solutions were used as supplied. The lipid compositions used are given in Table 2.1.

Lipid	Inner Leaflet % (w/w)	Outer Leaflet % (w/w)
16:0 PS	22.3	0
16:0 PC	11.8	15.1
16:0 PE	38	48.7
Cholesterol	20	25.6
16:0 SM	8.3	10.3

Table 2.1 The different lipid compositions of the inner and outer leaflet mixtures; 16:0 PS (1,2-dipalmitoyl-*sn*-glycero-3-phosphoserine); 16:0 PC (1,2-dipalmitoyl-*sn*-glycero-3-phosphocholine); 16:0 PE (1,2-dipalmitoyl-*sn*-glycero-3-phosphoethanolamine); cholesterol; 16:0 SM (N-palmitoyl-D-*erythro*-sphingosylphosphorylcholine).

2.2.5 Langmuir Trough Preparation

All measurements were carried out using a Kibron μ-trough (45 mm X 131 mm) with two moveable barriers, and Filmware version 2.41 software. The Langmuir trough and barriers were first cleaned and polished to remove any scratches from the surface. This was done using lapping glass and mild detergent. The scratches were removed from all surfaces, by gently moving the trough and barriers over the lapping glass, with frequent washing with pure water. The Langmuir trough was then rinsed in ethanol, and contaminants were removed using a HFC (hydofluorocarbon) free air duster. The trough was then placed in the holder, underneath the sensor arm. A magnet, attached to a stirrer plate, was placed underneath the trough, and a magnetic flea in the middle of the trough. This was set at a speed of 180 rpm. The same cleaning and lapping process as used for the trough was applied to the barriers. The trough was filled with approximately 60 ml of nanopure water. The sensor probe, stored in ethanol, was run through a flame to remove any contaminates. This was repeated a few times. The probe

was then attached to the sensor arm, and lowered into the water subphase and calibrated according to the manufacturer's instructions. The barriers were initialised to determine the trough edge, and hence the greatest surface area of the trough. The trough surface was cleaned by repeated sweeps of the barriers across the surface, followed by aspiration of the surface using a hypodermic needle attached to a vacuum pump whilst the barriers were at minimum separation. This process was repeated until there was no further change in surface pressure with barrier compression. The probe was then re-zeroed. Once the surface was clean, the lipid solution was then spread on the surface. The lipid solution was deposited onto the surface using a Hamilton syringe. Volumes between 10 – 25 µl of chloroform containing 1 mg/ml of lipid were added depending on the lipid being used. To deposit the lipids, firstly, a small droplet was formed on the end of the syringe, no bigger than 1 µl. Then, gently, the end of the syringe was pressed onto the surface, ensuring lipids were not added too close to the barriers, trough edges and the probe. This prevented build-up of lipids on these surfaces. It is important to deposit small volumes of lipid at a time because if the droplet is too big, it could sink through the surface, depositing the lipids on the bottom of the trough. After the required volume of lipid had been added to the surface, the monolayer was then left to equilibrate for 15 min. This allowed sufficient time for all the solvent to evaporate.

2.2.6 Recording π – A Isotherms

π-A isotherms were constructed by compression and relaxation of the barriers at a rate of 0.5 $Å^2$/molecule/min. The optimum rate was determined after testing a range of rates. At a faster rate, smaller details of the isotherms were not being picked up, noticeably, missing the phase transitions. Cycles of compressions and relaxation were repeated until a reproducible trace of the isotherm was achieved. This is indicative of a stable monolayer, meaning the graphene oxide may now be incorporated into the lipid monolayer.

2.2.7 Incorporating Graphene Oxide into the Lipid Monolayer

To incorporate the GO into the monolayer, the GO solution was injected underneath the barriers into the subphase of the trough using a 1 ml syringe with needle attachment, after the monolayer had equilibrated at a chosen constant pressure. Initially experiments were carried out using 1 mg/ml GO solution in order to achieve a 0.05 mg/ml concentration inside the trough, however, this required using approximately 3 ml of solution which caused leaking at the edges of the trough. Therefore, it was decided that an optimum volume would have to be between 0.5 – 1 ml, arriving at the decision to use 1ml of a 6 mg/ml GO solution, to give a 0.1 mg/ml concentration in the trough. After addition of GO the system was held at a constant pressure and subsequent changes in trough area were recorded. After area had stabilised pressure-area isotherms were recorded, starting in the direction of increasing surface pressure. Generally, 3-4 compression-relaxation cycles were performed.

2.2.8 Lipid Preparation for Langmuir – Blodgett Deposition

Only lipid mixtures that do not form domains were employed in these experiments to ensure uniformity of the films. Details of these are given in Table 2.2.

Substrate	Lipid used (Avanti Polar Lipids)
Silicon	DPPC
HOPG	DPPC:Chol (80:20) DPPC
BDD	DPPC DOPC DOPC:DPPC (1:1)

Table 2.2 The different substrates used for Langmuir-Blodgett deposition, and the different lipids deposited.

Cholesterol solutions were prepared by dissolving cholesterol powder in chloroform, to a concentration of 1 mg/ml.

2.2.9 Substrate Cleaning

Lipid mono- and bilayers were deposited onto a range of different carbon materials, including boron-doped diamond (BDD, Diamond Detectors Ltd., Poole UK, boron acceptor concentration ≥ 10^{20} cm^{-3}) (9.6 cm^2) and highly-oriented pyrolytic graphite (HOPG) (10X10X1, 2 mm^3, NT-MDT Co., Moscow). Silicon (p^+-doped Si with 300 nm SiO_2 coating, IDB Technologies) was also used as a substrate in preliminary experiments. Silicon substrates were cleaned using successive sonication steps. Firstly, the substrates were sonicated for 30 min in acetone, then for 20 min in nanopure water, and finally 15 min in isopropanol. The substrates were then dried using a steady flow of nitrogen. HOPG substrates were cleaned using the "cleaving" method. This was performed by using tape to stick to the dirty surface of the HOPG and peel off the top layer of carbon, leaving a clean surface underneath. BDD substrates were cleaned, first by rinsing with water, then methanol and finally polished using alumina slurry (0.3 μM, 0.05 μM, Sigma Aldrich, UK).

2.2.10 Lipid Deposition

The Langmuir trough was set up as previously described [Section 2.2.4]. Silicon, a hydrophilic substrate, attached to a dipping arm, was lowered into a nanopure water subphase. The lipid solution was then added to the surface. Once a stable lipid monolayer was established, a π-A isotherm was constructed and the film was set at the required surface pressure. The feedback system was then set to maintain this pressure during dipping. The pressure was generally maintained at 30 mN/m to approximate the packing density found in biological membranes. The substrate, attached to the dipping arm, was then raised through the lipid monolayer at a rate of 1 mm/min to deposit a monolayer. The substrate was then left to air-dry 15 minutes before depositing a second layer by lowering the

substrate back through the monolayer at the same rate. Once fully immersed in the subphase, the surface was cleaned by repeated aspiration until surface pressure returned to zero in order to remove the lipid monolayer from the surface before raising the substrate out of the substrate, to prevent further lipid deposition.

Because the BDD substrate was too large (3.5 cm diameter, 9.6 cm^2 area) to be dipped into the trough, the Langmuir-Schaefer method was used to deposit monolayers. In this approach, lipid layers were deposited onto the substrate through dipping horizontally, rather than vertically (92).

As HOPG is naturally hydrophobic, a lipid monolayer with the fatty acid tails adhering to the substrate was deposited by setting up the trough with the HOPG poised above the lipid monolayer, and then lowered through the film at a rate of 1 mm/min. The surface was then cleaned to reach a surface pressure of zero, and then the HOPG was removed from the subphase. No attempt was made to assemble an inverted bilayer. However, normal bilayers were assembled as for silicon on HOPG rendered hydrophilic by anodic polarization. For this, the HOPG was held in the electrochemical cell, filled with 0.1 M NaOH solution at 1500 mV for 3 min.

2.2.11 Surface Characterisation

For all the bilayers and monolayers, the deposition ratio, τ, was calculated by measuring the change in trough area before deposition and after deposition (93)

$$\tau = A_l / A_s \tag{2.4}$$

where A_l is the decrease in the area of the trough and A_s is the coated area of the solid substrate. The deposition ratio was used to characterise the transfer of layer. When the deposition ratio is equal to one, the transfer has been complete. Wetting properties were analysed using a stereo microscope (used horizontally) attached to a CCD camera (AVT Marlin) and a syringe which was used to release a water droplet on the substrate surface. The contact angle was measured as the angle formed between the substrate and the edge of the water droplet.

Atomic force microscopy (AFM) was also used for characterisation of the mono- and bilayers on silicon substrates. DPPC Lipid mono- and bilayers were deposited onto half of the silicon substrates in order to form a step height between the surface and the lipids. An AFM (NT-MDT, Ntegra Aura) was used at room temperature in semi-contact mode to detect surface topographical changes. AFM was also used to determine surface roughness of HOPG and BDD substrates.

2.2.12 Measurement of Electrochemical Properties of Lipid Films

To determine the electrochemical properties for all substrates (BDD and HOPG), the same method was used. A three-electrode system was used for all measurements. The substrate with lipid layer adsorbed was placed on an electrical contact, and inserted in the bottom of the electrochemical cell [Figure 2.9]. The cell was filled with a solution containing the electroactive solute, ensuring no bubbles form in the cell. Both ruthenium hexamine $[Ru(NH_3)_6]^{3+/2+}$ and ferricyanide ($[Fe(CN)_6]^{3-/4-}$) were used as electroactive probe molecules at a 1mmol concentration in 0.2M KCl, ruthenium being used for the bulk of the experiments as it was found to be more stable over time. This thesis has not explored the charge structure of membrane pores where choice of electrolyte is important, where both species would need to be compared.

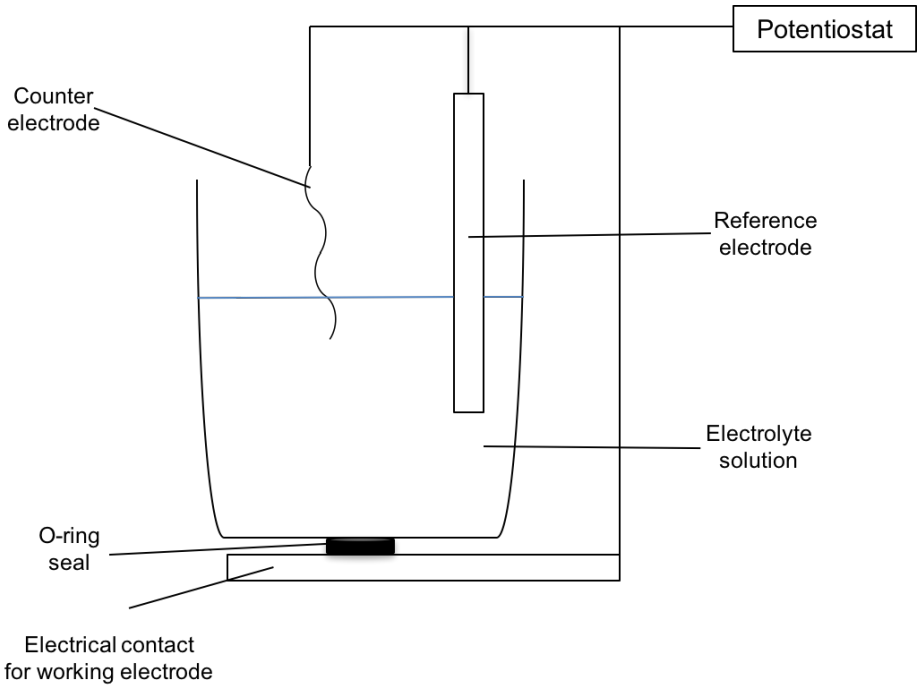

Figure 2.9 Experimental set up of the electrochemical cell, showing the 3-electrode system. The substrates used in these experiments are held in place between the O-ring and the electrical contact.

The electrodes used in this experiment were an Ag/AgCl reference electrode (BASi) with a salt bridge containing 3M NaCl (Sigma Aldrich, UK) and a platinum counter electrode (BASi) of curled wire for greater surface area. Nitrogen was bubbled through the electrolyte solution for 10 minutes to remove oxygen. Measurements were performed on a Bas100W electrochemical analyser. A scan rate of 50 mV/s was used, over a potential scan of -0.8 V – 0.6 V.

2.3 Results and Discussion

This section includes all Langmuir trough results for graphene oxide interacting with inner and outer leaflet lipid mixtures, the π-A isotherms and dilational modulus. It also includes results from the Langmuir-Blodgett deposition of lipid mono- and bilayers onto different substrates, and their electrochemical response.

2.3.1 Characterisation of Graphene Oxide

For all experiments the same method for producing graphene oxide suspensions was used [Section 2.2.2].

Raman spectroscopy was one of the methods used to characterise the GO. GO has two characteristic Raman peaks, the G-peak (1580 cm^{-1}) and the D-peak (1350 cm^{-1}), which relates to the honeycomb lattice of carbon atoms and defects in the crystal (predominantly, the oxygen groups), respectively. A typical Raman spectrum obtained for the GO samples is shown in Figure 2.10.

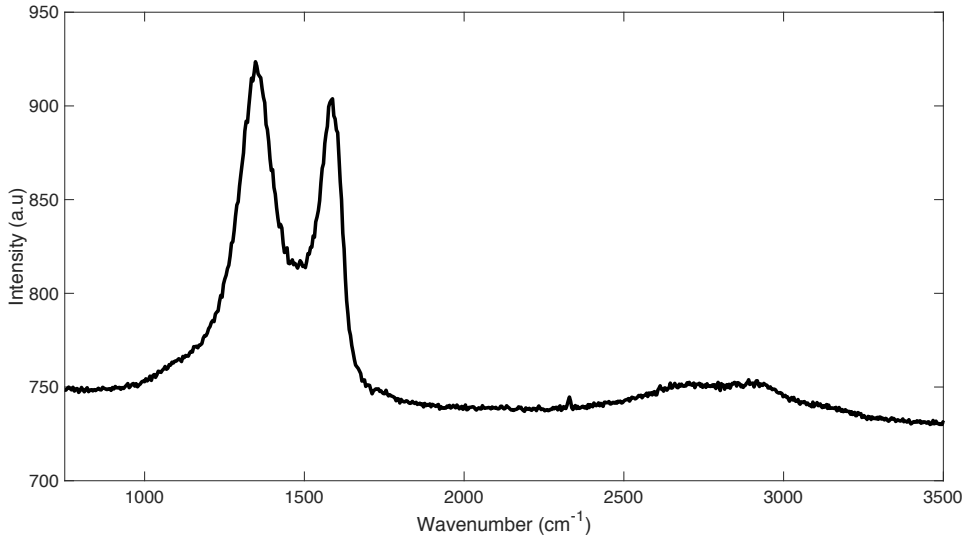

Figure 2.10 A typical Raman spectrum obtained for GO showing its two characteristic peaks at 1351 cm^{-1} (D-peak) and 1584 cm^{-1} (G-peak).

The Raman spectrum shows the D-peak at 1351 cm^{-1} and the G-peak at 1584 cm^{-1}.

Scanning electron microscopy (SEM) was used to determine the average size of the flakes produced. An example of the SEM images obtained is shown in Figure 1.3. The graphene oxide is distinguished by the dark grey flakes. Figure 2.11 shows the histogram of size distribution of GO flakes suspended in nanopure water.

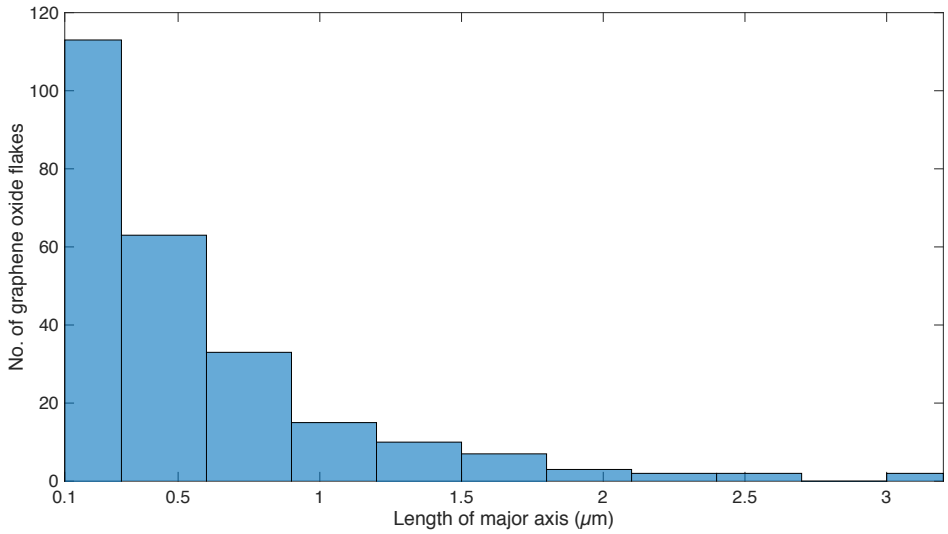

Figure 2.11 Histogram of the size distribution for 0.1 mg/ml GO suspension, centrifuged for 10,000 rpm for 10 min.

The analysis of 250 GO flakes gives an average size of ~ 0.5 μm (the size is measured according to the length of the major axis).

To determine the average thickness of the GO flakes produced, atomic force microscopy (AFM) was used. Height profiles were taken across various cross sections of GO flakes (n=100) [Figure 2.12].

a)

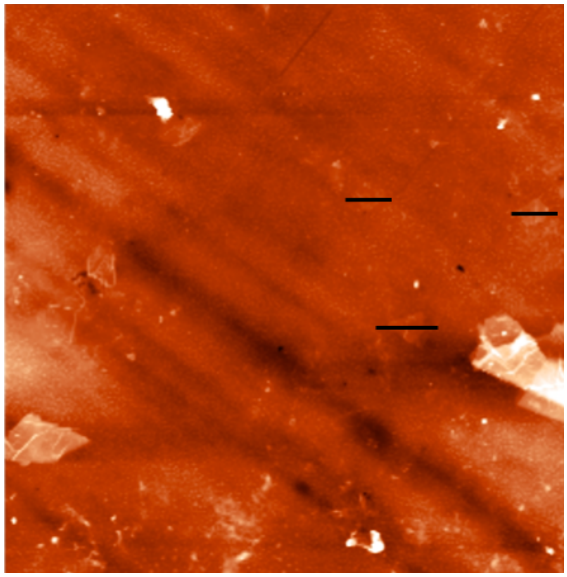

b)

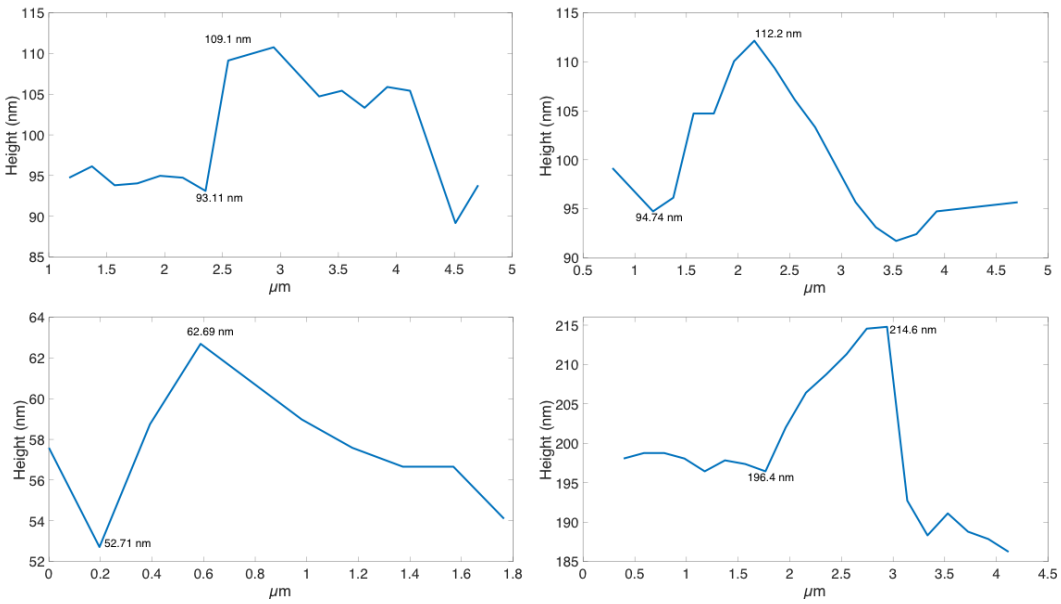

Figure 2.12 a) 50 x 50 μm AFM image scan of 0.1 mg/ml GO giving examples of the cross-sections taken for height analysis b) examples of height profiles taken across GO flakes.

Height profiles of 100 GO flakes were taken giving an average thickness of ~ 13 nm [Figure 2.13].

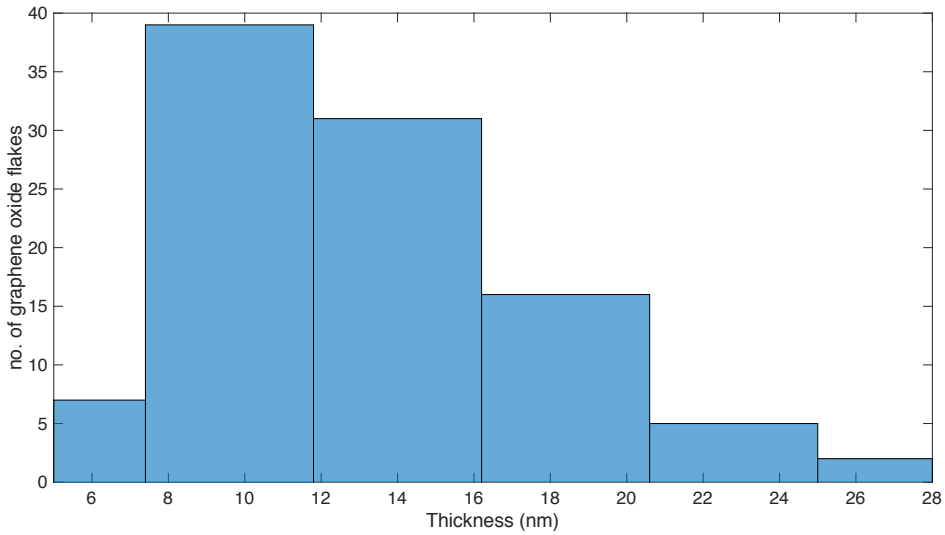

Figure 2.13 Histogram of the thickness distribution for 0.1 mg/ml GO suspension, centrifuged for 10,000 rpm for 10 min.

The expected thickness was 1.1 ± 0.2 nm (the recorded thickness provided with the data sheet: Graphene Supermarket), however the AFM used for this analysis was unable to resolve below 5 nm so it was not possible to analyse flakes of the expected thickness.

The chemical composition of the GO samples used can be determined using FT–IR spectroscopy, due to its characteristic IR Spectrum. Figure 2.14 shows the typical FTIR spectrum obtained. Characteristic features of the spectrum are shown at 3420 cm^{-1} (O–H), 1719 cm^{-1} (C=O from carbonyl and carboxyl groups), 1612 cm^{-1} (C=C from aromatic carbons), 1049 cm^{-1} and 1198 cm^{-1} (C–O from alkoxy and epoxy groups) as expected from previous literature (94) (95) (96). The FTIR spectrum provides information of the presence of different functional groups across the GO surface.

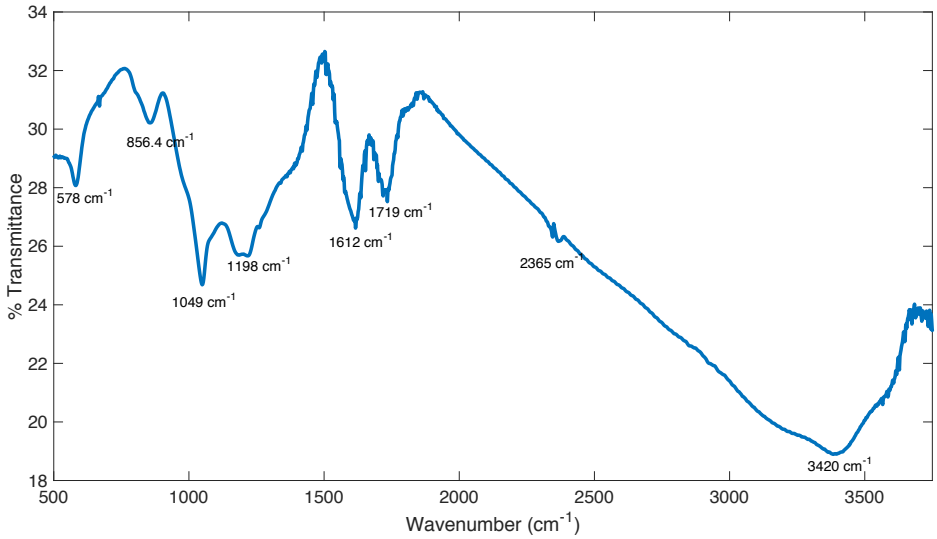

Figure 2.14 FTIR spectrum of graphene oxide, showing the presence of different oxygen-containing functional groups.

2.3.2 Surface Charge of Graphene Oxide

Microelectrophoresis was used to determine the charge of the graphene oxide by tracking the motion of the dispersed charged particles relative to a fluid under the influence of an electric field. Videos of the GO flakes were recorded showing an overall migration of flakes towards the cathode, determining GO to be negatively charged. The overall surface charge of the GO is calculated by determining the drag force of the GO flakes through solution relative to the applied voltage. The drag force is calculated using

$$F_D = p\tau A \tag{2.5}$$

where F_D is the drag force, p is the density of the fluid, τ is the shear stress ("drag") in the fluid and *A* is the average area of the GO flakes. To calculate τ, Equation 2.6 is used

$$\tau = \frac{C_D p v^2}{2} \tag{2.6}$$

where C_D is the drag coefficient and v is the calculated velocity of the GO flakes. C_D is defined as $0.074(Re)^{-1/5}$ where Re is the Reynolds number

$$Re = \frac{\rho v L}{\mu} \tag{2.7}$$

and L is the average length of GO flake and μ is the viscosity of water. Once the force has been calculated it can be used to determine the total charge, q

$$F = q\frac{V^2}{d} \tag{2.8}$$

where V is the applied voltage and d is the distance between the two electrodes. The average total charge calculated for GO (n=30) was 1.61 $\pm$ 0.88 x 10^{-16} C per flake.

2.3.3 Langmuir Monolayer π – A Isotherms

Figure 2.15 shows the π-A isotherms of the lipid mixtures representative of the inner and outer leaflet of the cell membrane [Table 2.1]. The isotherms are distinctively different. The inner leaflet has a steeper gradient and appears as a smoother curve. For both isotherms a clear first order transition occurs, shown by a plateau in the isotherms, indicating a phase transition. However, this transition is extended for the outer leaflet, and occurs at a higher area per molecule. The phase transition for the inner leaflet also occurs at a lower pressure. The inner leaflet has a higher compressibility as shown by the dilational modulus. It is possible that the addition of PS in the mixture could increase the stability of domain structures, partially due to the unusual bonding that occurs between PS molecules which overcomes repulsive electrostatic forces between the negatively charge head groups (97).

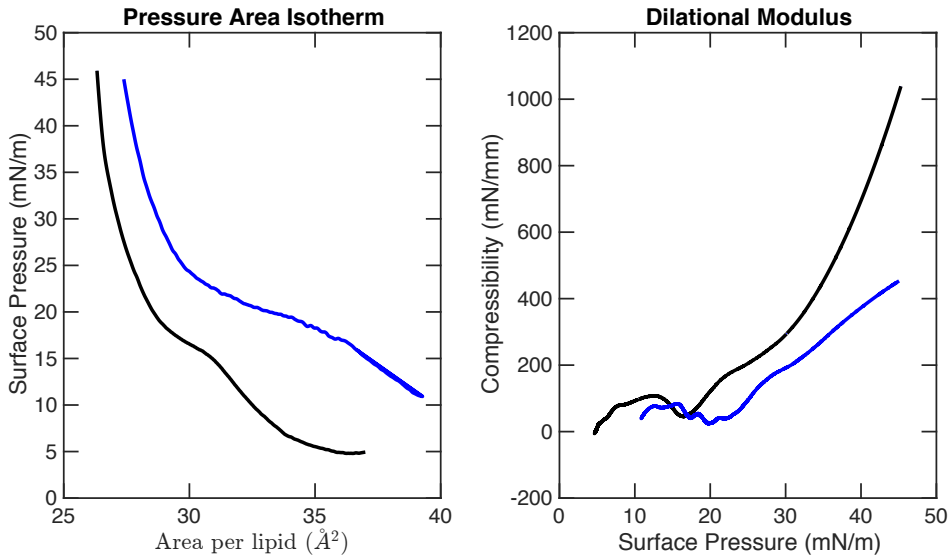

Figure 2.15 Pressure (mN/m) vs Area per lipid (Å^2) isotherms (left) comparing inner (black) and outer (blue) lipid mixtures, with the corresponding dilational modulus (right).

The isotherms reported here are in good agreement with previously recorded isotherms for the inner and outer membrane leaflets (98).

In order to characterise the effects of the graphene oxide – lipid interaction, π-A isotherms were investigated for the different lipid systems after addition of graphene oxide to the subphase. In all experiments of this type, the monolayer was first compressed and relaxed a few times, to ensure a reproducible isotherm. The graphene oxide was then added to the subphase at pressures either at which the monolayer was undergoing its phase transition (~ 10 – 20 mN/m) or when the monolayer was in a compressed state (~ 20 – 30 mN/m). The system is then given a 15 minute equilibration period, whilst the subphase was continuously stirred, before relaxation and compression of the monolayer with the presence of graphene oxide.

Figures 2.16 and 2.17 show the change in trough area recorded for one experiment during addition of the graphene oxide, at constant pressure, to the inner and outer leaflet monolayers, respectively. All results recorded (n=5 for each experiment) show an increase in area, which is presumed to arise from graphene oxide insertion in the monolayer.

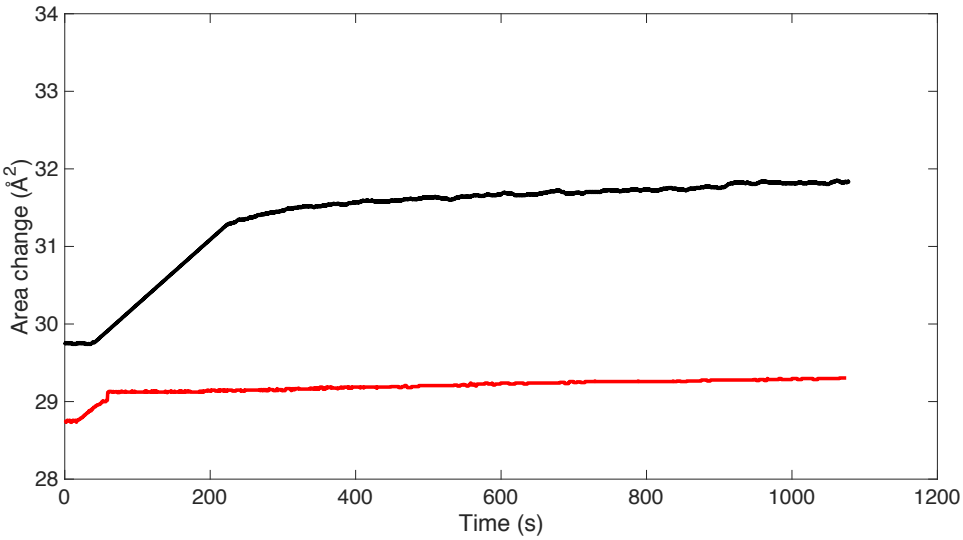

Figure 2.16 Time vs area per molecule comparing the change in area observed during addition of graphene oxide at 17 mN/m (black) and 20 mN/m (red) to the inner leaflet monolayer. Graphene oxide was added at t=0 after the monolayer had equilibrated for 15 min.

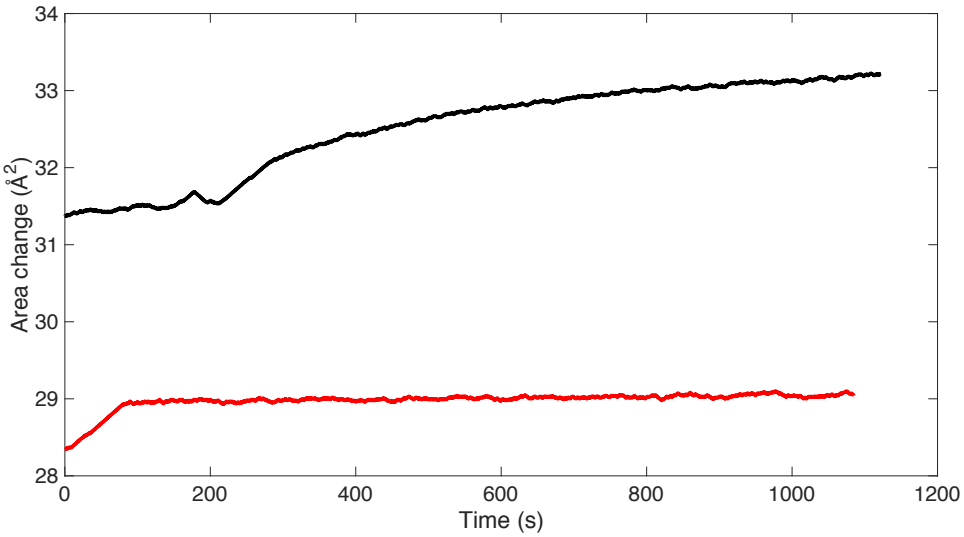

Figure 2.17 Time vs area per molecule comparing the change in area observed during addition of graphene oxide at 18.5 mN/m (black) and 25 mN/m (red) to the outer leaflet monolayer. Graphene oxide was added at t=0 after the monolayer had equilibrated for 15 min.

For both monolayers there is a greater increase in area when graphene oxide is added at the phase transition. At the phase transition, the lipids are less densely packed, meaning the monolayer is more permeable to graphene oxide. Penetration allows possible interactions between the head groups of the phospholipids and also the fatty acid tails. A change in area of 2.1 $Å^2$ was recorded at the inner leaflet monolayer and 1.85 $Å^2$ at the outer monolayer. A slightly greater change in area was observed at the inner leaflet monolayer. This may arise from repulsive forces between the oxygen-containing groups on the graphene oxide, and the negatively charged PS head groups.

The proposed mechanisms of GO insertion are given in Figure 2.18 showing the increase in trough area on addition of GO to the inner and outer monolayers at the phase transition. It is important to note at this stage, an investigation into the orientation of GO has not been conducted. The proposed mechanisms show examples of both ‘edge-on’ and ‘face-on’ GO.

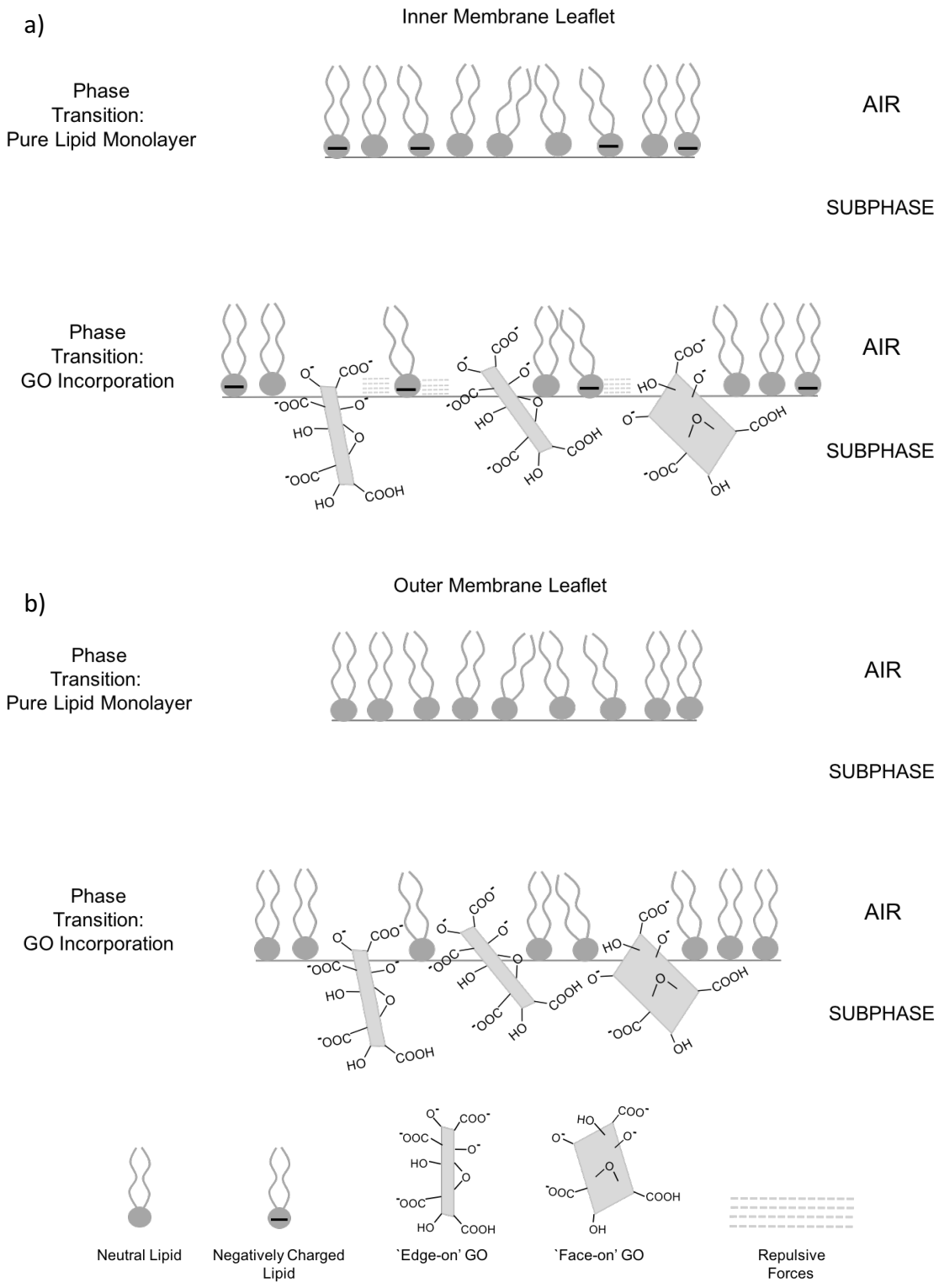

Figure 2.18 The addition of GO at the monolayer phase transition for a) inner membrane leaflet and b) outer membrane leaflet and the resulting change in trough area. A greater increase in area is observed for the inner leaflet, possibly due to repulsive forces between the negatively charged lipids and GO.

At the condensed phase a change in area of 0.57 $Å^2$ at the inner monolayer, and 0.7 $Å^2$ at the outer monolayer, was observed. When the monolayer is in a condensed phase the graphene oxide can only interact with the lipid head groups. The change in area observed at the inner monolayer is less than at the outer. This suggests less graphene oxide is inserted into the monolayer, possibly due to a more concentrated overall negative charge from the PS head groups repelling the graphene. Figures 2.19 and 2.20 show the proposed interactions of GO with the inner and outer membrane leaflet, respectively.

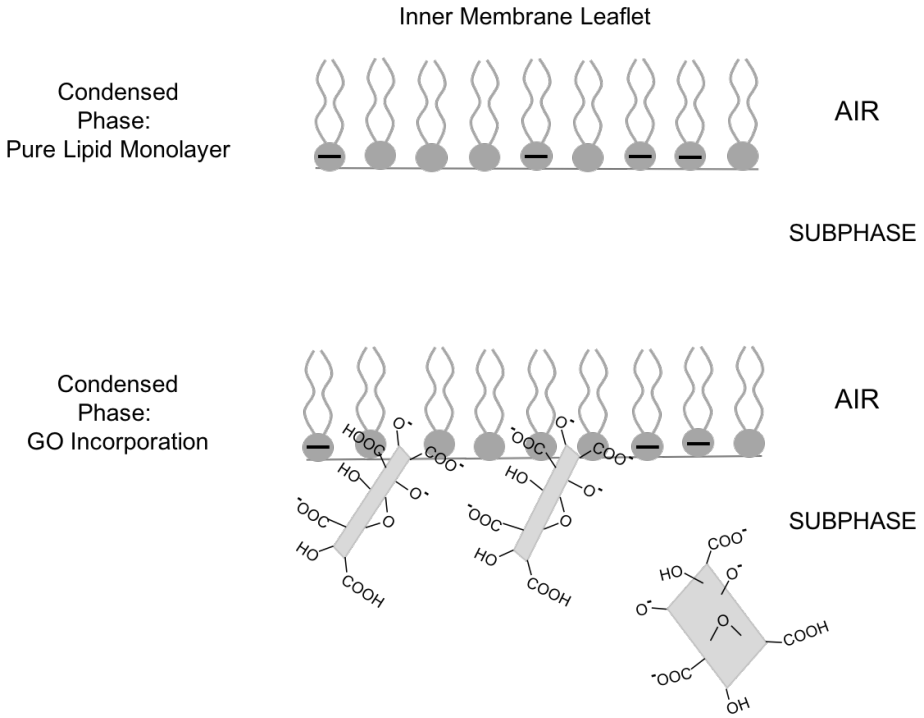

Figure 2.19 The addition of GO to the inner leaflet monolayer at the condensed phase. The GO interacts with the neutral lipid head groups, with negatively charged lipid head groups repelling some GO forcing it away from the surface. Only a small increase in area is observed, as the monolayer is more tightly packed and harder for the GO to penetrate.

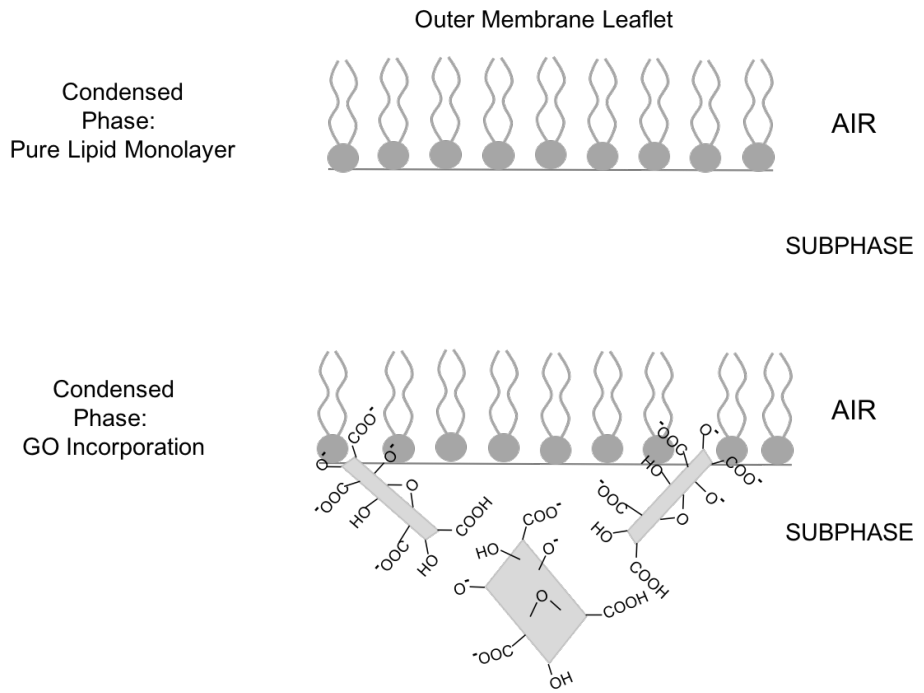

Figure 2.20 The addition of GO to the outer leaflet monolayer at the condensed phase. There is a greater increase in area compared to the inner leaflet monolayer due to the absence of the negatively charged lipid head groups, however, the increase in area is still small due to the condensed packing of the lipids.

After addition of graphene oxide, and re-equilibration of pressure, the monolayer was then relaxed and subsequent cycles of compression and relaxation are performed in order to record reproducible isotherms. The results presented here are examples to show the general trends of the π-A isotherms recorded throughout multiple experiments (n=5 for each experiment). Figure 2.21 shows the π-A isotherms and the dilational modulus for the inner leaflet, with graphene oxide added at 17 mN/m, the phase transition pressure. The presence of graphene oxide increases the overall pressure of the system. The plateau region observed in the isotherm recorded with graphene shifts to a higher area per molecule and shows an extended phase transition, indicating either additional graphene oxide insertion into the monolayer or stronger lipid-graphene interactions. The difference in gradient between the isotherms suggests graphene oxide inserts in between the lipid molecules interacting with the head groups on the surface, decreasing the compressibility of the monolayer. The dilational modulus confirms a significant decrease in the compressibility of the monolayer in the presence of graphene oxide. A further decrease in the dilational modulus at ~ 45 mN/m shows the monolayer is beginning to collapse. It appears the addition of graphene oxide produces a 'harder' monolayer under compression, resulting in the reduced values for the dilational modulus, possibly due to graphene oxide interfering with the packing of the lipid tails or the graphene itself is being extruded from the monolayer. The proposed interactions are given in Figure 2.22.

Figure 2.23 shows the π-A isotherms and dilational modulus for the inner leaflet with graphene oxide added at 20 mN/m, the condensed phase pressure. The isotherms are less smooth, indicating more complex phase behaviour, with inflections around 30 – 35 mN/m. Analysis of the isotherms recorded and the corresponding dilational modulus curves shows the addition of graphene oxide increases the overall pressure and decreases the compressibility, but to a lesser extent than when graphene oxide is added at the phase transition where there is more graphene oxide inserted in the monolayer. No changes in the isotherms are observed with repeated compression and relaxation of the monolayer, with no further graphene oxide inserting in the monolayer. This would suggest an initial interaction of graphene oxide with the lipid head groups, which reaches saturation [Figure 2.24].

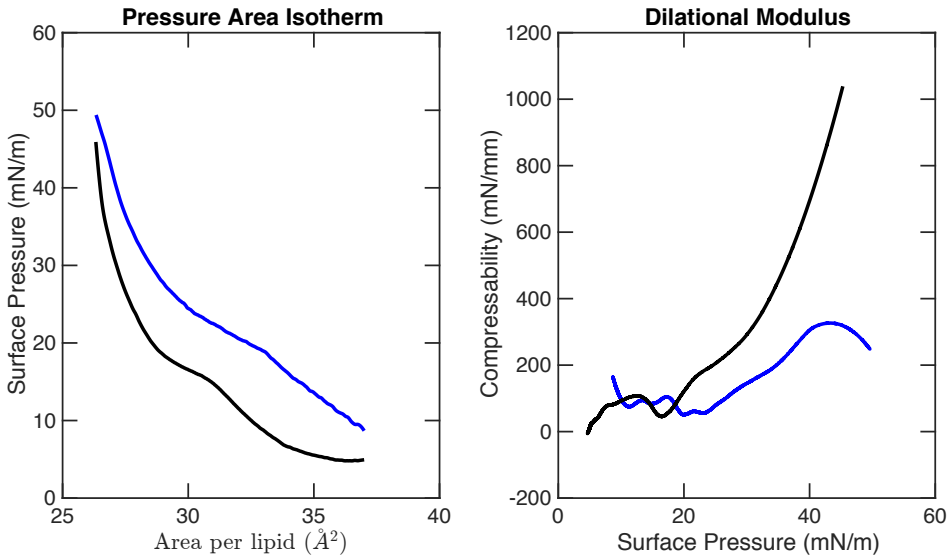

Figure 2.21 Pressure-Area isotherms (left) and Dilational modulus vs surface pressure (right) comparing a pure inner leaflet mixture (black) with inner leaflet with graphene oxide incorporated at a constant pressure of 17 mN/m (blue).

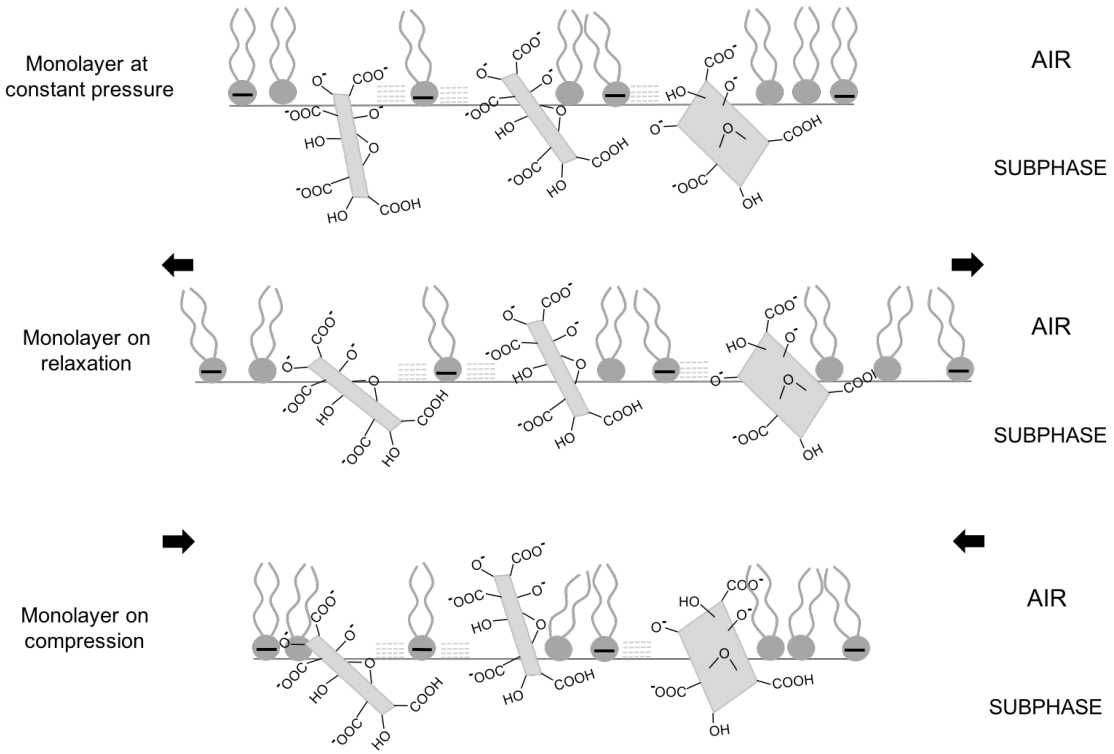

Figure 2.22 Proposed GO interactions with the inner monolayer at the phase transition. Once the GO is added at the phase transition, the barriers are relaxed and compressed. Due to the repulsive forces between the GO and negatively charged lipids, there is greater difficulty compressing the monolayer, and the lipids are less densely packed.

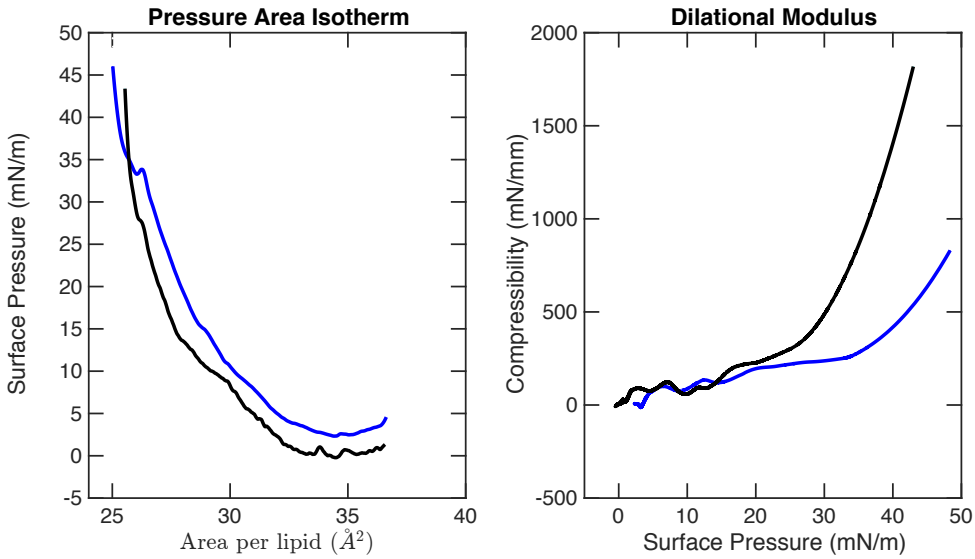

Figure 2.23 Pressure-Area isotherms (left) and Dilational modulus vs surface pressure (right) comparing a pure inner leaflet mixture (black) with inner leaflet with graphene oxide incorporated at a constant pressure of 20 mN/m (blue).

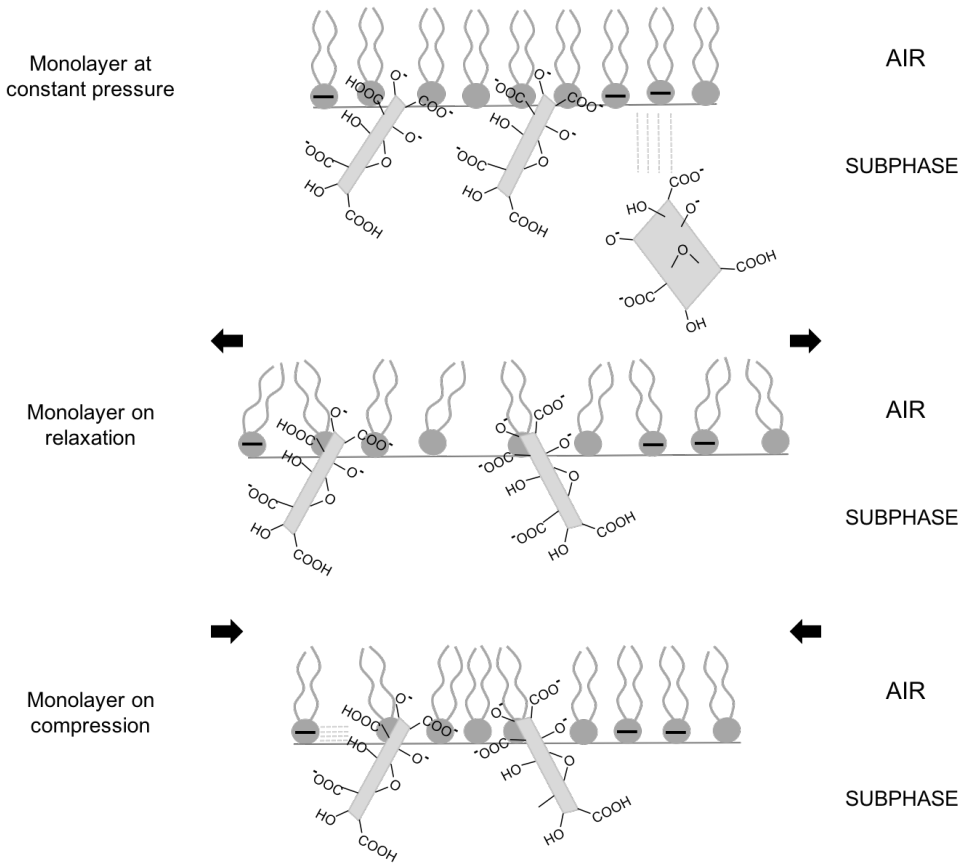

Figure 2.24 Proposed GO interactions with the inner monolayer at the condensed phase. Less GO is incorporated into the monolayer at the condensed phase. There is an initial interaction with GO and neutral lipids, with negatively charged lipids repulsing the remaining GO. As the barriers relax remaining GO sinks to the bottom of trough.

Figures 2.25 and 2.27 show the π-A isotherms and dilational modulus recorded for the outer leaflet monolayer with graphene oxide addition at 20.5 mN/m and 30 mN/m, respectively. In contrast to the results reported for the inner membrane leaflet, results were similar for different initial monolayer pressures. For both the phase transition and condensed pressure the initial relaxed pressure increases by ~ 5.5 ± 0.5 mN/m. This suggests that, although the initial change in area during graphene oxide addition was lower at the condensed pressure than at the phase transition, the same amount of graphene oxide has been inserted into the monolayer. It is possible that the graphene oxide is interacting weakly with the head groups of at least some components of the mixture, which in turn allowed for more graphene oxide insertion on the first relaxation of the monolayer. Since this was not shown for the inner leaflet, it is probable that PS is a significant determinant of graphene oxide insertion. The change in dilational modulus supports this hypothesis showing a compressibility of ~ 400 mN/mm before graphene oxide insertion, and ~ 350 mN/mm after for both experiments. Thus, the addition of graphene oxide decreases the compressibility, but not as dramatically as for the inner leaflet. The proposed mechanisms are given in Figure 2.26 and 2.28.

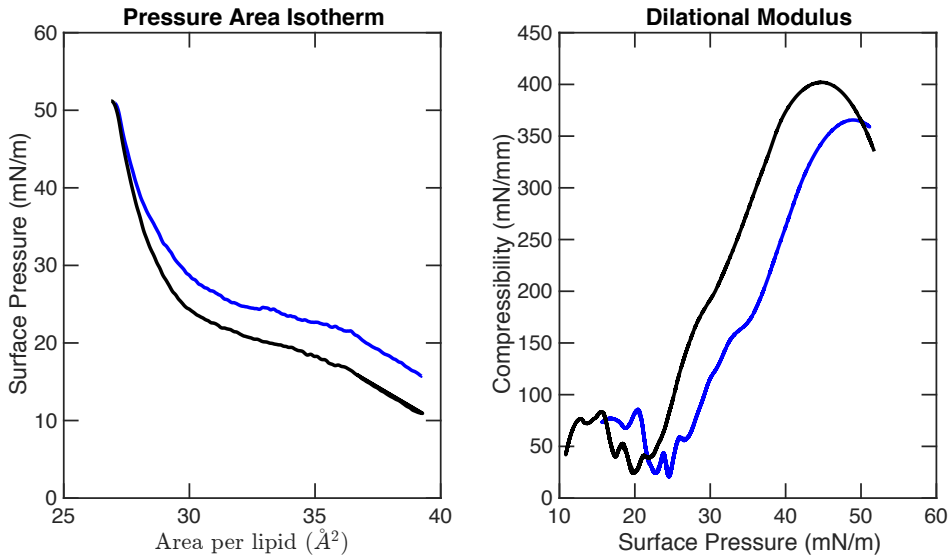

Figure 2.25 Pressure-Area isotherms (left) and Dilational modulus vs surface pressure (right) comparing a pure outer leaflet mixture (black) with outer leaflet with graphene oxide incorporated at a constant pressure of 20.5 mN/m (blue).

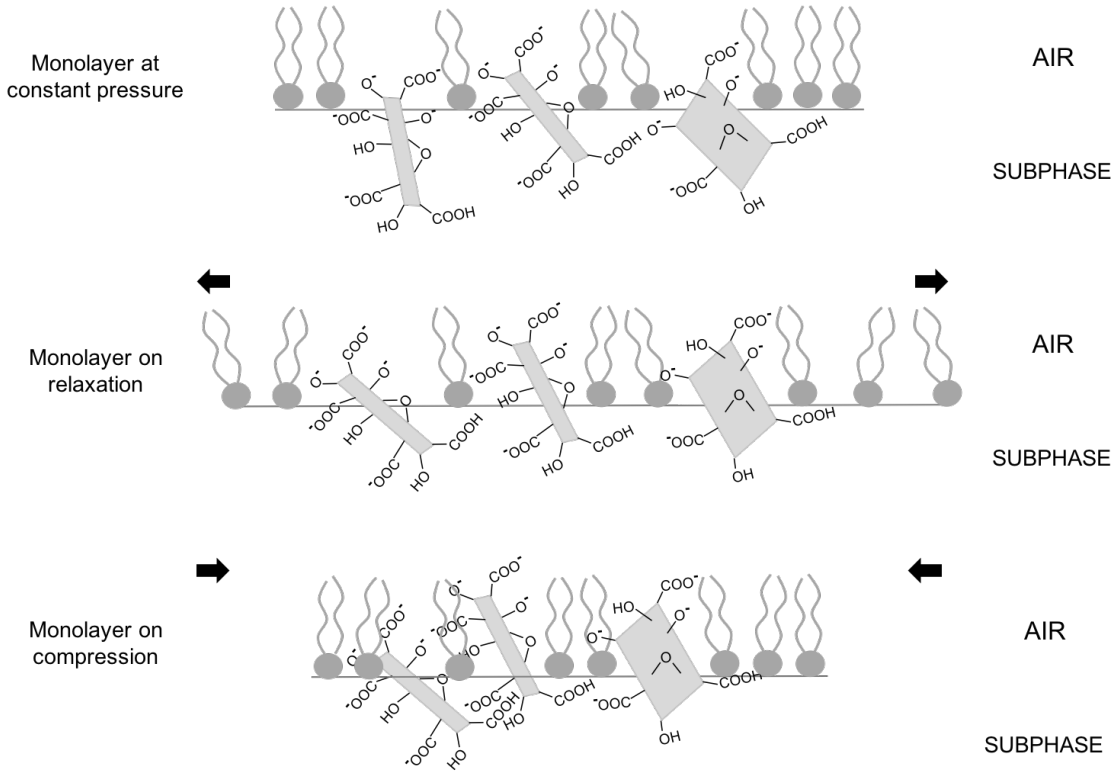

Figure 2.26 Proposed GO interactions with the outer monolayer at the phase transition. The outer leaflet is more compressible than the inner leaflet after addition of GO due to the absence of repulsive forces from PS lipids. Three possible interactions are proposed: GO can either be interacting with the lipid head groups; the fatty acid tails; or being extruded from the monolayer, affecting the molecular packing of the monolayer.

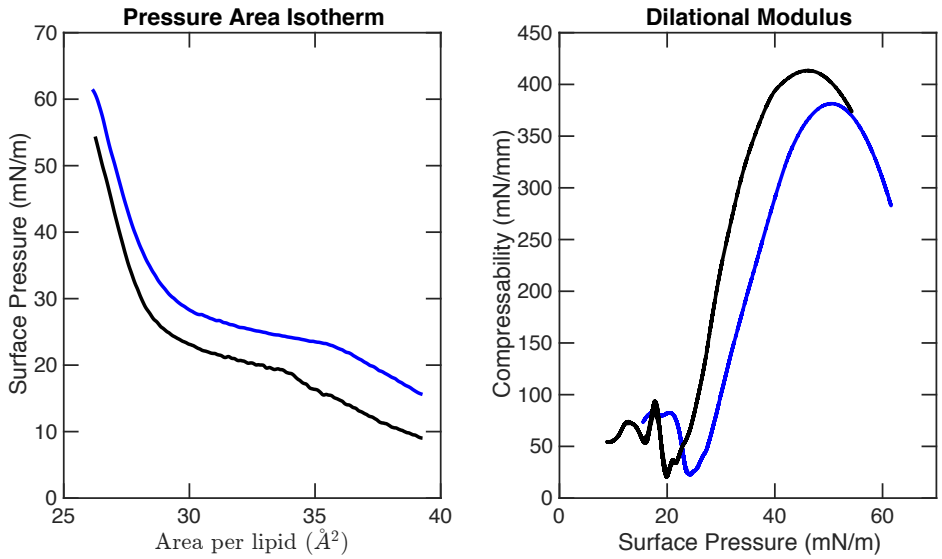

Figure 2.27 Pressure-Area isotherms (left) and Dilational modulus vs surface pressure (right) comparing a pure outer leaflet mixture (black) with outer leaflet with graphene oxide incorporated at a constant pressure of 28 mN/m (blue).

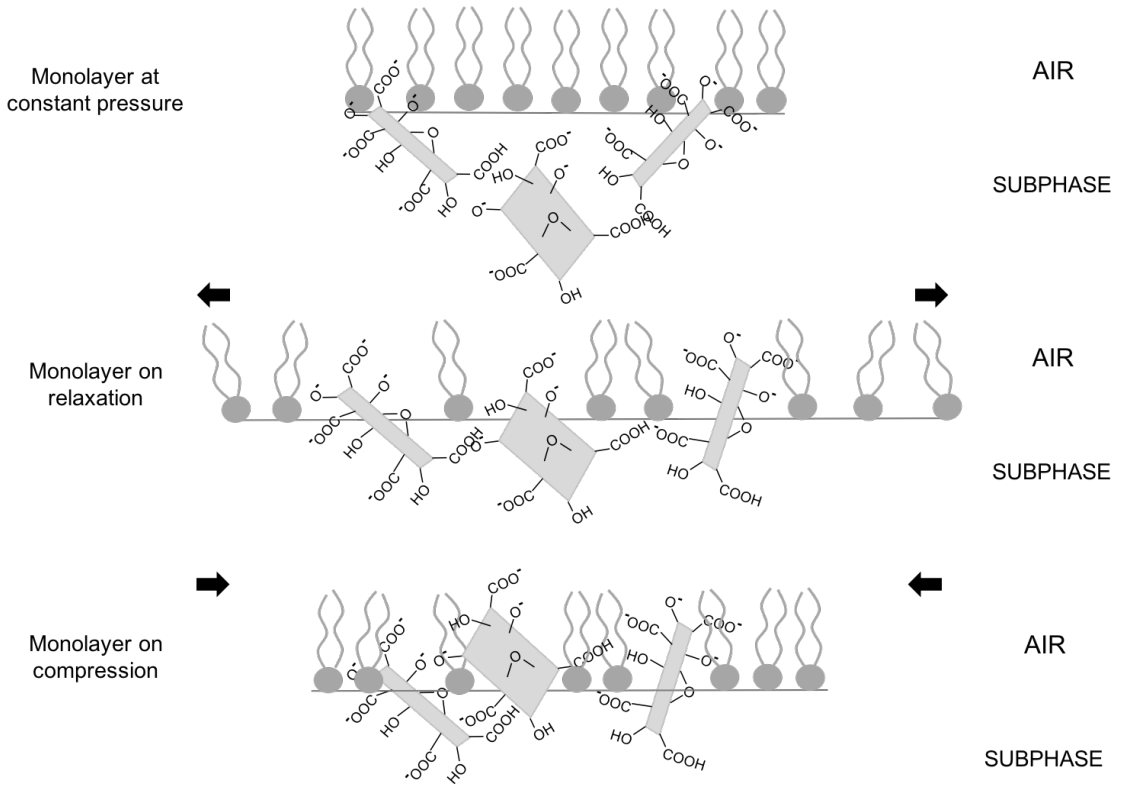

Figure 2.28 Proposed GO interactions with the outer monolayer at the condensed phase. It is proposed that GO is interacting weakly with the monolayer at constant pressure. Relaxation of the monolayer can incorporate further GO into the monolayer, due to the absence of repulsive forces. The compressibility is then equivalent to when the GO is added at the phase transition.

In the Langmuir monolayers (and vesicles and cells) GO flakes can orient either parallel or perpendicular to the plane of phospholipids and may or may not penetrate the bilayer. It is important to distinguish these modes of interaction and so a series of experiments were undertaken in which the phospholipid head groups were allowed to interact only with carbon planes. An important corollary of this work is that the layers formed could be used as a receptor in the development of electrochemical sensors. For this series of experiments, the Langmuir-Blodgett approach was used.

2.3.4 Langmuir – Blodgett Deposition and Characterisation of Lipid Layers on Silicon

In order to develop the methodology for Langmuir-Blodgett deposition of lipid layers onto carbon substrates and characterisation of the layers, DPPC monolayers were first deposited onto silicon substrates. For all layers deposited an average deposition ratio of 1.3 $\pm$ 0.3 (n=11) was calculated, at an optimum deposition rate of 1 mm/min. Wettability experiments were carried out to determine the nature of the silicon substrate and the orientation of the lipid monolayer deposited. Wettability of the bare silicon substrate gave a contact angle of ~ 15° indicating a hydrophilic surface. After deposition of a lipid monolayer, a contact angle of ~ 65° was calculated showing the modified silicon surface to be hydrophobic [Figure 2.29]. This is expected due to the hydrophilic head groups of the lipids interacting with the silicon surface, leaving the hydrophobic tails exposed. The contact angles calculated were consistent over the surface of the substrate, suggesting uniform layers had been deposited.

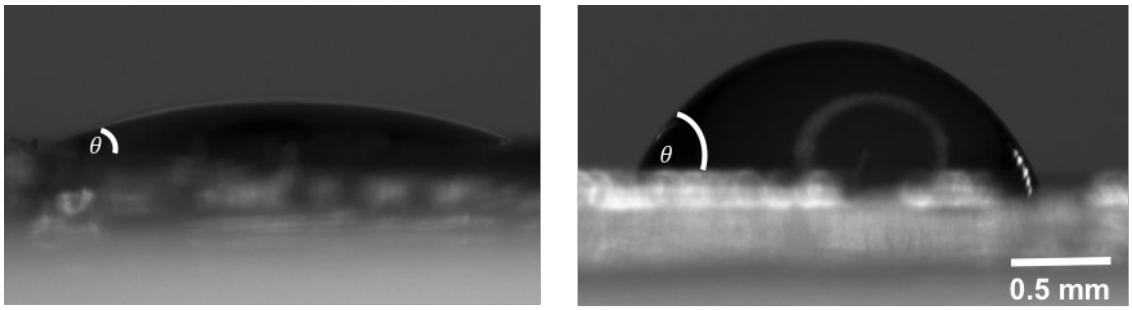

Figure 2.29 Images showing a silicon substrate (left) and monolayer deposited (right) on the surface. The water droplet technique was used to determine the wettability of the substrate. The left shown to be hydrophilic, and the right hydrophobic.

AFM was used to give a height profile of the sample to determine the thickness of the lipid layers. The difference in height between the bare silicon and the lipid DPPC monolayer deposited was shown to be 2.39 nm [Figure 2.30].

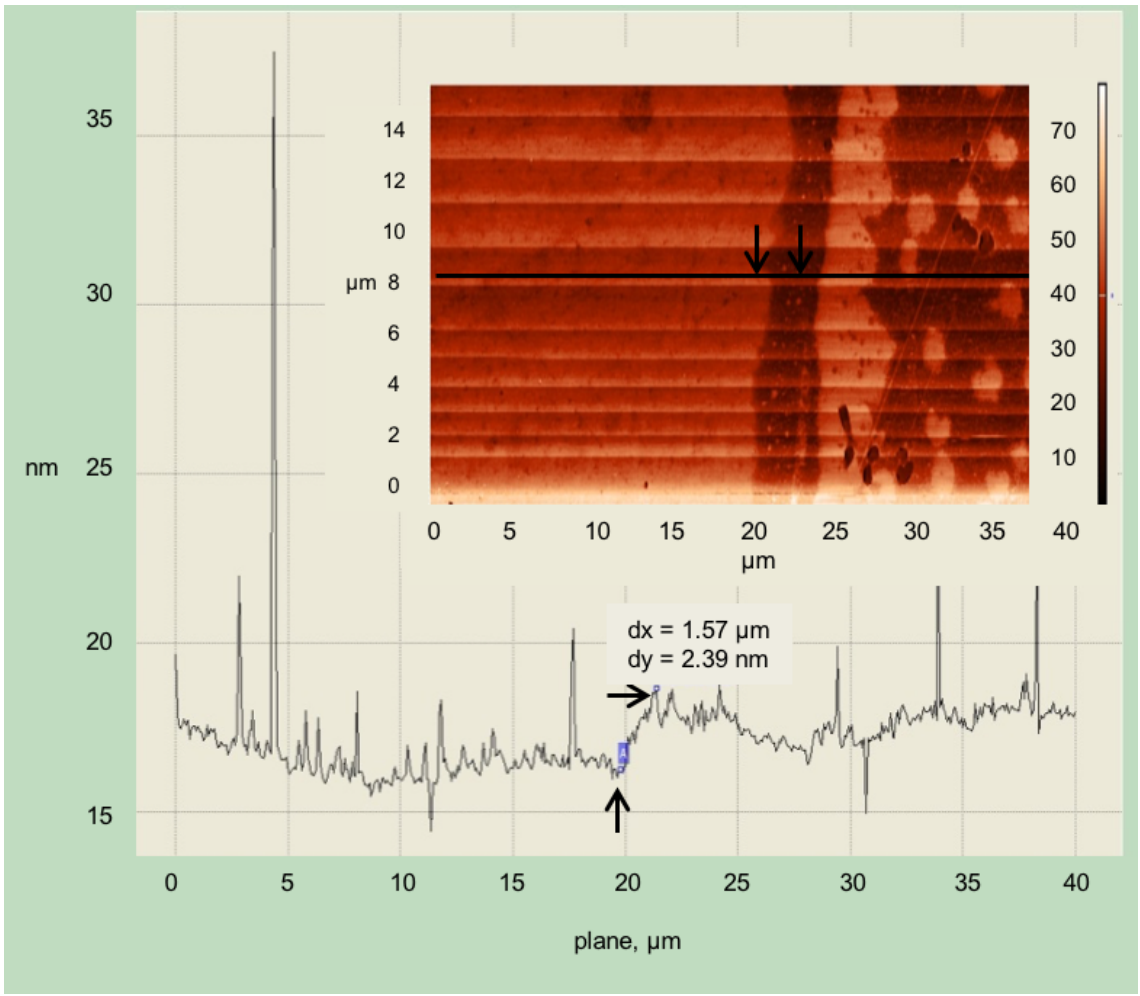

Figure 2.30 AFM image of a lipid monolayer deposited (right) onto a silicon substrate (left), with corresponding cross-section profile shown by the black line. The arrows indicate the points taken to determine the step height.

The average length of a phospholipid is ~ 2 nm, so the AFM result correlates well for a lipid monolayer deposited with lipids perpendicular to the substrate surface [Figure 2.31].

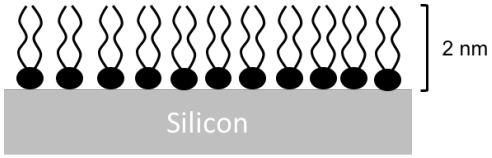

Figure 2.31 The predicted arrangement of a phospholipid monolayer deposited onto a silicon substrate

However, surface heterogeneities can be observed in the surface profile, as well as the image generated from the AFM scan. The image shows uniformity across a large surface area of the substrate, but there are obvious holes where the lipid has not been deposited, possibly due to surface defects which can be observed on the bare silicon wafer.

2.3.5 Electrochemical Analysis of Lipid Layers Deposited onto BDD

Lipid layers were deposited onto BDD and HOPG substrates: firstly, to determine whether lipid layers are deposited and if this can be characterised electrochemically, and secondly, to determine the sensitivity of the layer to the substrate used. First, DOPC, DPPC and DOPC:DPPC monolayers were deposited onto clean BDD substrates. For all monolayers an average deposition ratio of 1.4 $\pm$ 0.3 (n=13) was calculated, suggesting a uniform layer was deposited. Figure 2.32 shows the voltammetric response of $[Fe(CN)_6]^{3-/4-}$ at the BDD electrode with these monolayer deposited. For all bare electrode measurements, well defined anodic and cathodic peaks are observed. For all voltammograms, $\frac{Ip_c}{Ip_a}$ = ~ 1, except in the case of DPPC where complete blockage of electron transfer occurred. The voltammograms show a decrease in electron transfer from the bare BDD to BDD – DPPC. This could be due to the molecular packing on the substrate. DPPC is likely to pack efficiently on the surface due to its structure, consisting of two saturated hydrocarbon chains. DOPC molecules have one unsaturated bond in one of the hydrocarbon chains, which causes a kink in the tail preventing close packing between molecules. For DOPC, the

peaks are only slightly smaller than bare BDD, with ΔE_p = 185 mV. It is likely, therefore, that very little DOPC has been deposited onto the surface, leaving a significant area of the electrode available for electrolyte to react. The DOPC:DPPC monolayer shows a larger peak potential ΔE_p = 348 mV, indicating slower kinetics.

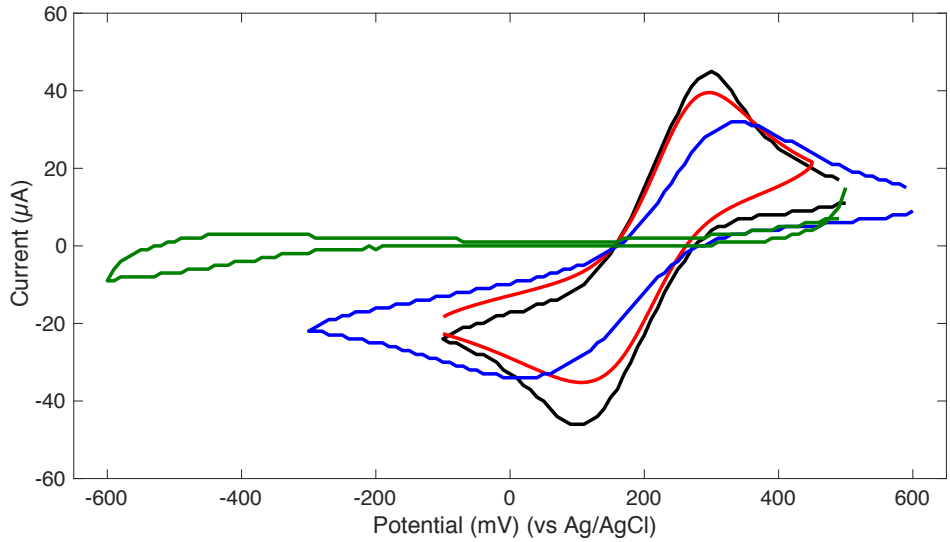

Figure 2.32 Cyclic voltammogram in 1 M KCl containing 1 mM $[Fe(CN)_6]^{3-/4-}$. Black – bare BDD electrode, Red – DOPC monolayer, Blue – DOPC:DPPC (1:1) monolayer, Green – DPPC monolayer

It has been previously reported by Ru *et al.* that DPPC molecules form a more continuous membrane on reduced graphene oxide sheets, using the Langmuir-Blodgett technique, compared to DOPC (99), possibly because DPPC is in a gel phase at room temperature whereas DOPC is a liquid phase and is more disordered.

A limitation of these experiments was the stability of the ferricyanide probe, which showed changes in the electrochemical response on bare BDD over longer time periods. At this stage, the charge structure of the electroactive species is not important so ruthenium hexamine was used for subsequent experiments (choice of redox probe is important for understanding charge structures of pores that form in the monolayers). Another limitation was the size and surface roughness of the BDD substrate which presents difficulties for uniform deposition of lipid layers. The size of BDD used in these experiments was 9.6 cm^2. For successful deposition of a monolayer, the transfer ratio should be

equal to 1, and so the area required of the Langmuir monolayer was a significant fraction of that of the trough used in these experiments. AFM analysis of BDD at various points across the substrate showed the surface to be rough, with a height range of 0 – 120 nm (60X the height of a phospholipid) [Figure 2.33]. This surface morphology is typical of BDD (100), however, for Langmuir-Blodgett deposition a smooth surface is required (101).

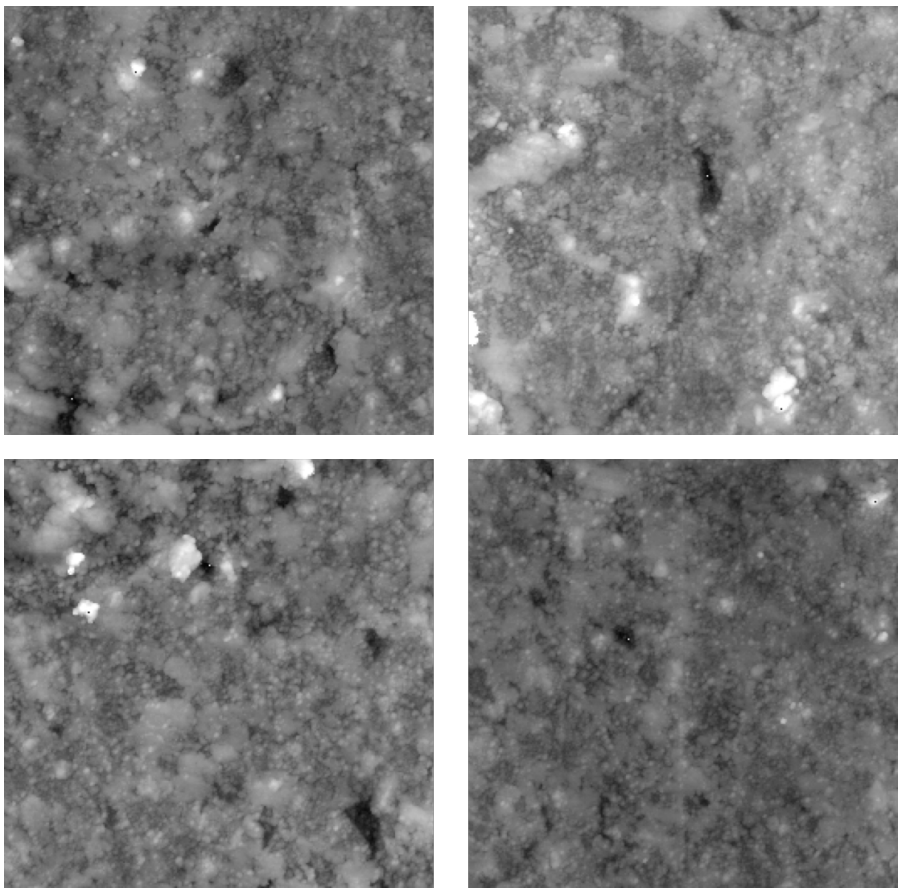

Figure 2.33 AFM topographical images of BDD at different points across the surface of the substrate. 2 dimensional view 10 x 10 μm scan. Colour range from black – white: 0 – 120 nm.

2.3.6 Electrochemical Analysis of Lipid Layers Deposited onto HOPG

As BDD was shown to be an unsuitable substrate for Langmuir-Blodgett deposition, HOPG was used to further investigate phospholipid interactions with

carbon substrates. To deposit a bilayer comparable to a cell membrane, the substrate initially has to be hydrophilic. The following experiments were conducted with hydrophilic HOPG. The predicted arrangement of the lipid bilayer on HOPG is shown in Figure 2.34.

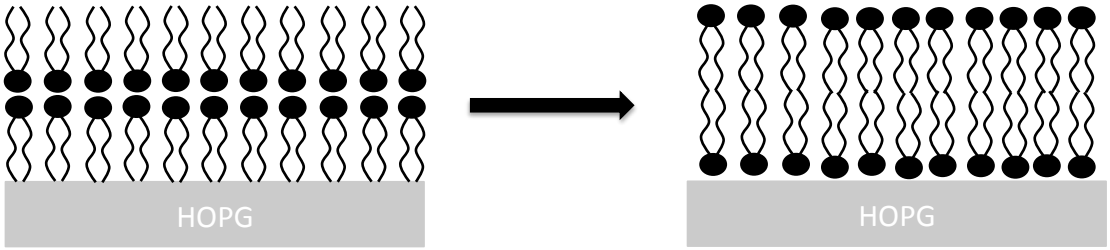

Figure 2.34 The predicted orientation of a phospholipid bilayer on a hydrophobic HOPG substrate, and hydrophilic HOPG.

The HOPG electrode was polarised at 1500 mV in 0.1 M NaOH, which causes the addition of surface oxygen, making the surface more hydrophilic (102). For all layers deposited an average deposition ratio of 1.00 ± 0.2 (n=9) was calculated. Figure 2.35 shows an example of one cyclic voltammogram of $Ru(NH_3)_6^{3+/2+}$ at the bare HOPG substrate, and with a DPPC bilayer deposited. The peak heights decrease significantly, however, there is still some electron transfer occurring. ΔE_p = 179, which suggests good kinetics i.e. the electrons can easily transfer between the solution and the electrode surface without anything on the surface blocking it. The dramatic decrease of the peak height suggests electron transfer is still occurring over a small fraction of the electrode surface, which indicates that there may be holes in the membrane.

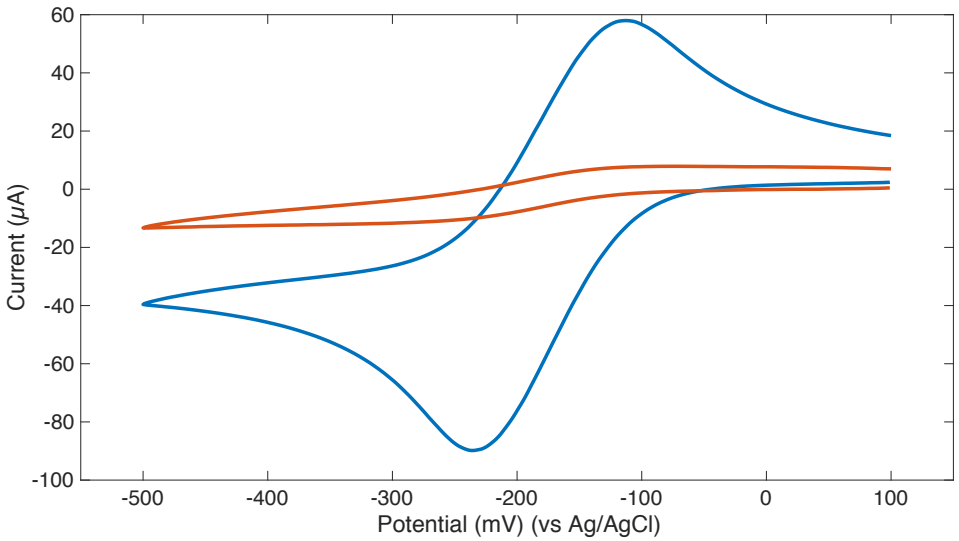

Figure 2.35 Cyclic voltammogram in 1M KCl containing 1mM $Ru(NH_3)_6^{3+/2+}$ at a potential sweep rate of 50 mV/s at a bare HOPG electrode (blue) and at a HOPG electrode with a DPPC bilayer deposited (red).

However, this was not a reproducible result, with repeat experiments showing great variation in the effects on electron transfer. Another example of a cyclic voltammogram produced depositing a DPPC bilayer onto HOPG is given in Figure 2.36, where there is a significant electron transfer occurring after bilayer deposition.

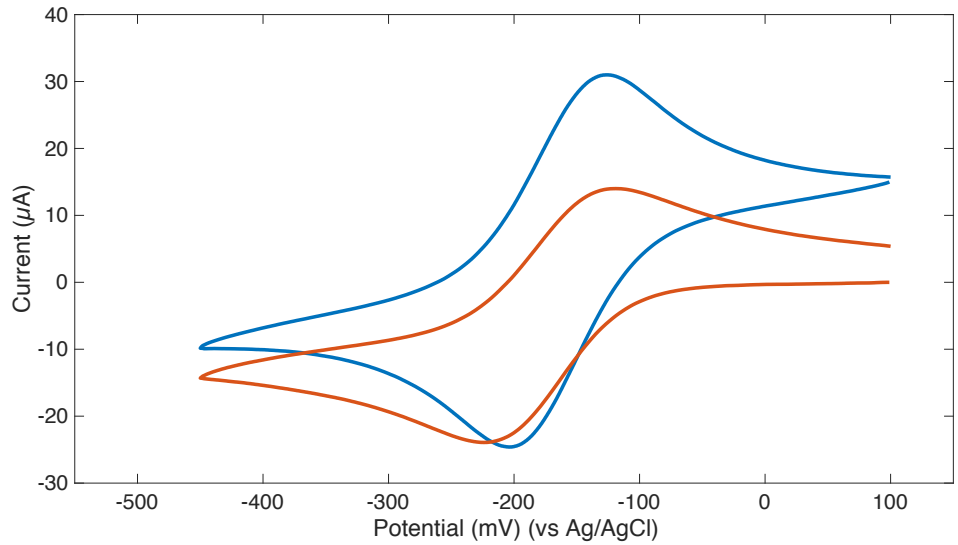

Figure 2.36 Cyclic voltammogram in 1M KCl containing 1mM $Ru(NH_3)_6^{3+/2+}$ at a potential sweep rate of 50 mV/s at a bare HOPG electrode (blue) and at a HOPG electrode with a DPPC bilayer deposited (red).

In order to form a more biologically relevant bilayer, a mixture of DPPC and Cholesterol, at a 80:20 molar ratio, was used in further experiments. Figure 2.37 shows an example of a cyclic voltammogram of $Ru(NH_3)_6^{3+/2+}$ at the bare HOPG and with a DPPC:Chol bilayer deposited. A more complete coverage of the electrode is observed, significantly slowing electron transfer down, where ΔE_p= 530. However, electron transfer has not been completely blocked, suggesting the electroactive species may be permeating the membrane.

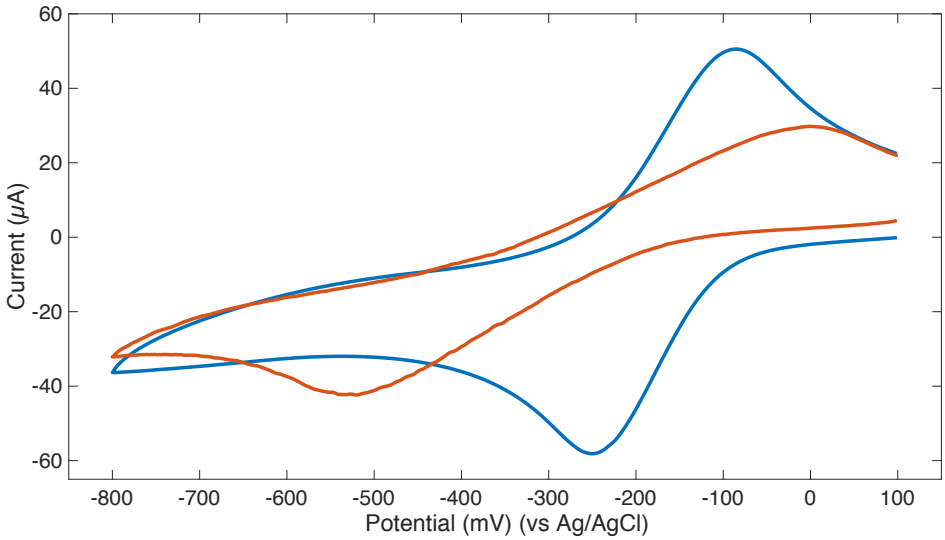

Figure 2.37 Cyclic voltammogram in 1M KCl containing 1mM $Ru(NH_3)_6^{3+/2+}$ at a potential sweep rate of 50 mV/s at a bare HOPG electrode (blue) and at a HOPG electrode with a DPPC:Cholesterol (1:1) bilayer deposited (red).

It is possible for the cholesterol to decrease the permeability of the bilayer deposited. This could make the bilayer harder to permeate and consequently block more electron transfer, or slow down the process. However, as shown in Figure 2.38, the results observed in Figure 2.37 were not reproducible.

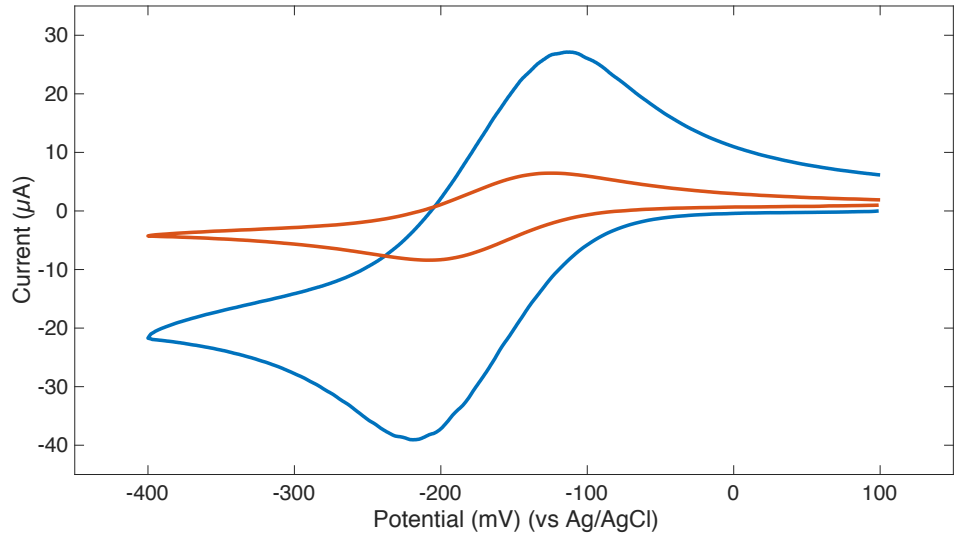

Figure 2.38 Cyclic voltammogram in 1M KCl containing 1mM $Ru(NH_3)_6^{3+/2+}$ at a potential sweep rate of 50 mV/s at a bare HOPG electrode (blue) and at a HOPG electrode with a DPPC:Cholesterol (1:1) bilayer deposited (red).

The cyclic voltammetry reveals the HOPG – DPPC:Chol bilayer and BDD – DPPC monolayer act most effectively as barriers to the charge transfer between electrolyte solution and electrode surface. However, none were totally effective and there was considerable variability between experiments which probably reflected the difficulty in depositing a continuous, uniform layer. One difficulty using HOPG arose from changes to its surface with successive cleaving between each experiment. Cleaving HOPG can cause step defects on the surface, therefore leaving the HOPG with a rougher surface, which could affect lipid deposition and the uniformity of the layers. Heterogeneity across the surface could result in inconsistent lipid deposition.

AFM scans of HOPG were taken at different cleaving steps to analyse the surface roughness of the substrate [Figure 2.39].

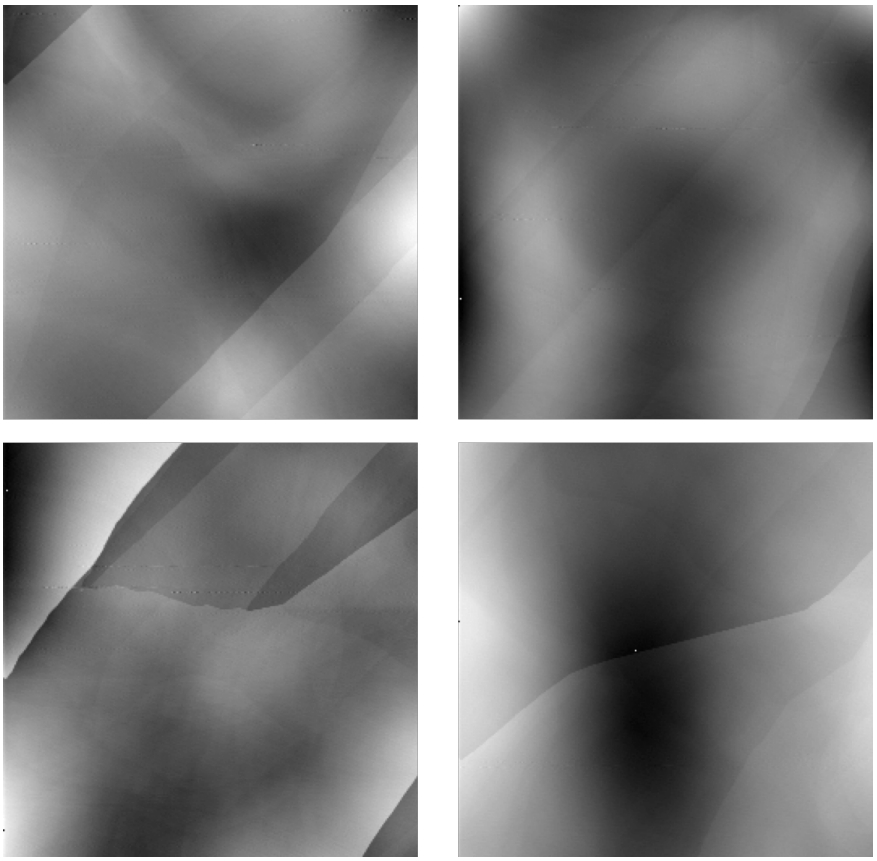

Figure 2.39 AFM topographical images of HOPG at different stages of cleaving to show the differences in surface roughness. 2-dimensional view 10 x 10 µm scan. Colour range from black – white: 0 – 20 nm.

The surface morphology showed a height range of 0 – 20 nm, with no significant difference between different stages of cleaving. This is a considerably smooth surface compared to BDD. The variability in electrochemical behaviour of BDD and HOPG results show no substrate is favourable to lipid deposition and, therefore, would suggest substrates smoothness is not a primary factor affecting lipid deposition. The transfer ratio for all experiments suggested uniform layers were deposited, however this was not shown in the electrochemical analysis. To successfully analyse the layers electrochemically to determine the arrangement of phospholipids on the substrates, and to finally develop a phospholipid biosensor, further investigation is required to determine the optimum conditions for lipid deposition and to identify any further external factors which could be affecting the electrochemical results.

2.4 Conclusions

From Langmuir monolayer studies it has been possible to record π-A isotherms and calculate the corresponding dilational moduli for the inner and outer leaflet lipids, before and after the incorporation of graphene oxide. The inner leaflet mixture forms a more compressible monolayer, that reaches higher pressures at a lower area per molecule. It is likely that this is an effect of PS molecules present in the inner leaflet mixture, as the only difference between the two, possibly providing increased stabilisation to the organisation of the lipid molecules and lipid domains. On addition of graphene oxide, an increase in trough area is observed for all monolayers indicating graphene oxide insertion. For the inner leaflet, initial graphene oxide is dependent on pressure, with more graphene oxide insertion when added at the phase transition pressure. At the condensed phase pressure, less graphene oxide is able to permeate the monolayer, a possible result of repulsive forces between the negatively charged PS head groups and oxygen-containing groups on the graphene oxide. For all isotherms recorded on addition of graphene oxide, there was an increase in the overall pressure of the monolayer, and a decrease in compressibility. It is likely that the graphene oxide is interacting with the head groups of the lipids, but there is a more significant interaction between the graphene oxide and PS lipids.

The Langmuir-Blodgett technique was used to deposit lipid layers onto BDD and HOPG substrates. These layers were analysed electrochemically in order to determine whether uniform lipid layers were deposited by measuring changes in electron transfer. This also has further potential to be used in biosensor applications. Although there was some success showing DPPC monolayers deposited onto BDD to completely block electron transfer, this result was not reproducible on HOPG. DPPC:DOPC and DOPC layers were also deposited onto BDD substrates, showing little effect on the electrochemistry. The results have shown unsuccessful deposition of uniform lipid mono- and bilayers, with incomplete coverage of carbon substrates, AFM analysis showed great difference in surface roughness but no significant difference in the electrochemical behaviour of either substrate, suggesting this was not the factor contributing to the unsuccessful results. Before developing a phospholipid

biosensor, further work is required to determine the optimum parameters for lipid deposition and to investigate any other external factors which could be contributing to the variable results.

Chapter 3 The Effects of Graphene Oxide on Bilayer Vesicles

This chapter will describe two groups of experiments, investigating the interactions of graphene oxide with lipid bilayer vesicles. In the first group, giant unilamellar vesicles are used to investigate permeability characterised by phase contrast microscopy. In the second group, changes in permeability are investigated using self-quenching fluorescent vesicles, pre-loaded with fluorescein, measuring the change in fluorescence intensity before and after graphene oxide exposure. In order to validate the methodology and to provide a comparator for the permeability changes, another group of experiments were undertaken using a range of known membrane-targeting toxins.

3.1 Introduction

Unilamellar lipid bilayer vesicles are an excellent model membrane system used for many biophysical and biochemical investigations (103). The vesicle is the closest artificial structure to that of a biological cell membrane. The simplest way to produce vesicles is by evaporating lipids in a solvent solution (eg. chloroform) then to re-suspend them in an aqueous solution (eg. sucrose). Due to the amphiphilic properties of the lipids, they will spontaneously self-assemble into a structure that is energetically favourable. Vesicle formation can produce unilamellar and multilamellar vesicles [Figure 3.1]. As unilamellar vesicles are formed of one lipid bilayer, they are more biologically relevant.

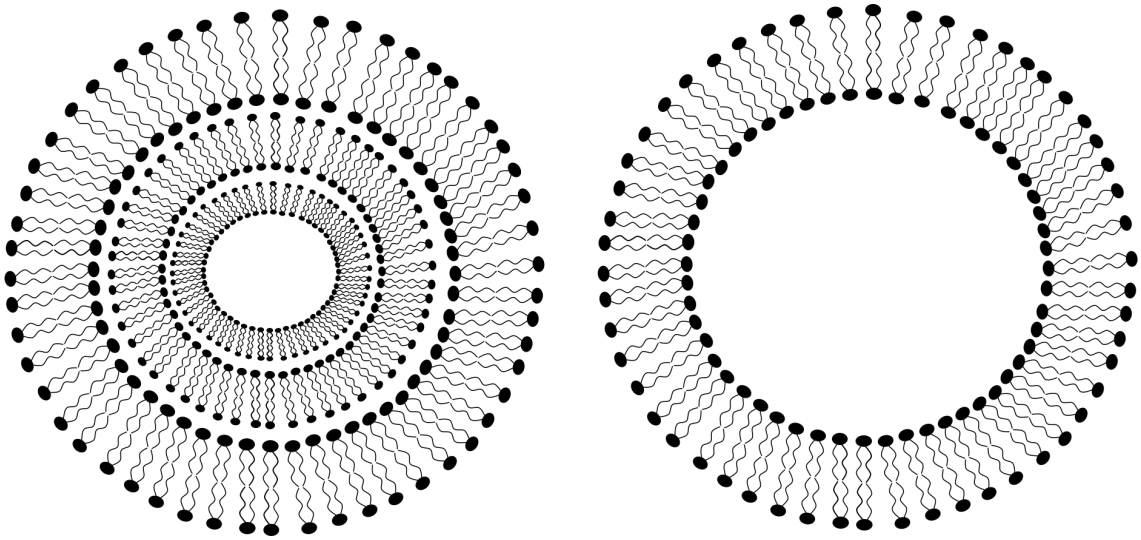

Figure 3.1 Diagram illustrating a giant multilamellar vesicle, MLV (left) and a giant unilamellar vesicle, GUV (right). Vesicle size and membrane thickness are not to scale.

Pure lipid vesicles can be made, but more importantly, it is possible to make vesicles with a specific lipid composition, in order to mimic the lipid composition of a particular cell membrane. This also allows the roles of different types of lipid to be determined, and their contribution to membrane properties and interactions.

Using different preparation methods (103), various sizes of vesicles can be produced with diameters ranging from ~20 nm to ~100 μm. Unilamellar vesicles can be categorised according to their size: Small (20-100 nm), large (100 nm – 1 μm), and giant (1 – 100 μm). These are referred to as SUV's, LUV's and GUV's, respectively. SUV's have rather different mechanical properties to cell membranes, but LUV's and GUV's closely resemble cells.

3.1.1 Giant Vesicles

Giant vesicles are a widely used membrane system, and are one of the types of vesicles used in this experiment. Giant vesicles can either be prepared by the swelling technique which results in both uni- and multilamellar vesicles, or the electroformation method (104) [Section 3.2.1] which produces mostly unilamellar vesicles. This method of vesicle formation is poorly understood, but it is proposed that applying an AC current induces mechanical stress on the dried lipid film

suspended in an aqueous solution, separating and destabilising the lipid film allowing spontaneous formation of vesicles (105).

It has been shown experimentally that vesicles can adopt various shapes. Shape transitions can be induced by a number of factors. A change in temperature will induce prolate vesicles to undergo a process called budding (106). Changes in osmotic pressure can induce changes to the area-to-volume ratio: when the solute concentration is higher than the solution inside the vesicle, it deflates (107). Also, using different solutes, at the same osmotic concentration inside and outside of the vesicle, can affect the spontaneous curvature causing a change in shape (108). It is important to control these factors to ensure the stability of the vesicles. Vesicle shape can be predicted from its area, reduced volume and spontaneous curvature using the Area-Difference-Elasticity (ADE) model, used to model membrane bending elasticity (109). Figure 3.2 shows the different shape deformations of a GUV under different osmotic pressure changes.

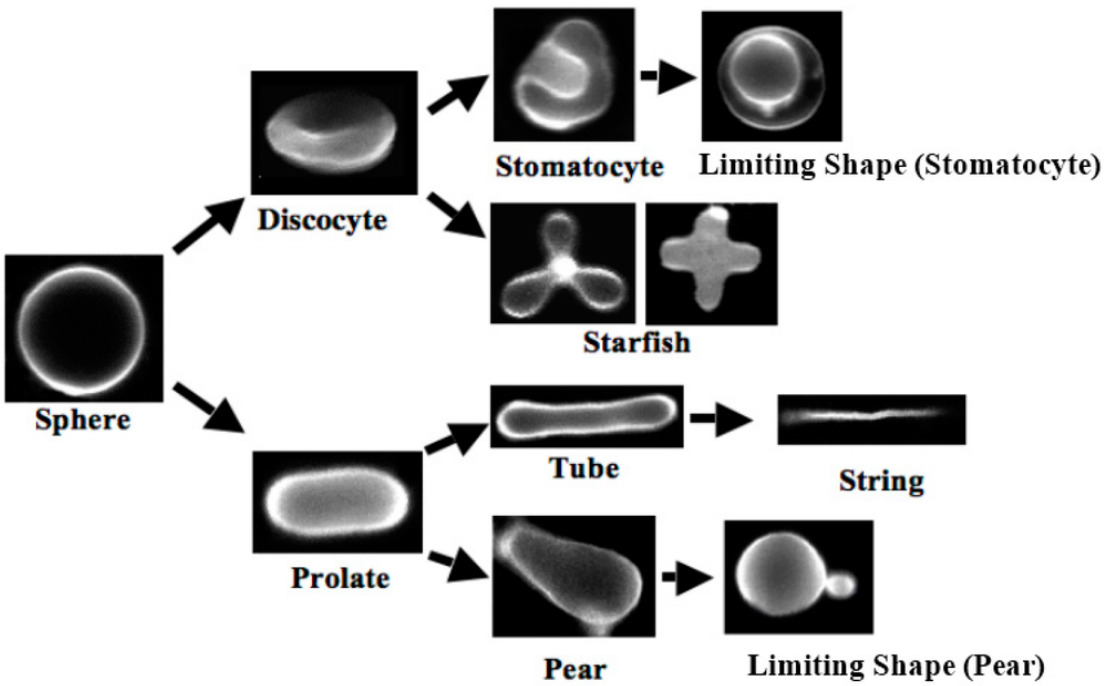

Figure 3.2 Shape deformation pathway of a GUV, showing the different shape changes produced by an osmotic pressure difference (from (110)).

Giant vesicles produced using the electroformation method are mainly spherical in shape with a single closed bilayer, which can float freely in aqueous solution. GUV's are especially useful for optical microscopy due to their cell-like size and shape (111). They are also used to study mechanical properties of the membrane because they exhibit large thermal fluctuations (112). This technique will be further described in Chapter 4.

3.1.2 Permeability of Bilayer Vesicles

One of the primary functions of biological membranes is to provide a barrier between two regions. This barrier is selectively permeable to ions and organic molecules and controls the movement of substances in and out of the cell. The phospholipid bilayer can greatly modify the permeation of molecules into a cell, with the composition of lipids found in the membrane having a vital role in permeability. For example, one study has shown membrane permeability to antibiotics is dependent on lipid composition, where anionic lipids decrease the permeability, whereas neutral lipid vesicles are more permeable (113).

By analysing phase-contrast images of vesicles, it is possible to determine the permeability of the vesicles. This approach exploits the clear difference in intensity inside and outside the vesicle, using phase contrast microscopy. This allows for a label-free measurement of graphene oxide permeation. To quantify this measurement, a permeability coefficient can be calculated. This method has been used to study diffusion of antibiotics (113) and will be further discussed in Section 3.3.1.

The aim of this experiment [Section 3.2.2] is to investigate the permeability of bilayer vesicles towards graphene oxide, to determine whether graphene oxide can enter vesicles without disruption. A DOPC unilamellar vesicle model has been used in this thesis.

3.1.3 Self – Quenching Fluorescence Vesicles

During the process of making phospholipid vesicles it is possible to encapsulate molecules within the vesicles. Fluorescent tracer molecules can be incorporated into the internal fluid phase of the vesicles during formation and changes in fluorescence with time provide a marker for permeability. In this research a slightly different approach was used. The vesicles were loaded with a dye at a sufficiently high concentration that fluorescence was self-quenched. Permeabilisation of the lipid bilayer releases the dye from the vesicle, thereby diluting the remaining dye and 'switching on' the fluorescence [Figure 3.3]. This technique is very sensitive and has been developed in studies on the interactions of toxins with membranes (114).

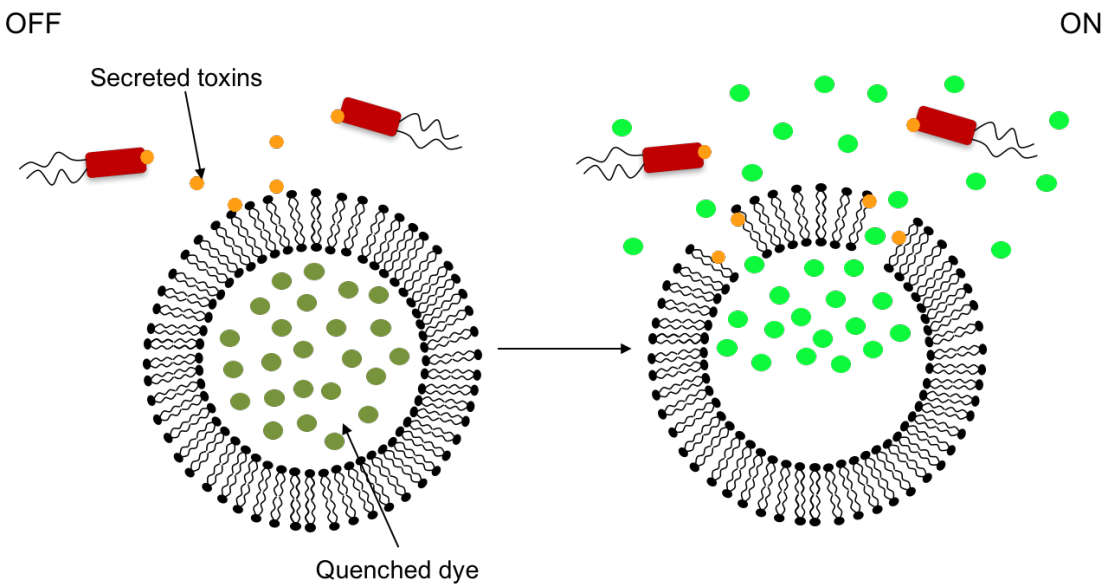

Figure 3.3 Scheme showing a lipid bilayer vesicle containing self-quenched fluorescent dye being permeated by secreted bacterial toxins, resulting in releasing dye and causing a fluorescence 'switch on'.

Previous work has been carried out using these vesicles to investigate the interactions of bilayer-targeting toxins, where a fluorescent dye is released from the vesicle when in contact with the active toxin (114). In this study, vesicles with varying cholesterol concentration were investigated, using carboxyfluorescein as the fluorescent dye. The vesicle membrane consisted of a lipid mixture (DPPC,

DPPE, CHO, SM) to which was added 10, 12-tricosadiynoic acid (TCDA). TCDA is a photo-polymerised fatty acid which creates domains within the vesicle, separate to the fluid phospholipid domains containing DPPC and DPPE. TCDA gives the vesicles a high stability and makes them more robust.

In the present research, the effects of graphene oxide on membrane permeability were compared with pore-forming toxins, whose effects are well characterised. Two toxins were used in this thesis, α-haemolysin, produced by the bacterium *Staphylococcus aureus* and NetB, produced by *Clostridium perfringens*. The two toxins are similar in structure, however, they differ in their pore-forming mechanisms. α-haemolysin forms pores by binding to lipids within the membrane containing a phosphocholine head group (115), whereas NetB does not bind PC efficiently, and has an affinity towards cholesterol (116). Here, the aim is to investigate how graphene oxide interacts with the self-quenching fluorescent vesicles, firstly to determine if graphene oxide permeates the vesicles, and then the extent to which the vesicles are lysed or permeabilised.

3.2 Experimental Methods

3.2.1 Electroformation of GUVs

The electroformation method was used to form GUVs, developed by Angelova *et al* (105). Plastic slides coated in Indium tin oxide (ITO), (75 mm x 25 mm), (thickness 1 mm, resistivity 60 Ω/m^2, Sigma Aldrich, UK) were used. A Teflon ring (thickness 5 mm, outer diameter 30 mm, inner diameter 25 mm) was first washed with methanol, then 2 – 3 times with chloroform. A 50 μl Hamilton syringe was also cleaned with methanol followed by chloroform, then used to apply uniformly 10 μl of the DOPC lipid solution in chloroform (10 mg/ml) on the conductive face of the ITO slide, inside the circle marked out by the Teflon ring. The ITO plate was placed in a vacuum chamber for 2 hours to allow the chloroform to evaporate and for a thin uniform lipid film to form. The electroformation chamber was constructed from this ITO slide and another ITO slide separated by the Teflon ring, the conductive faces being on the inside of the chamber. Clips were used to secure the chamber, applying pressure in order to contain the swelling solution [Figure 3.4].

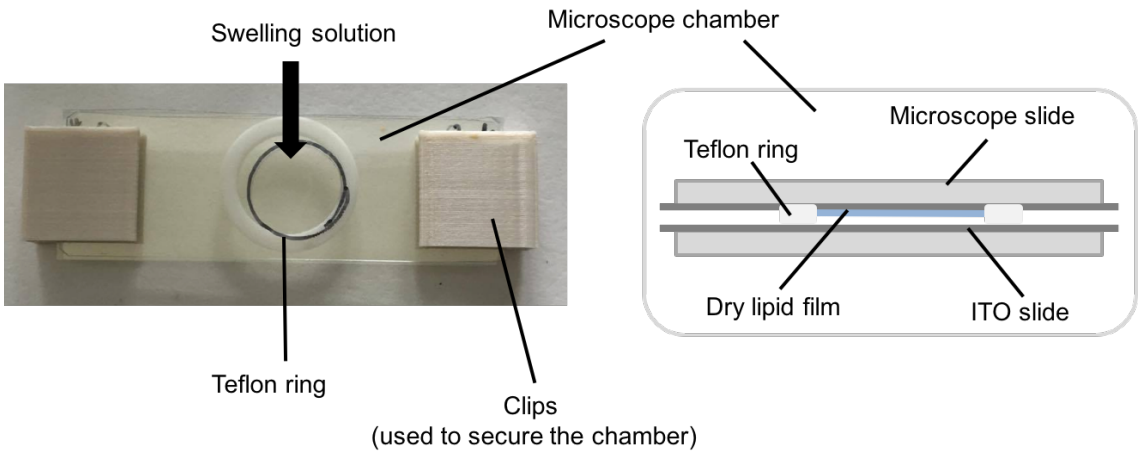

Figure 3.4 Electroformation chamber, formed from a Teflon ring and two ITO slides, sandwiched between two microscope slides. The swelling solution is injected into the chamber through a small slit in the Teflon ring.

1 ml of swelling solution, consisting of 100 mM or 200 mM sucrose, was injected into the chamber. The chamber was incubated at 37°C. Alternating current was then driven between the two ITO surfaces. Initially, a 1.2 V peak to peak square wave at a frequency of 10 Hz was applied for 1h, followed by a 1.5 V peak to peak sinusoidal wave at a frequency of 4 Hz for 1/2 h. The frequency was then adjusted to 2 Hz for 15 min, then to 1 Hz for a further 15 min. The electroformation chamber was then removed from the incubator and allowed to cool down for 20 min. The vesicle solution was then transferred to a glass bottle, sealed with Parafilm, and stored at 4°C.

3.2.2 Imaging of Giant Vesicles and Analysis

Phase contrast microscopy was used to image the vesicles. An optical density difference was achieved by using different sugar solutions inside and outside of the vesicle. Here, sucrose was used as an internal swelling solution, and glucose as the external. The sugars have different molecular weights but were present in equal concentrations. These sugars generated the required difference in refractive index without altering the osmotic pressure across the membrane. It is important to ensure the osmolarities of the internal and external solutions are equal to avoid vesicles rupturing due to a change in osmotic pressure. Vesicles were observed using an Olympus BX60 microscope set up for phase-contrast, with a 40X/0.75 Ph2 objective lens. A Mako G-234C camera was used to capture the images. 1 mg/ml graphene oxide solution was prepared in 200 mM glucose buffer. The microscope chamber was built using a glass microscope slide and cover slip. Both were cleaned first with detergent, and then methanol, then dried using lintless tissue paper. Strips of parafilm were used to separate the slide and cover slip and were arranged as shown in the diagram [Figure 3.5]. The depth of the chamber is controlled by the number of layers of Parafilm used: for these experiments only one layer of Parafilm was used. The chamber was constructed then placed on a hotplate at ~ 100ºC to seal the chamber. The vesicle suspension and graphene oxide solution were mixed before adding to the microscope chamber. The vesicle suspension was injected into the chamber, and the four

openings were sealed using molten wax. This was to prevent the otherwise rapid evaporation of the vesicle solution.

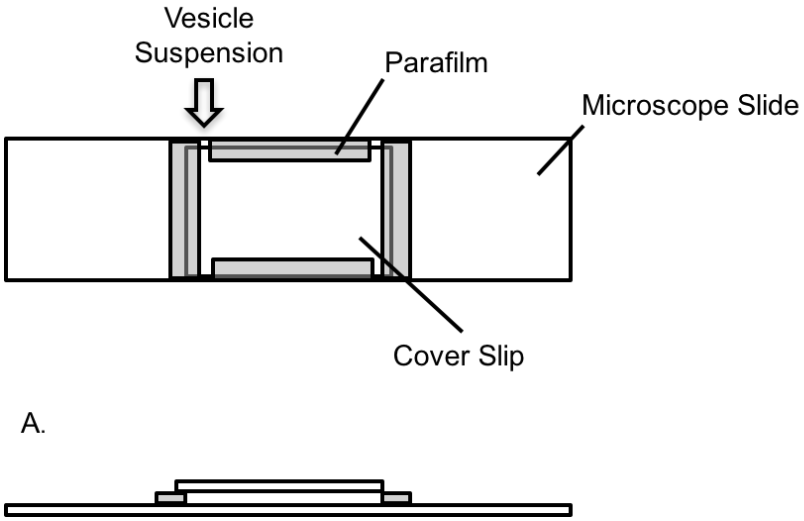

Figure 3.5 Vesicle chamber built using a glass microscope slide and cover slip, separated by one layer of Parafilm. The vesicle solution is added to the chamber at one of the openings and then the chamber is sealed using molten wax.

Images were then taken of suitable sized, unilamellar vesicles every 10 min for 1h. The images were then analysed using MATLAB [Section 3.3.1].

3.2.3 Preparation of Self – Quenching Fluorescent Vesicles

Self-quenching fluorescent vesicles were prepared using a mixture of lipids including, 16:0 PC (DPPC), 16:0 PE (DPPE), cholesterol and a cross-linker molecule, 10,12-Tricosadiynoic acid (TCDA). The method used was essentially that described by Laabei et al (114), producing vesicles of sizes ~ 90 – 110 nm. Each component was separately dissolved in 1 ml of chloroform to a concentration of 0.1moldm^{-3}. The stock solutions were stored in glass vials at -20C. Vesicle suspensions were prepared by mixing lipid and fatty acid components using 25mol\% TCDA, 53mol\% DPPC, 2mol\% DPPE and 20mol\% CHO. This mixture was dried under a nitrogen flow to form a lipid film on the

inside of the glass vial. The dried lipid was rehydrated using 5 ml of 5(6)-carboxyfluorescein (CF) buffer solution, vortexed and heated in a hot water bath at 75C for 10 min. Freeze/thaw cycles were carried out by initially immersing the lipid-containing vial in liquid nitrogen and then heating the vial back to room temperature to homogenise the solution. This was repeated three times. A turbid solution was an indication of vesicle formation. Vesicles were then extruded five times at 55°C using a Liposofast vesicle extruder (Avestin, USA) through 2 X 0.1 μM polycarbonate filters under nitrogen pressure. Water was initially run through the extruder to ensure removal of ethanol from the previous cleaning procedure. The initial opaque vesicle solution became translucent after extrusion. To remove any un-encapsulated CF dye, the vesicle solution was purified using Illustrate Nap-25 columns. First, the columns were washed with 15 ml of 4-(2-hydroxyethyl)-1-piperazineethanesulfonic acid (HEPES) buffer to remove the 0.15% Kathon CG/ICP biocide, which is present in the column as a preservative. (It is crucial that the biocide is removed to prevent false readings later on.) Then 2.5 ml of vesicle solution was added to each column and allowed to load. 1 ml of HEPES buffer was added and left to drain. After this, a further 2.5 ml of HEPES buffer was added and the resultant pure vesicle was collected and stored at 4°C for 2h. The TCDA molecules present in the lipid vesicles were then cross-linked and photo polymerised using a CL1000 Ultraviolet cross linker (Hamamatsu, Japan) for 6s [Figure 3.6].

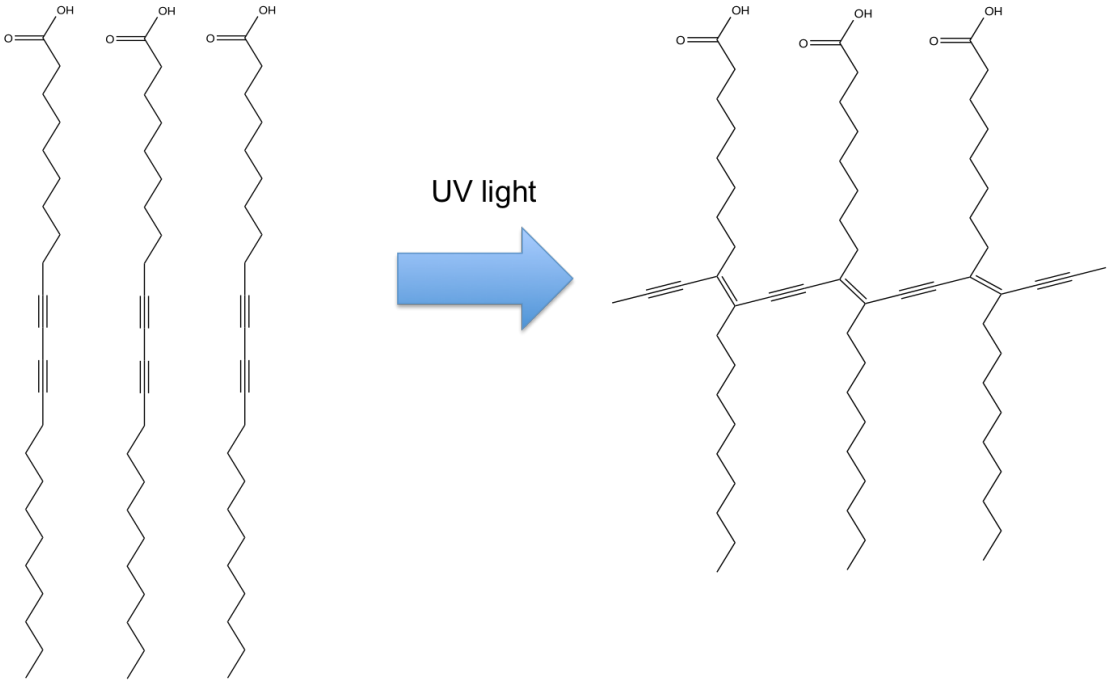

Figure 3.6 Scheme to show the conformational change of 10,12-Tricosadiynoic acid (TCDA) molecules, one of component of the lipid vesicles, after exposure to UV light. Cross-linking of these molecules gives the vesicles high stability.

3.2.4 Fluorescence Intensity Assay

The fluorescence intensity was measured using a fluorescence plater reader (Tecan Pro Infinite 200), at excitation and emission wavelengths of 485 nm and 520 nm respectively. For graphene oxide measurements, 50 µl of vesicle solution was mixed with 50 µl of graphene oxide suspended in HEPES (Sigma Aldrich, UK) buffer, in a 96-well plate. The graphene oxide concentration ranged from 0.01 mg/ml to 0.1 mg/ml. The well plate was incubated in the fluorimeter at 37°C for 1h. Measurements were taken over 30 kinetic cycles with 2 min intervals. Each experiment was performed in duplicate. Positive (0.1% Triton X-100, Sigma Aldrich, UK) and negative (HEPES buffer) controls were used to normalise fluorescence. The same method was used for initial experiments testing the following pore-forming toxins: α-haemolysin (0.5 mg/ml, List Biological Laboratories Inc, USA) and NetB (0.45 mg/ml) which was isolated from *C.*perfringens, cloned and purified before use by another group using the methodology detailed in (116).

3.3 Results and Discussion

This section includes all results for graphene oxide permeability experiments carried out using giant vesicles and self-quenching fluorescent vesicles, including a comparative study with pore-forming toxins.

3.3.1 Permeability of Giant Vesicles

To calculate the permeability coefficient, first, the normalised fluorescence intensity differences between the inside and the outside of the vesicle at $t = 0$ (ΔI_1) and at $t = t_f$ (ΔI_2) were calculated using the following equations:

$$\Delta I_1 = \frac{I_{out} - I_1}{I_{out}}; (t = 0) \tag{3.1}$$

$$\Delta I_2 = \frac{I_{out} - I_2}{I_{out}}; (t = t_f) \tag{3.2}$$

where I_1 and I_2 correspond to the average internal intensities measured around the centre of the vesicles at times $t = 0$ and $t = t_f$. I_{out} is the intensity outside of the vesicle. The relative intensities ΔI_1, before the addition of graphene oxide, and ΔI_2, a time point after graphene incubation, can be calculated (using MATLAB). The following equation calculates the permeability coefficient,

$$-P = \frac{R}{3t}\ln(\Delta I_2 - \Delta I_1 + 1) \tag{3.3}$$

where P is the permeability coefficient, R is the vesicle radius and t is the time taken from initial vesicle detection to the first point of detection after GO treatment.

Figure 3.7 shows an example of a giant vesicle (~ 8.5 μm) in a glucose external swelling solution without treatment with graphene oxide, monitored over

1h. The WU fluorescence filter cube was used as it gave the optimum contrast between inside and outside the vesicle. There are no changes in intensities or differences in contrast observed over 1h. Figure 3.8 shows a series of images taken of a giant vesicle, exposed to 1 mg/ml graphene oxide in glucose showing loss of contrast after 10 min exposure with complete loss of contrast observed after 60 min. For all measurements, a 10 minute period was given to find a suitable vesicle.

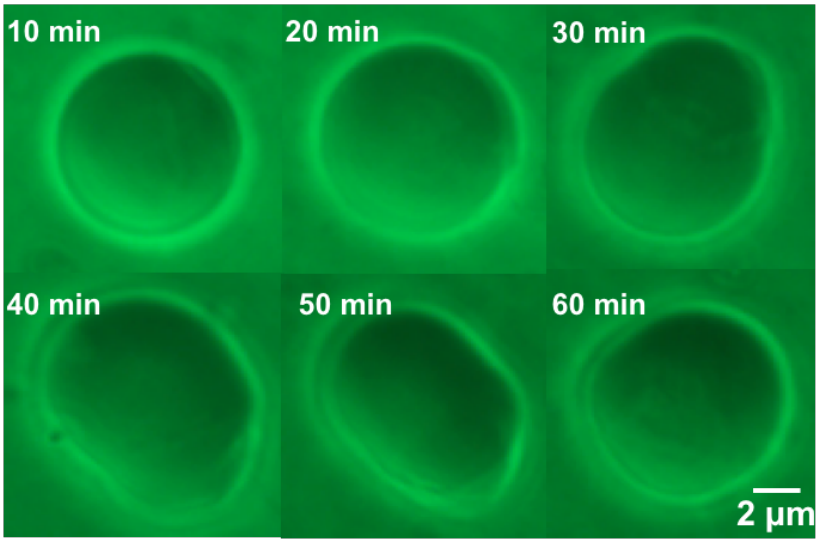

Figure 3.7 Snapshots of a giant vesicle viewed using phase-contrast microscopy (40X/0.75 Ph2 objective), taken every 10 min over 1 h. (left to right, 10 min to 60 min).

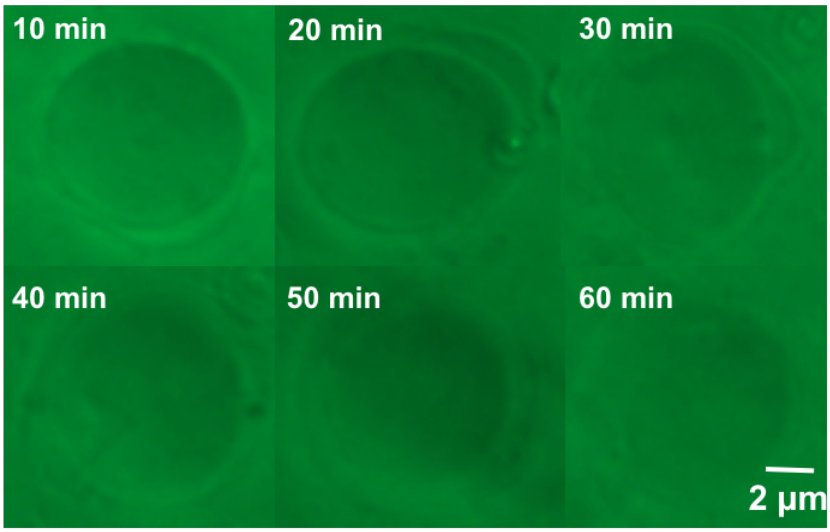

Figure 3.8 Snapshots of a giant vesicle, treated with 1 mg/ml graphene oxide suspended in a 200 mM glucose solution. Images were taken every 10 min for 1 h (left to right).

Using equations 3.1 – 3.3, the permeability of the giant vesicles can be calculated. Figure 3.9 shows an average of the permeability coefficients obtained from the samples used. After 10 minutes of exposure to graphene oxide the average permeability coefficient was $0.72 \pm 0.05 \times 10^{-3}$ cm s^{-1} increasing to $0.99 \pm 0.05 \times 10^{-3}$ cm s^{-1} after 1h (n=5). This is an obvious increase in permeability compared to the control vesicles where an average of $0.16 \pm 0.02 \times 10^{-3}$ cm s^{-1} was obtained [Figure 3.10]. The greatest increase in permeability is observed at t=10 min, suggesting GO permeation of the vesicles occurs initially. The permeability coefficient stays reasonably constant throughout the experiment, with only a slow increase to 0.27×10^{-3} cm s^{-1} observed over 1h, which could mean the vesicle becomes saturated by GO. It is possible that further GO from the solution permeates the vesicle after the initial saturation, however it does not seem to have a significant effect.

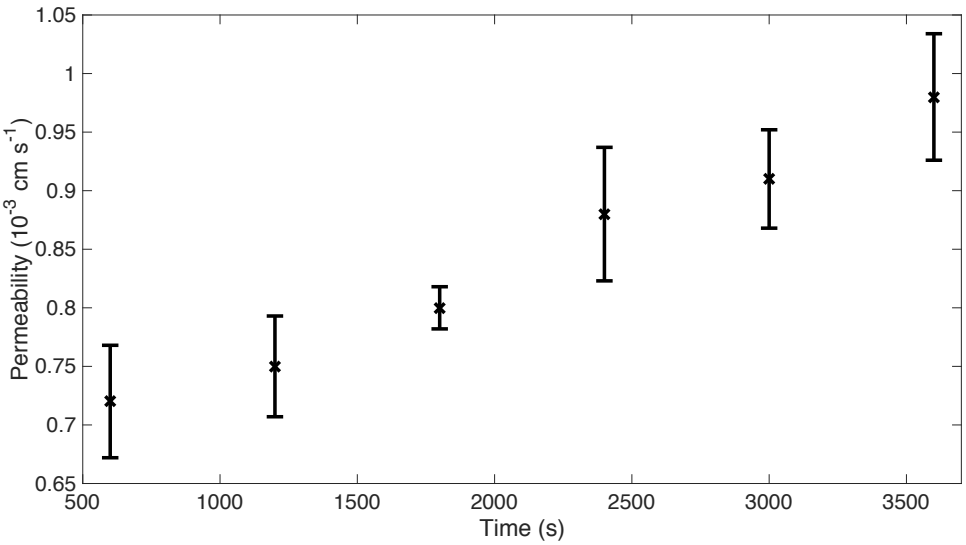

Figure 3.9 The average calculated permeability coefficients over 1 h for DOPC vesicles treated with 1 mg/ml graphene oxide suspended in 200 mM glucose (n=5).

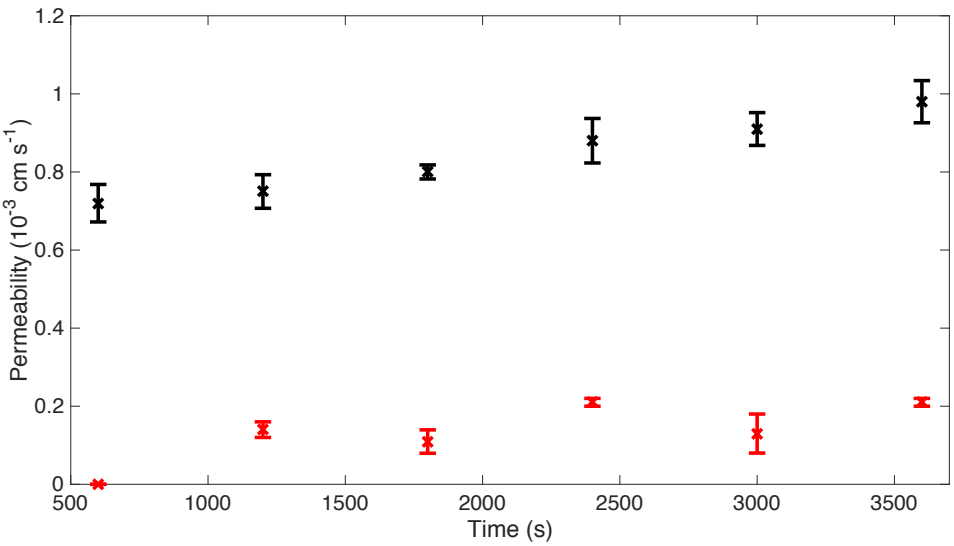

Figure 3.10 A comparison of the averaged calculated permeability coefficients for DOPC vesicles treated with 1 mg/ml graphene oxide in 200 mM glucose (black), with control vesicles treated with 200 mM glucose (red).

Figure 3.11 shows the proposed interactions of GO with a vesicle. Possible permeation could occur from “edge on” GO due to its smaller width compared to “side on” GO, forming holes within the bilayer. It is possible “side on” GO is interacting with head groups of vesicles, saturating but not entering the vesicle.

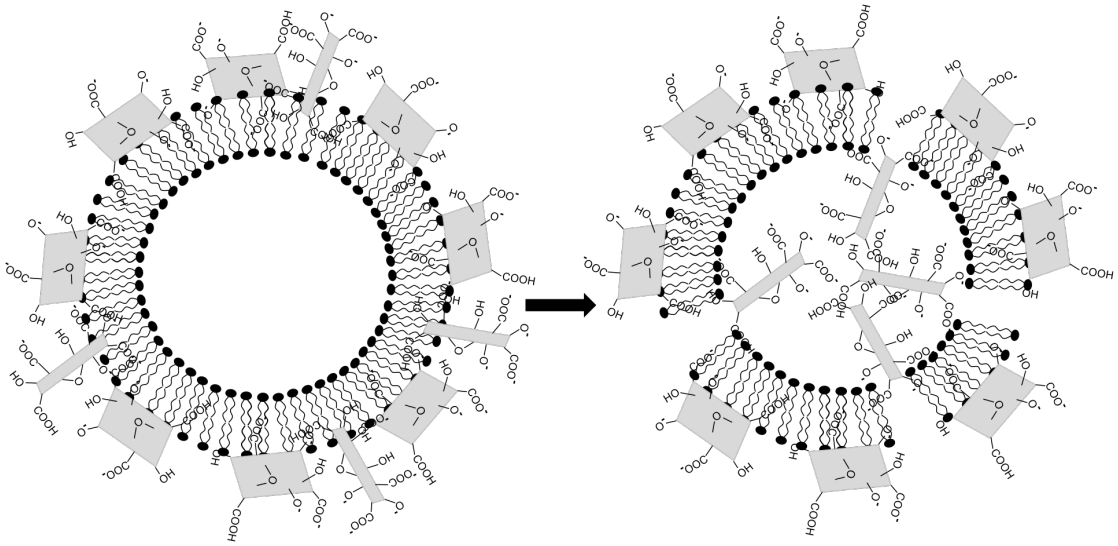

Figure 3.11 the proposed interaction of GO with giant vesicles. The expected initial interaction is shown at 0 min (left) and after 10 min (right). Due to the size of the GO, “edge on” GO is predicted to permeate the vesicle forming holes allowing GO to enter the vesicle. GO permeation of the vesicle occurs initially with very little change in permeation over the 1h time course.

As can be shown from images of vesicles treated with GO [Figure 3.8] it appears initial permeation is likely to occur before 10 minutes. However, due to the method used for this experiment, measurements could not be accurately recorded before 10 minutes. To overcome this, further experiments were carried out using self-quenching fluorescence vesicles, which allows fluorescence intensity measurements to be recorded using a fluorimeter. Although the self-quenching vesicles are smaller than the giant vesicles (~100 nm) and are not representative of the size of a cell, it is useful for investigating the GO-lipid interactions.

3.3.2 Permeability of Self – Quenching Vesicles

Initial experiments were carried out investigating the interactions of known pore-forming toxins with the vesicles. All experiments were performed in duplicate. The samples were incubated at 37ºC for 1h and the fluorescence response was measured. An incubation temperature of 37ºC was chosen to provide biologically relevant experimental conditions. Figure 3.12 shows the fluorescence response of α-haemolysin and NetB. Both positive (Triton X-100) and negative (HEPES buffer) controls were used in fluorescence normalisation. Normalised fluorescence was calculated using the equation,

$$(F_t - F_0)/(F_m - F_0) \tag{3.4}$$

where F_t is the average fluorescence value at a specific time point, F_0 is the minimum fluorescence and F_m is the maximum fluorescence shown in that particular experiment. The loss of fluorescein from the vesicles can be calculated as a percentage using the maximum release of dye with the addition of 0.01% Triton X-100.

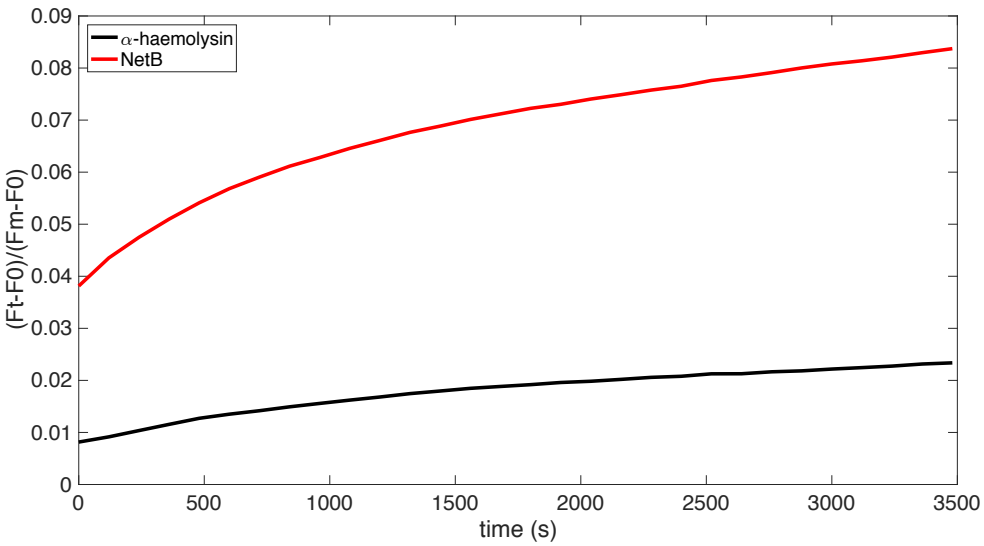

Figure 3.12 The average fluorescence response of the vesicles to two membrane-targeting toxins: α-haemolysin (black) and NetB (red), over 1h. Fluorescence values were measured and normalised.

NetB gave the greatest response with ~ 8% fluorescein leakage. This experiment was repeated over a range of NetB concentrations [Figure 3.13]. There is little fluorescence response at the lower concentrations of NetB, with only 0.45 mg/ml showing ~ 14% fluorescein leakage.

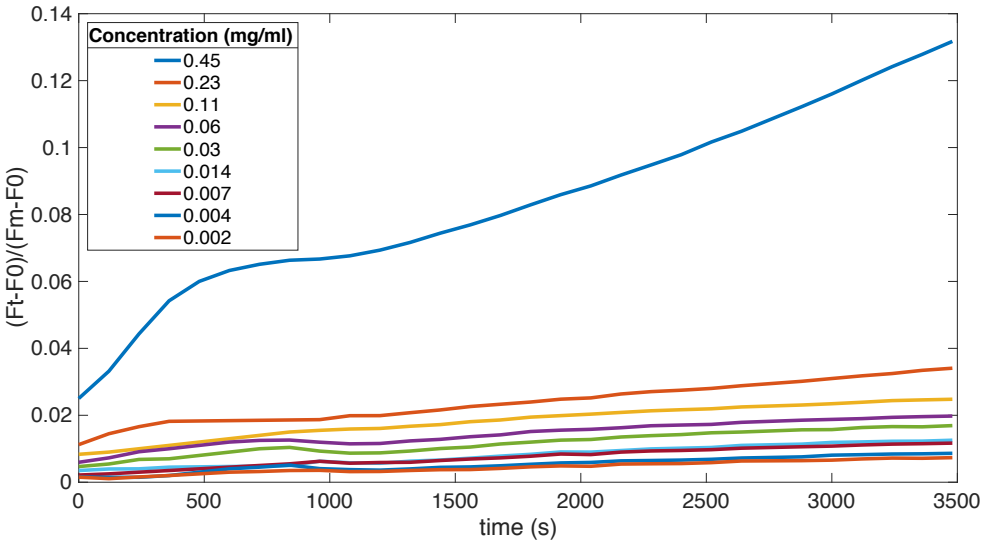

Figure 3.13 Fluorescence response of the vesicles to the toxin NetB, in the concentration range 2 x 10^{-3} mg/ml – 0.45 mg/ml. Fluorescence values were measured over 1h and the data was normalised.

Although there is not a strong fluorescence response from the NetB, it is useful to use as a comparison for graphene oxide experiments using similar concentrations. What is clear from these results is that as the concentration of NetB increases, the fluorescence response increases, with a significant increase at the higher concentrations [Figure 3.14].

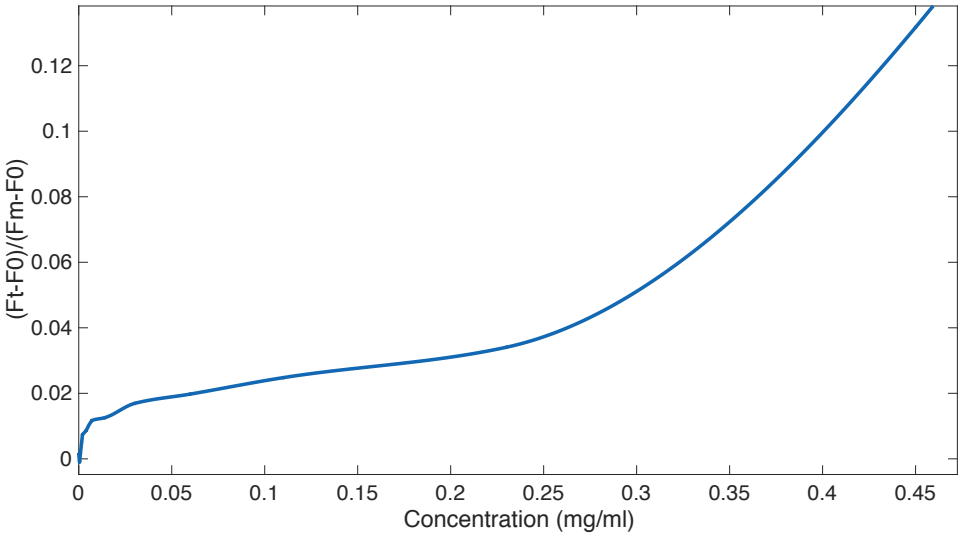

Figure 3.14 The fluorescence response as a function of NetB concentration over 1h.

Figure 3.15 shows the fluorescence response using a range of graphene oxide concentrations, in HEPES buffer, incubated for 1h at 37°C. This is also expressed as a function of graphene oxide concentration [Figure 3.16].

An increase in fluorescence is observed over time, with a significant increase at the higher concentrations of graphene oxide. For 0.1 mg/ml graphene oxide, there is a brief lag period of ~ 2 min, which probably reflects the time period required for graphene oxide to specifically adsorb to the membrane and to begin permeating the bilayer. This is followed by a sharp increase in fluorescence intensity over the next 20 min, which appears to plateau after ~ 30 min, suggesting no further fluorescein leakage from the vesicle and this steady state level is reduced as smaller concentrations of graphene oxide are used. 0.1 mg/ml graphene oxide causes ~ 35% fluorescein leakage which shows GO does not cause complete lysis of the vesicles, suggesting a specific mechanism of interaction. A plateau in fluorescence intensity is unlikely to be caused through all of the graphene diffusing into the vesicle. One possible suggestion is the GO interacts with only one component of the vesicle which then saturates. Another possibility could be that the vesicle bilayer ‘re-seals’ itself, blocking further fluorescein leakage. This has previously been reported (117), finding GO to permeate DOPC vesicles which successively led to reduced membrane tension, driving the pores to close (118) in a self-healing manner.

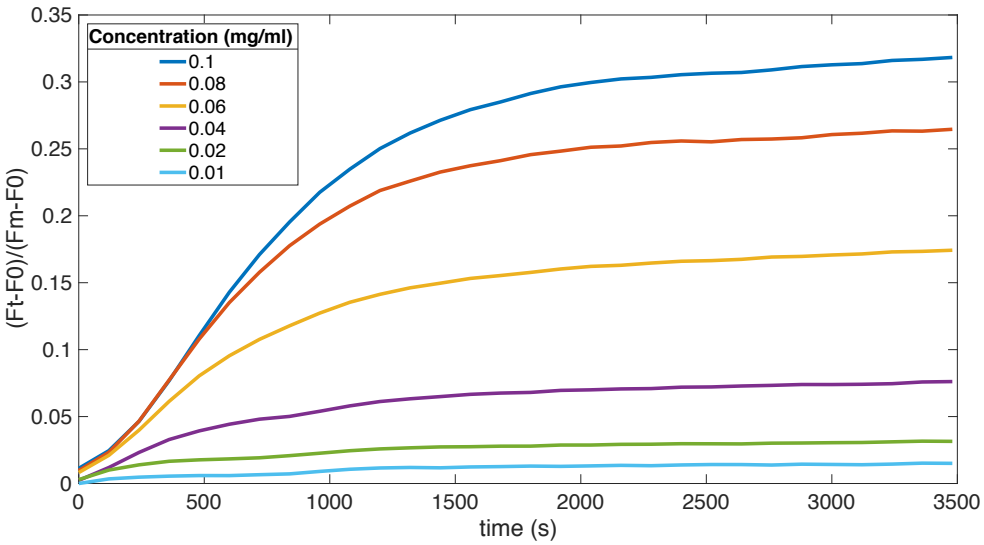

Figure 3.15 Fluorescence response of the vesicles to the graphene oxide, over the concentration range 0.01 - 0.1 mg/ml. Fluorescence values were measured over 1h and the data was normalised using the positive and negative controls.

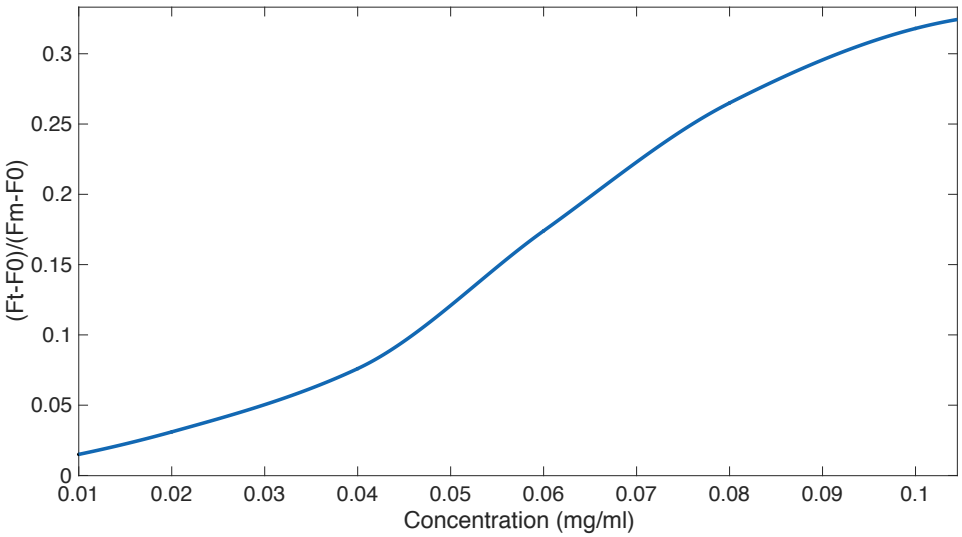

Figure 3.16 The fluorescence response as a function of graphene oxide concentration (t = 1h).

To determine vesicle permeability the same principle using equations 3.1 – 3.3 can be applied for this experiment, assuming I_{out} is the maximum fluorescence intensity observed, ΔI_1 is calculated from positive and negative controls, and ΔI_2 is calculated from vesicle treatment with graphene oxide at a specific time point. Figure 3.17 shows the average permeability coefficients (n=6) calculated for self-quenching vesicles treated with graphene oxide over a concentration range. As the graphene oxide concentration increases, the permeability increases. The permeability coefficient increases from 0.12 ± 0.005 x 10^{-6} cm s^{-1} to 1.65 ± 0.12 x 10^{-6} cm s^{-1}.

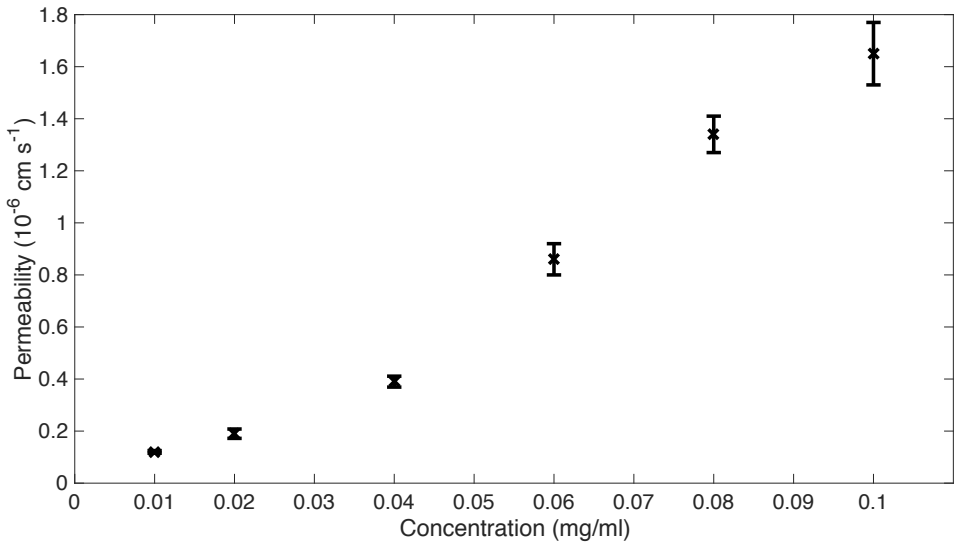

Figure 3.17 The average calculated permeability coefficients over 1 h for self-quenching fluorescence vesicles containing fluorescein, treated with graphene oxide suspended in HEPES buffer, over a concentration range from 0.01 – 0.1 mg/ml (n=6).

One observation that can be drawn on is the difference in permeability between the two preparations of vesicles. The highest permeability calculated for GUVs was 0.99 ± 0.05 x 10^{-3} cm s^{-1}, with a significant decrease to 1.65 ± 0.12 x 10^{-6} cm s^{-1} calculated at the highest concentration of GO used to treat self-quenching vesicles. From this it can be said DOPC vesicles are more permeable than the self-quenching vesicles. We hypothesise that the difference in membrane permeability is due the properties of the vesicles: their size and lipid composition. The average size of DOPC vesicles was ~ 8 μm, whereas the self-quenching vesicles are significantly smaller at ~ 0.1 μm. The self-quenching vesicles also

have a more complex lipid composition, including the TCDA linker molecule which decreases membrane fluidity. The DOPC vesicles are simpler in structure, but the fatty acid tails of the lipids are unsaturated, which could affect membrane fluidity **(119)**. Figure 3.18 shows the average permeability coefficients calculated for vesicles treated with 0.1 mg/ml GO and its control, over 1h.

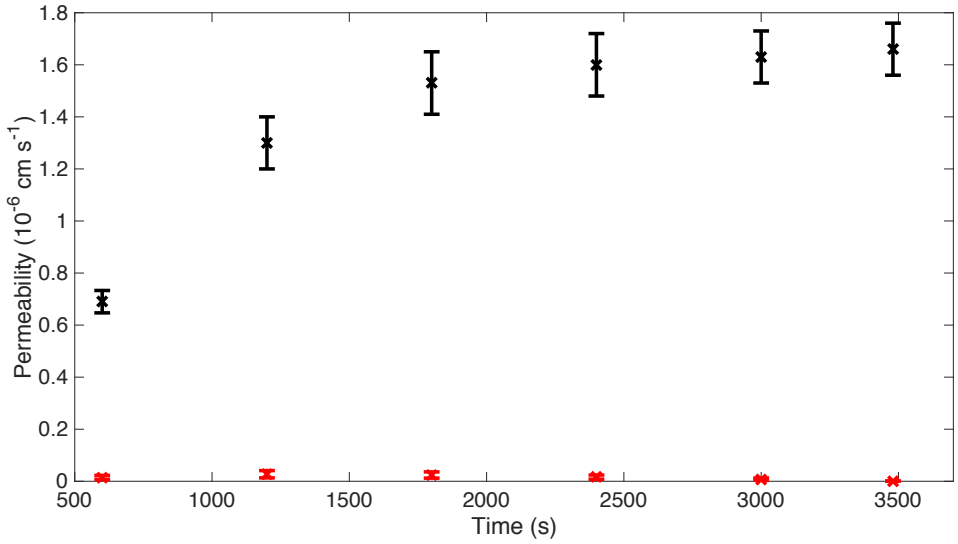

Figure 3.18 The average calculated permeability coefficients over 1h for self-quenching vesicles treated with 0.1 mg/ml GO (black) and vesicles treated with HEPES buffer (red).

There is a slow increase in permeability over the first ½ h from 0.7 x 10^{-6} cm s^{-1} to ~ 1.55 x 10^{-6} cm s^{-1}, where the curve plateaus. The addition of TCDA molecules and cholesterol decreases the permeability of the vesicle, which could decrease the rate of GO permeation. The plateau suggests that either, like the giant vesicles, the GO saturates the vesicle preventing further permeation. Or it is possible that the GO is interacting specifically with one of the phospholipids in the self-quenching vesicles, and therefore only permeating the vesicles in specific locations. From the results achieved using DOPC vesicles, which only have one lipid component, it can be suggested that GO permeates vesicles by interacting with the PC head groups of the lipids, forming holes within the bilayer. Figure 3.19 gives the proposed mechanism of interaction of GO with the vesicles.

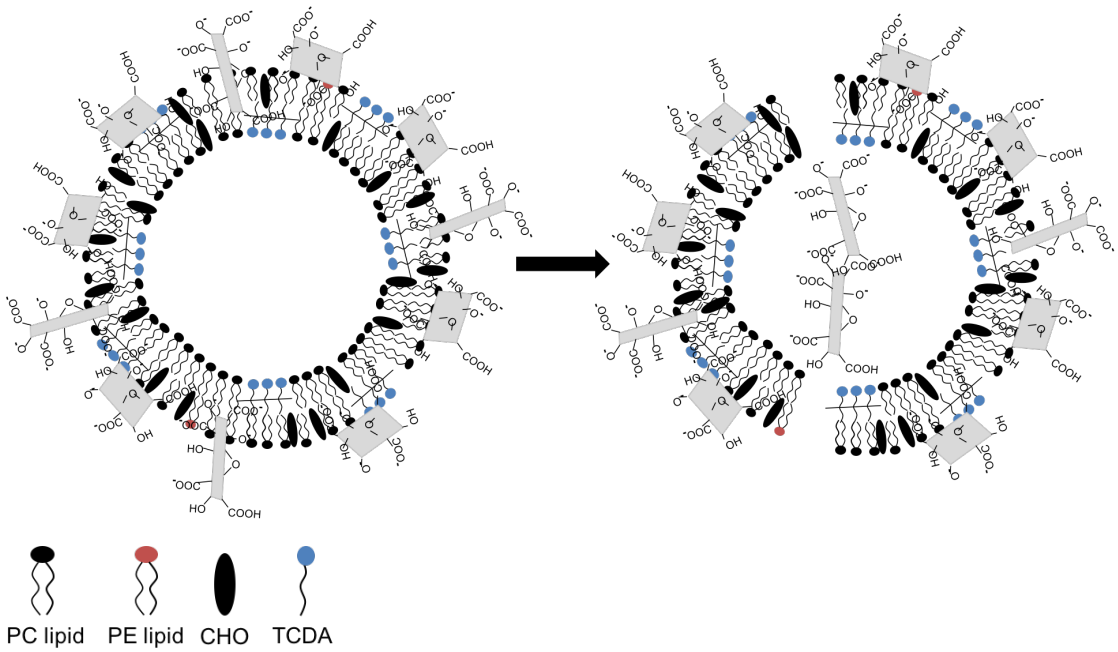

Figure 3.19 The proposed interactions of GO with self-quenching fluorescence vesicles. The addition of molecules which decrease permeability is likely to affect how much GO can permeate the membrane. It is possible GO is forming holes within PC regions of the vesicle.

By comparing the graphene oxide results with the results achieved using pore-forming toxins, it is clear graphene oxide creates greater permeability in the vesicles, shown by the greater fluorescence response. It is possible GO is also forming “pore-like” structures within the bilayer, similar to the toxins. The greater increase in fluorescence suggests GO either forms larger pores, compared to NetB, or similar sized pores with more attachment sites on the vesicle. Lipid vesicles have previously been used to determine NetB has an affinity towards cholesterol but not PC, interacting directly with cholesterol in the absence of other lipids (116). It is unclear from these results whether GO has any other interactions with the other lipid components of the vesicles. It could be possible that GO specifically interacts with PC head groups, with a greater fluorescence response observed with GO than NetB, with a greater concentration of DPPC and cholesterol present in the vesicle, 53mol\% and 20mol\% respectively. However, a low fluorescence response was observed with α-haemolysin, a toxin with a specific PC binding pocket (116). Further research investigating individual lipid-GO interactions would be required to determine the exact mechanism in which the GO is acting.

3.4 Conclusions

From experimentally determining the permeability of GO towards different compositions of vesicles, it can be concluded that GO permeates vesicles, rather than causing complete lysis of the vesicles. This was confirmed using two different experiments. Firstly, by analysing changes in the optical density of a series of images of giant DOPC vesicles treated with graphene oxide. The difference in contrast inside and outside the vesicle is caused by using two different solutions with containing sugars of different molecular weights but equal concentrations. The addition of graphene oxide showed an obvious change in contrast, suggesting the vesicle had been permeated causing an exchange of internal sucrose solution and the external glucose solution, resulting in a loss of contrast. The second experiment used self-quenching fluorescence vesicles to measure the permeability of graphene oxide, by measuring the change in fluorescence intensity over a period of time. Permeability is determined by the leakage of the fluorescein from the vesicle. Initially the fluorescence intensity is low, where the fluorescein inside the vesicle is quenched. As the vesicle is permeated and the fluorescein leaks out, the intensity increases. The results from this experiment showed an increase in fluorescence over time, as well as an increase at higher concentrations of graphene oxide. Therefore, there is an overall increase in permeability. From both experiments it is proposed that GO may permeate vesicles by interacting with PC lipids “edge-on”, forming holes in the bilayer, with “side-on” GO interacting with head groups saturating the outer lipid layer.

Chapter 4 The Effects of Graphene Oxide on Red Blood Cells

4.1 Introduction

In this chapter I will discuss experiments investigating the interactions of graphene oxide and red blood cells. Red blood cells (RBC) have a simple structure meaning we can look specifically at the interactions at the membrane, which is very similar to those of most mammalian cells. As the most abundant cell within the blood, it would be unavoidable to administer graphene-based materials into the blood without contact with RBCs. Any interactions will help determine the bioavailability of graphene and the kinetics of its distribution in tissues, relevant both to biomedical applications and safety. Determining how graphene oxide interacts with RBCs is therefore paramount in assessing its biological safety. The aim of this experiment is to determine if and how graphene oxide interacts with red blood cells. Analysing the fluctuations of the RBC membrane allows us to detect any changes in the mechanical properties of the cell membrane caused by graphene oxide. Absorbance measurements allow us establish whether graphene oxide changes the shape of the RBC, or produces haemoglobin leakages. We will also use Raman spectroscopy to determine whether graphene oxide is taken up by RBCs and where it accumulates in or on the cell.

4.1.1 Structure and Properties of Red Blood Cells

The red blood cell is the simplest of all biological cells, with no nucleus and no internal organelles. A mature cell is almost exclusively full of haemoglobin, the oxygen-binding protein, which allows for transport of oxygen throughout the body.

RBCs typically have a diameter of 5 – 8 μm with a biconcave disc shape. The biconcave disc allows for an increased surface area-to-volume ratio, improving oxygen transfer across the membrane, and also enables the cell to undergo deformations so they can pass through capillaries half the size of the cell. This biconcave shape is determined by the properties of the membrane. The structure of a mature red blood cell makes them an ideal candidate to use as a model membrane system, as well as being easily available. The red blood cell membrane mass consists of ~52% proteins, ~40% lipids and 8% carbohydrates. The membrane is approximately 20 nm thick and consists of a quasi-fluid lipid bilayer, with proteins embedded. The membrane proteins are anchored to a network of proteins on the cytosolic side of the membrane. This is known as the membrane cytoskeleton. The cytoskeleton is formed from various structural proteins; spectrin, ankyrin, protein 4.1, actin and several other proteins [Figure 4.1].

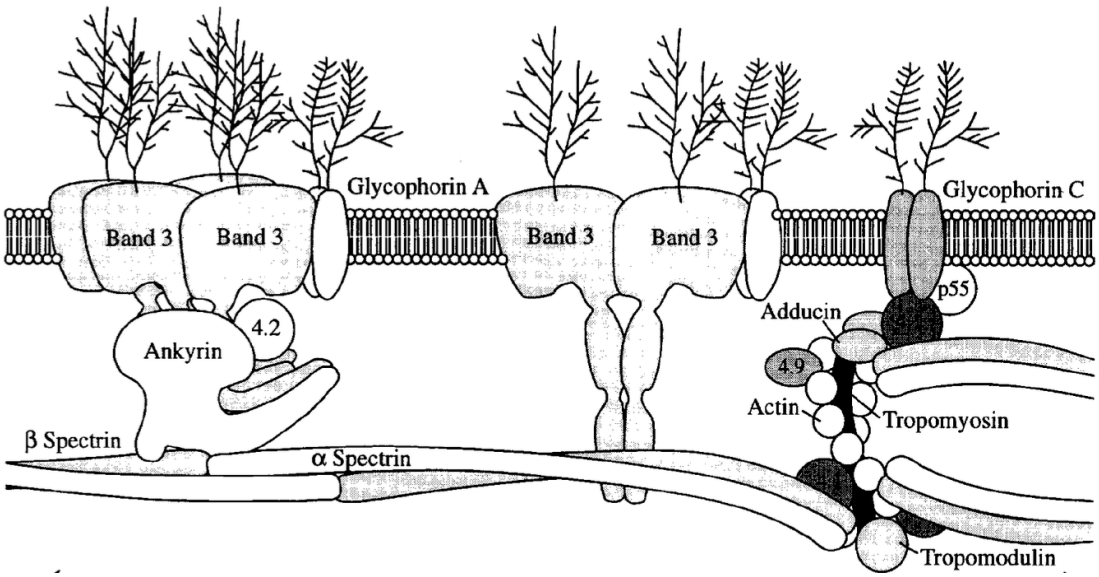

Figure 4.1 The structure of the RBC membrane (Tse and Lux, 1999). Showing the lipid bilayer with trans-membrane proteins embedded, and the primary structural protein spectrin that forms part of the cytoskeleton. From (120).

This network provides support to the membrane increasing the cells overall mechanical strength, in order to withstand regular deformations. The membrane is robust in order to withstand shear stresses.

Shape changes of RBCs are of great interest, particularly because they are lacking any internal organelles, and the biconcave shape of red blood cells being determined solely by the membrane mechanics., the shape transitions of the cell are due to changes in the cell membrane, either structure or composition of the lipid bilayer or underlying cytoskeleton. Shape transitions are often observed when the cell is in a pathological state, therefore the mechanical changes of the membrane is of great importance to understanding the structural significance of the pathological changes to the cell.

4.1.2 Membrane Elasticity

The primary role of the red blood cell is to transport oxygen from the lungs to the rest of the body. There are many diseases which show reduced performance of RBCs due to deformabilities such as sickle cell disease. Sickle cell disease results from a defect in the haemoglobin structure caused by substituting one amino acid causing a change in cell shape (crescent like). This change in shape can cause blocking of blood vessels resulting in an inefficient oxygen supply to surrounding tissues (121). As described in Chapter 1, the RBC is one of two typical systems used to demonstrate membrane elasticity. Studies have shown the lipid bilayer, membrane-associated proteins, as well as the cytoskeletal network contribute to the stability and deformability of the red blood cell (122). Research has largely been focused towards the most abundant cytoskeletal protein, spectrin. Several experimental techniques have been applied to characterise the deformations of RBCs including micropipette aspiration (123) and optical tweezers (124). These methods, however, only provide information about the membrane mechanics in static conditions.

RBC thermal fluctuations, ‘flickering’, provide comprehensive characterisation of membrane mechanics and have been studied extensively to better understand the relationship between the lipid bilayer and the cytoskeleton (125). RBCs flicker due to the Brownian motion of their thin membrane (126), resulting in fluctuations.

The RBC membrane can be described as a 2D surface, embedded in 3D space. The mean curvature of a membrane can be defined as,

$$H \equiv \frac{(1/R_1 + 1/R_2)}{2} \tag{4.1}$$

and the Gaussian curvature as,

$$K \equiv \frac{1}{(R_1 R_2)} \tag{4.2}$$

where the local curvature of the membrane, *C,* is *C = 1/R*, and *R* is the radius of the curvature characterised by two principal radii [Figure 4.2].

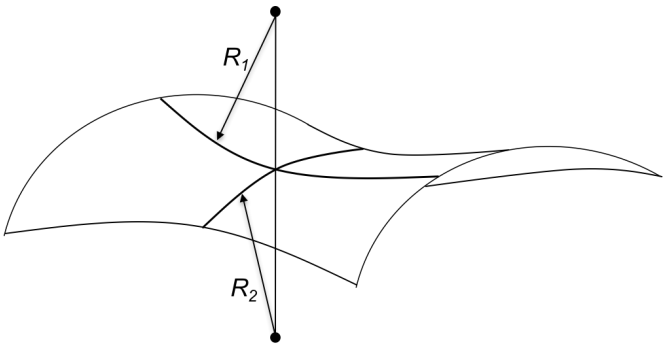

Figure 4.2 Radii of curvature R_1 and R_2, associated with one point of the surface.

The energy required to bend a bilayer increases with curvature. The simplest form for this energy density, f_0, is defined as,

$$f_0 \equiv \frac{k_b}{2}(2H)^2 + k_G K \tag{4.3}$$

where k_b is the bending modulus and k_G is the Gaussian bending modulus, derived from the classical curvature model for symmetrical membranes (127) (112). Giant vesicles, and many biological membranes, have a bending rigidity of

the order ~10 kT (128) (129), resulting in visible thermal fluctuations at room temperature. By analysing shape fluctuations, it is possible to determine the bending modulus.

An investigation into the mechanical properties of RBC membranes, treated with and without graphene oxide, will give an insight into how graphene interacts with cell membranes.

4.1.3 Thermal Fluctuation Spectroscopy

Thermal fluctuation spectroscopy is a recent technique designed to analyse giant non-spherical vesicles (130), developed from a simpler technique, which only analyses quasi-spherical vesicles. This technique has been further developed in order to analyse shape fluctuations of red blood cells (131). Phase-contrast microscopy is used to capture a time sequence of images of the fluctuating red blood cells. By using image analysis software, it is possible to obtain a 2-dimensional contour map of the membrane [Figure 4.3].

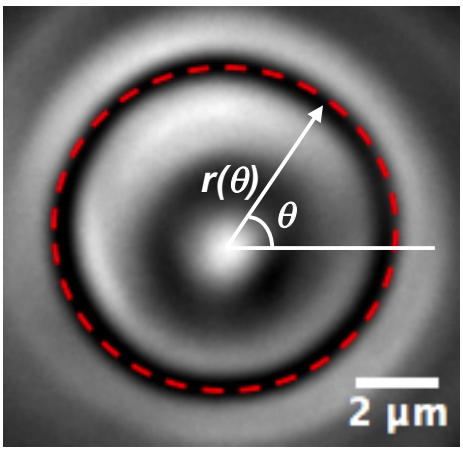

Figure 4.3 Phase contrast image of a red blood cell, showing a traced contour of the cell membrane. The polar coordinates *(r,θ)* are also shown.

The two-dimensional contours are fitted using a Fourier series, using polar coordinates (r,θ), with the origin at the centre of the area [Figure 4.3].

$$r(\theta,t) = r_0(t)\left[1 + \sum_n a_n(t)\,cos(n\theta) + \sum_n b_n(t) sin(n\theta)\right] \tag{4.4}$$

The time dependence of the resulting amplitudes, $a_n(t)$ and $b_n(t)$, encode all the necessary information about the shape fluctuations. a_n and b_n differ by $\pi/4$ rotation. The values extracted by fitting equation 4.4 to a set of experimental contours, describes the mean contour shape [Figure 4.4].

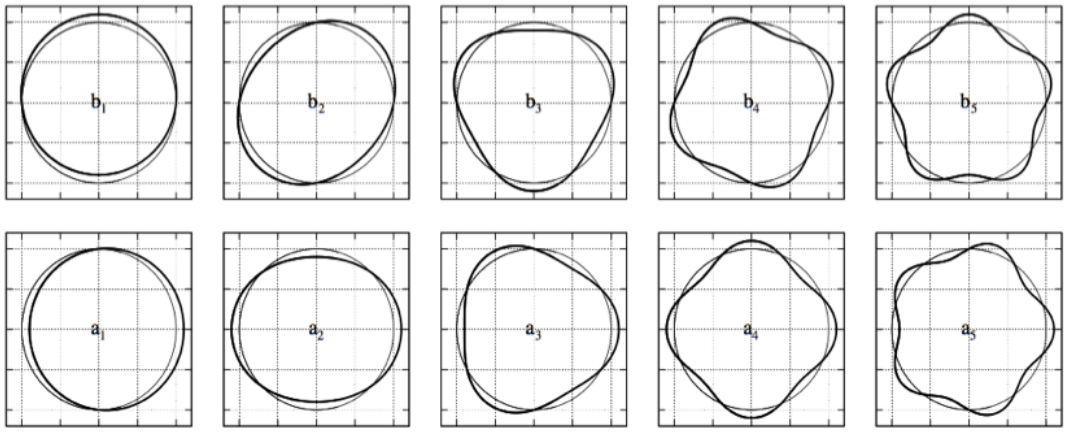

Figure 4.4 shape deformations corresponding to the first 5 Fourier modes of Equation 4.4.

The contour shape fluctuations around the mean shape are quantified using the mean square values of the amplitudes for each mode,

$$\langle \delta_n^2 \rangle = [\langle a_n^2 \rangle - \langle a_n \rangle^2] + [\langle b_n^2 \rangle - \langle b_n \rangle^2] \tag{4.5}$$

the same analysis used for fluctuation vesicles (132). A typical fluctuation spectrum for a normal red blood cell is shown in Figure 4.5. As the mode number, *n*, increases there is a significant drop in the mean square fluctuations, as expected.

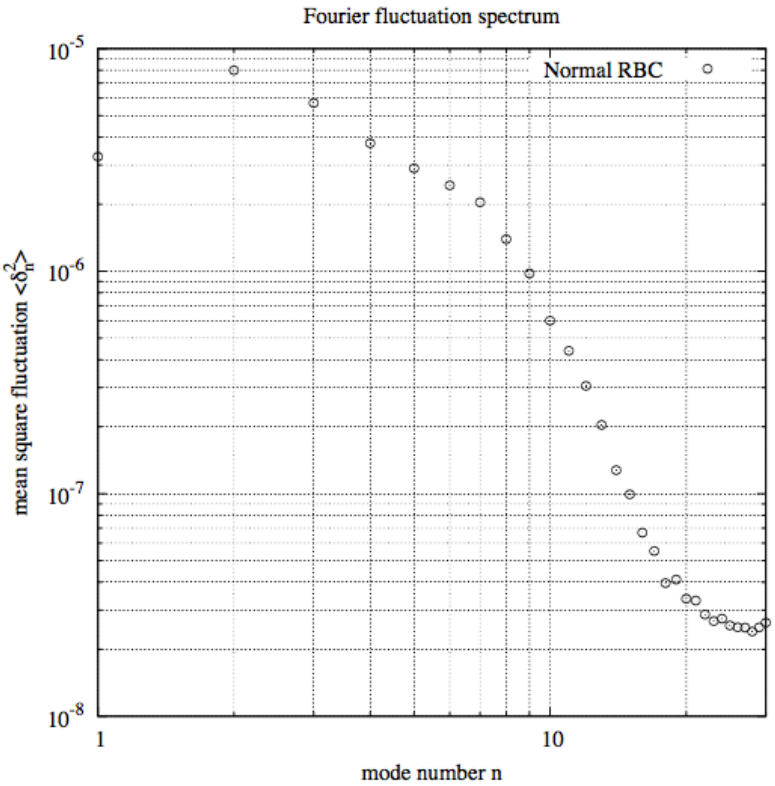

Figure 4.5 A typical fluctuation spectrum of a normal red blood cell, obtained from the Fourier analysis of the RBC contours. From (133).

The lower order modes encode the essential information regarding membrane elasticity. Modes up to $n \approx 18$ can be recorded reliably using this method.

The fluctuations of the amplitudes in the Fourier series enables extraction of the shear (μ) and bending (κ) elastic moduli, and the membrane tension (σ).

$$\langle C_n^2 \rangle = \frac{1}{2\pi} \frac{1}{\tilde{\kappa}\sqrt{\tilde{\sigma}^2 - \tilde{\gamma}}} \left[\left(\tilde{\sigma} + n^2 - \sqrt{\tilde{\sigma}^2 - \tilde{\gamma}} \right)^{-1/2} - \left(\tilde{\sigma} + n^2 + \sqrt{\tilde{\sigma}^2 - \tilde{\gamma}} \right)^{-1/2} \right] \tag{4.6}$$

where $\tilde{\kappa} \equiv \kappa/(k_b T)$, $\tilde{\sigma}$ is a dimensionless membrane tension. $\tilde{\gamma}$ and n are also dimensionless quantities. For lipid bilayers without a cytoskeleton, Equation 4.6 can be reduced to

$$\langle C_n^2 \rangle = \frac{1}{2\pi} \frac{1}{\tilde{\kappa}\tilde{\sigma}} \left[\frac{1}{n} - (2\tilde{\sigma} + n^2)^{-1/2} \right] \tag{4.7}$$

the equation for analysing contour fluctuations in vesicles (134). For red blood cells, equation 4.6 can be used to extract values for the bending modulus and the membrane surface tension, using non-linear regression analysis.

This method will be used to characterise the mechanical properties of the red blood cell membrane, and how graphene oxide affects these properties. However, there is one other important component of the red blood cell to consider: the oxygen-carrying protein, haemoglobin.

4.1.4 Haemoglobin Absorbance

Haemoglobin, the oxygen carrier of the red blood cell, consists of a haem group, containing iron, coordinated to four nitrogen molecules, forming a porphyrin ring. It facilitates oxygen transport by binding to oxygen molecules. Human RBCs contain high concentrations of haemoglobin (0.4 mg/ml). Spectroscopic techniques have been used to study interactions of molecules with electromagnetic radiation. UV-visible absorption spectroscopy has shown that haemoglobin exhibits strong absorption above 320 nm (135). The porphyrin ring exhibits strong absorption around 400 nm, known as the Soret region. This region is characteristic of porphyrin proteins. Different variants of haemoglobin, such as oxy- and ferri- haemoglobin, exhibit different maximum absorbance. According to the Beer-Lambert law, the specific absorption coefficients of an absorbing material can be defined by the equation

$$A = log_{10} \frac{I_0}{I} = \alpha\, cl \tag{4.8}$$

where I_0 is the intensity of incidence light, I is the intensity of transmitted light, l is the path length, c is the concentration of absorbing material and α is the absorption coefficient. With regards to red blood cells, the concentration here is that of haemoglobin and I_0 is the intensity of the light surrounding the cell. With red blood cells, it is possible to obtain an absorbance intensity profile, by plotting radial distance of the cell versus absorbance. This gives a profile, which traces

the shape of the cell, which in turn can be used to analyse changes in red blood cell shape. As a general rule, the higher the absorbance intensity, the more haemoglobin there is, and therefore the thickness of the cell would be bigger. Figure 4.6 shows an image of a human red blood cell using a 420 nm light. This technique can be used to determine the shape of the RBC (perpendicular to the light path) and, by integration, the total haemoglobin content of the cell.

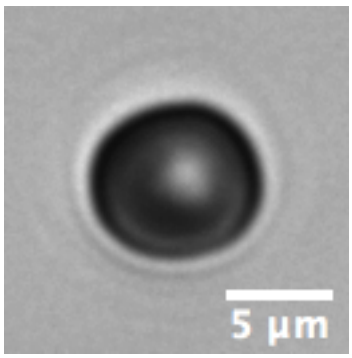

Figure 4.6 Image of a red blood cell viewed using bright-field microscopy, illuminated using a 420 nm light source.

4.1.5 Raman Spectroscopy of Red Blood Cells

To determine the location of graphene oxide within the red blood cell, Raman spectroscopy is used. Raman spectroscopy is a vibrational spectroscopy technique used for qualitative and quantitative analysis, by providing a unique chemical molecular fingerprint. It can be used to identify samples, and quantify the molecular components in the sample through their vibrational energy states. It does this by looking at particular molecule vibrations. Vibrational energy levels are different for every molecule. Light from a monochromatic light source (a laser) is shone on the sample. The majority of the scattered light remains unchanged, known as Raleigh scattering. A small amount of the scattered light shifts in energy from the laser frequency because of the interactions between the incident electromagnetic waves and the molecular vibrational energy levels in the sample. A Raman spectrum measures the intensity of shifted light versus frequency. Band positions within the spectrum are at frequencies corresponding to energy levels

of different functional group vibrations. The band areas are proportional to the concentration of molecules in the sample. The Raman spectrum of graphene is commonly used as a method of characterising graphene and its derivatives, and the spectra are well known (136). A Raman spectrum of graphene oxide [Figure 4.7] shows its main characteristic peaks at ~ 1580 cm^{-1} (the 'G peak') and at ~ 1350 cm^{-1} (the 'D peak').

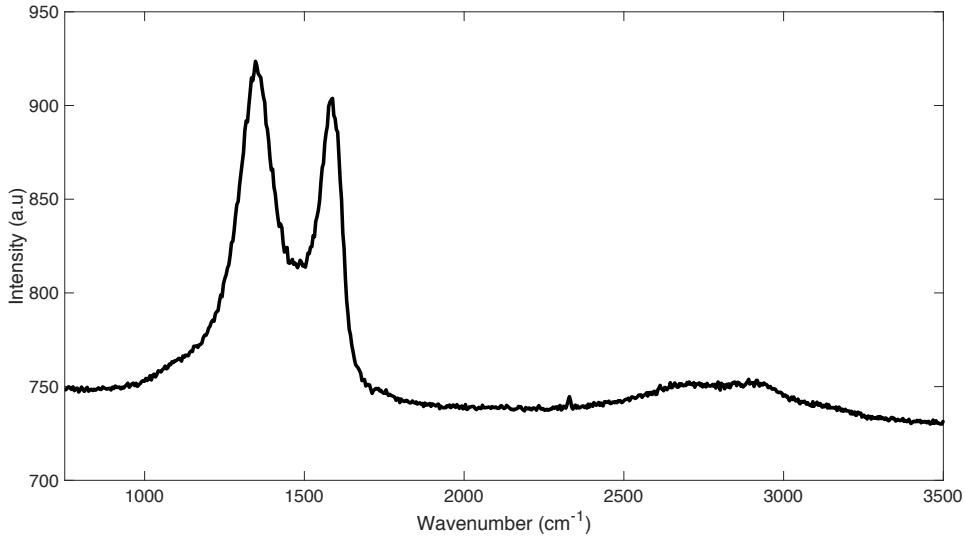

Figure 4.7 Raman spectra of graphene oxide, showing the G peak at 1580 cm^{-1} and the D peak at 1350 cm^{-1}.

Raman spectroscopy has also been widely used to study the molecular composition of single cells, including red blood cells. Both oxygenated and deoxygenated cells have been studied using Raman (137). Figure 4.8 gives an example of the Raman spectrum of an oxygenated RBC recorded using an excitation wavelength of 532 nm. There are several spectral regions reported, 1200 – 1250 cm^{-1}, 1355 – 1376 cm^{-1} and 1500 – 1650 cm^{-1}, to be characteristic of an oxygenated RBC (138) (137).

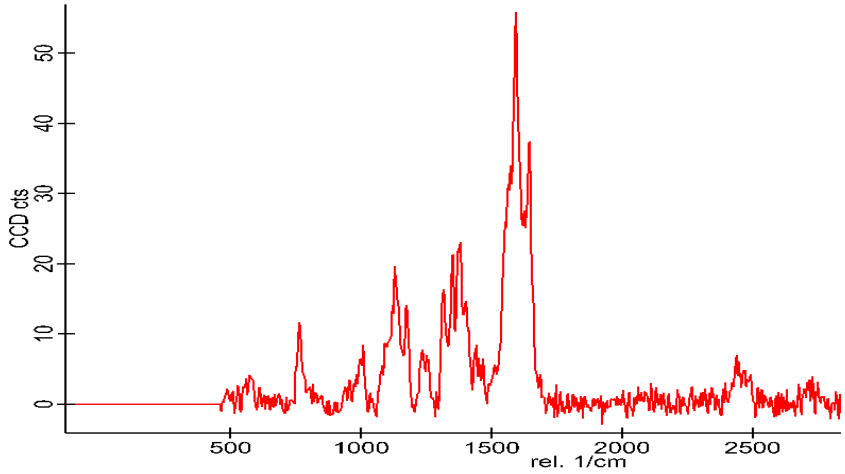

Figure 4.8 Raman spectrum of an oxygenated RBC recorded at 532 nm excitation wavelength

4.1.6 Previous Work

There have been initial studies researching interactions of GO and RBCs. Liao K-H *et al.* investigated the haemolytic activity of GO in human erythrocytes by measuring the haemoglobin present in the RBC suspension (60). Several graphene oxide suspensions (0.05 mg/ml) were used in this experiment, varying the sonication intensity and time to produce different sized flakes. They concluded smaller GO flakes, produced by probe sonication for 30 min, showed a higher haemolytic activity, compared to bigger flakes produced by shorter probe sonication and longer bath sonication. This suggested that membrane disruption is due to electrostatic attractions between the negatively charged graphene oxide, and positively charged PC lipids present on the outer membrane of the red blood cell.

In contrast, Zhang X. *et al.* reported good biocompatibility of graphene oxide with red blood cells (139). At GO concentrations of 10 μg/ml GO flakes adhered to the surface of the cells, but had little effect on morphology or membrane integrity. However, at higher concentrations, 80 μg/ml, ghost cells were observed. Ghost cells are RBCs which are visibly intact but have lost their

haemoglobin content, suggesting damage to the cell membrane causing the contents of the cell to leak out.

The GO preparations used in the following experiments differ from those previously used. A higher concentration of GO (1 mg/ml) is used throughout, using centrifugation to remove any aggregated GO and to produce a preparation with a uniform flake size distribution of ~ 500 nm.

4.2 Experimental Methods

4.2.1 Preparation of Graphene Oxide Suspension

In the following experiments, 1 mg/ml graphene oxide solutions, in phosphate buffer solution (PBS) with 1% bovine serum albumin (BSA, Sigma-Aldrich, UK), were used. The graphene oxide was sonicated in the PBS buffer for 1h, and centrifuged at 10,000 rpm for 10 min. The supernatant was collected, and the pellet discarded.

4.2.2 Microscope Chamber Preparation

The RBC chamber was constructed using standard glass microscope slides (75 mm x 25 mm x 1 mm), Parafilm and a thin glass cover slip (22 mm x 22 mm). All microscope slides and glass cover slips were cleaned using ethanol. Thin strips of Parafilm were used to create the chamber, by acting as a spacer between the slide and the coverslip. The Parafilm was placed on opposite sides of the microscope slide to form an open-sided chamber. The chamber was bonded together by applying heat from a hot plate in order to secure the slide and coverslip to the Parafilm. This formed a chamber ~ 1 mm in depth [Figure 4.9].

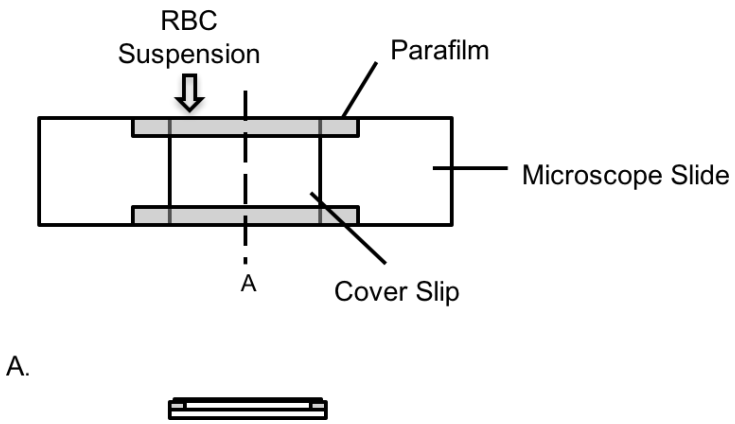

Figure 4.9 RBC open-sided chamber, prepared using a glass microscope slide and cover slip, separated by a single layer of Parafilm, sealed by applying heat. The RBC solution is introduced to the chamber by pipetting underneath the cover slip. The graphene oxide solution is added via buffer exchange through the chamber.

The open-sided chamber was used to allow for buffer exchange during the experiments. Excess solution was dropped onto the microscope slide at one end of the chamber, allowing the buffer to be pulled through the chamber with the aid of filter paper placed on the opposite side.

4.2.3 Blood Sample Preparation

A PBS buffer was used throughout these experiments, with a pH of 7.4 to which was added 1 mg/ml BSA (Sigma-Aldrich, UK). BSA was used to maintain the shape of the red blood cells, once the cells had been added to the chamber. It counteracts what is known as the “glass effect” which causes cells to change shape once in contact with the microscope slide (140). Fresh human blood samples were collected using a pin-prick lancet (Accu-Chek, Softclix Plus, Roche Ltd) immediately before each experiment and suspended in 1 ml of PBS 1% BSA buffer. Approximately 2 – 5 µl of blood was used. 20 µl of the suspended cells were placed in the microscope chamber using a Gilson pipette. By holding the pipette tip downwards onto the microscope slide, next to the glass cover slip, the cells could be injected into the chamber. The cells were then left for 5 – 10 min to settle. The difference in density between the red blood cell and the buffer, allows the red blood cells to stabilise at the bottom of the chamber, allowing

membrane fluctuations to be observed. 200 µl of graphene oxide was added to the chamber via buffer exchange. During buffer exchange it was found to be important to keep a slow, constant supply of the solution to the chamber, to avoid drying out.

4.2.4 Fluctuation Spectroscopy

A fast-video phase-contrast microscope (Leica DMLFS) was used to view fluctuating red blood cells, using a 530 nm light source (Thorlabs, Mounted High-Power LED M530L2), which allowed membrane flickering to be observed. The microscope was equipped with a 63X PL Fluotar phase-contrast objective. Video sequences of the fluctuating red blood cells were taken using a Q-Imaging camera at a typical frame rate of 7 fps. Initial experiments were carried out to determine the time course required for the following experiments. After first taking acquisitions every 5 min for 1h, it was determined that during the first 5 minutes there were significant changes to the RBC radius. From this it was decided that acquisitions would be taken over a period of 1/2h, taking one reading after 1 min, then increasing to 5 min, then 10 min, until 30 min. Once a series of contours (~1500) was acquired, they were then analysed to quantify the membrane fluctuations.

The fluctuation microscopy was repeated with GO/RBC suspensions over a longer time course, and at different temperatures. ~ 2 – 5 µl of blood was added to 500 µl of graphene oxide solution and incubated over a range of time periods (1/2h, 1h, 2h) and a range of temperatures (4°C, room temperature, 37°C). All cells were washed using PBS to remove excess graphene oxide before fluctuation measurements.

4.2.5 Absorbance Measurements

For absorbance experiments, videos of cells were taken using bright-field microscopy, using a 420 nm light source (Thorlabs Mounted High-Power LED

M420L2). 20 μl of RBC/PBS solution was added to the microscope chamber, and the video was taken. For graphene oxide measurements, 20 μl of RBC was added to 200 μl of the graphene oxide suspension, and left for ½ h at room temperature. Videos were then taken of the graphene oxide treated cells, in the same way as before. ImageJ analysis was used to calculate the absorbance at different points across the cell. The average absorbance intensity was recorded and a curve fitting tool (MATLAB) was used to reconstruct the cell profile and calculated the integrated area of the curves.

4.2.6 Raman Spectroscopy

4.2.6.1 Slide Preparation

In order to hold the red blood cells in place on the microscope slide, the slides were first coated in poly-L-lysine. The poly-L-lysine was diluted in deionised water (1:10) prior to slide coating. Slides were first cleaned with ethanol. The clean slides were placed into a slide rack, then into the poly-L-lysine solution for 5 min. The slides were then drained and dried at room temperature overnight. When dry, nail varnish was used to create a chamber on the slide, in order to avoid the cells drying out. 20 μl of RBC/graphene oxide solution was then dropped onto the slide, and a cover slip was placed over the top. The cells were then left for 15 min to allow sufficient time to adhere to the slide.

4.2.6.2 Raman Measurements

Raman spectra of RBCs were acquired using WITec Alpha300 R Raman imaging system. A 532 nm laser was used with a 50X objective. The laser power on the sample was 2.3 mW. Raman spectra were collected from 0 cm^{-1} to 3600 cm^{-1} with an integration time of 0.1 s. Raman maps were constructed using WITec Project 4.1 software with Shape plus graph background subtraction.

4.3 Results and Discussion

This section includes all results from the fluctuation spectroscopy of red blood cells, with and without exposure to graphene oxide, including calculations of the bending modulus. It also includes the effects of graphene oxide exposure over longer time periods, at room temperature and 37°C. Results showing absorbance plots of the cross-section of the RBC will also be described. Finally, the results from the Raman spectroscopy study locating graphene oxide within the cell will be discussed.

4.3.1 Fluctuation Spectra and Calculating the Bending Moduli

A typical phase contrast image of a red blood cell is shown in figure 4.2. The time sequence of contours, obtained from monitoring the cell membrane fluctuations, were fitted to the Fourier series [Section 4.2.3] giving a typical fluctuation spectrum shown in Figure 4.3. This analysis was repeated for cells treated with 1mg/ml graphene oxide, as well as cells treated with PBS buffer as a control. Figure 4.10 shows an example of the fluctuation spectra observed for cells treated with graphene oxide over a time course of ½ h. An overall decrease in the mean square fluctuation is observed after treatment with GO, showing the greatest affect after the first minute. For all spectra obtained, graphene oxide suppresses fluctuations in the lower modes, indicating an increase in bending rigidity. GO also has a small effect on the higher modes. From these results it is concluded that graphene oxide causes rigidification of the lipid bilayer with respect to its bending modulus.

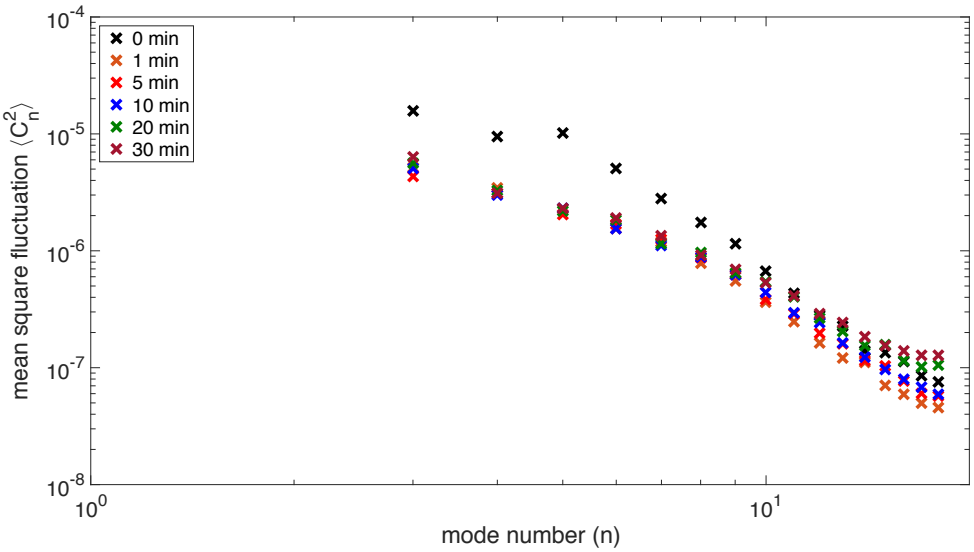

Figure 4.10 Contour fluctuation spectra of a red blood cell before treatment (t=0) with graphene oxide (black) and treated with 1 mg/ml GO over 1/2 h, showing increasing bending rigidity (top to bottom).

Following the recording of the Fourier fluctuation modes, the results are then fitted to the equation 4.6 in order to determine the values for the bending modulus, κ. Equation 4.6 provides meaningful fits for modes 3 - 18. An example fit is given in Figure 4.11. From these fits, values for κ were extracted.

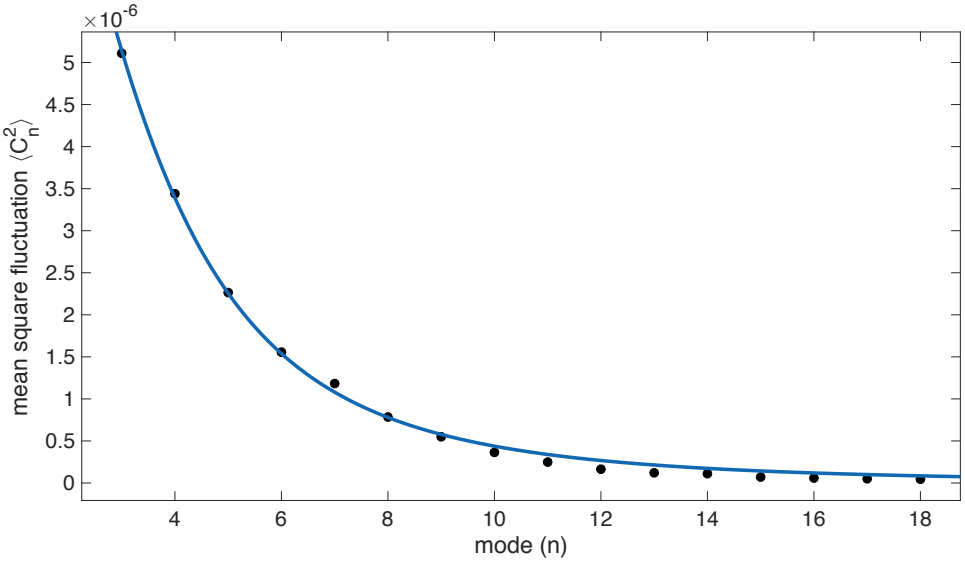

Figure 4.11 A fit of equation 4.6 to a contour fluctuation spectrum for a normal RBC at 0 min. Modes 3 – 18 are fitted, and values for the bending modulus are extracted.

Figure 4.12 shows the average normalised values of κ extracted from red blood cells treated with graphene oxide over 30 min, with respective errors (n=10). Normalisation was achieved using κ/κ_0, where κ_0 is the bending modulus at t=0. At 0 min, before treatment, the normalised bending modulus is 1.00 ± 0.32. At 30 min, the normalised bending modulus is 1.76 ± 0.47.

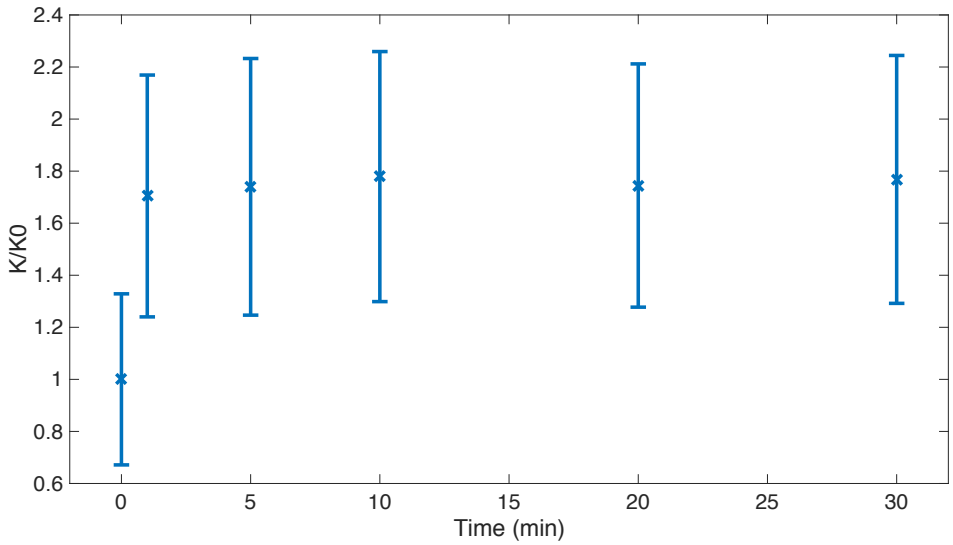

Figure 4.12 The normalised data, calculating the bending moduli from the fluctuation spectra of 10 red blood cells, treated with graphene oxide over ½ h. (1.75 ± 0.03, n=10)

There is an approximate two-fold increase of the membrane bending modulus observed when red blood cells are treated with graphene oxide. In control experiments no change to the bending modulus was observed [Figure 4.13]. The average bending modulus for untreated cells was calculated to be 4.59 x 10^{-19} J, which corresponds well to previously recorded values ranging from 1.4 x 10^{-19} J to 4.3 x 10^{-19} J (141) and from 2 x 10^{-19} J to 7 x 10^{-19} J (142). The initial average normalised bending modulus is 1.00 ± 0.17, and the final value calculated after ½ h is 1.02 ± 0.23 (n=10).

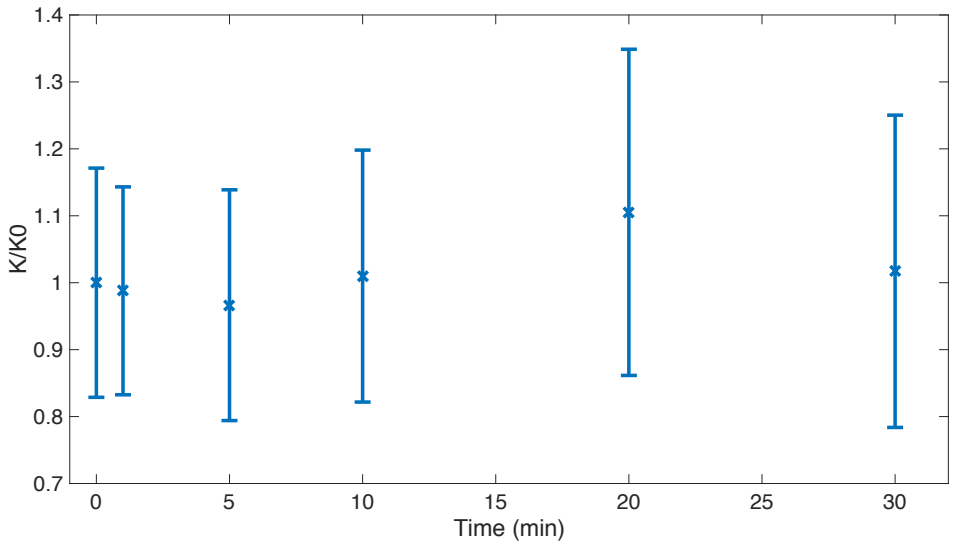

Figure 4.13 The normalised data, calculating the bending moduli from the fluctuation spectra of 10 red blood cells, treated with PBS buffer (1% BSA). (1.01 ± 0.04, n=10).

Figure 4.12 shows the greatest effect of the graphene oxide occurs within the first ½ hour. To investigate behaviour at longer times, cells were incubated with graphene oxide and were measured at ½ h, 1 h and 2h [Figure 4.14]. The average bending moduli were 1.87 ± 0.35, 1.95 ± 0.37 and 1.81 ± 0.28, respectively (n=5).

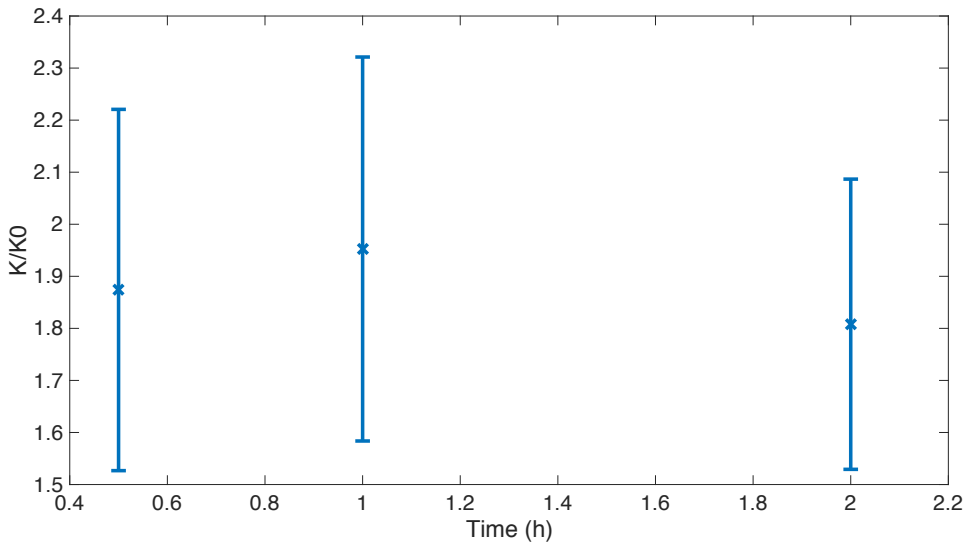

Figure 4.14 The normalised bending modulus calculated for RBCs incubated with graphene oxide at room temperature. Fluctuation measurements were taken at 1/2h, 1h and 2h.

The bending modulus doubled, as in the shorter time experiments, indicating that the increase in membrane rigidity occurs immediately after contact of the cells with the GO solution and as there is no significant change to the mechanical properties after the initial interaction it is likely the graphene oxide does not pass through the membrane. There is also no observable toxic effect on the cells as the RBCs remain intact, at least as observed by phase contrast imaging.

The effect of temperature was also investigated. Incubating the red blood cells with graphene oxide at 4°C, room temperature and 37°C (body temperature) all resulted in an increase in bending modulus. Figure 4.15 shows the average values obtained over ½ hour incubation periods (n=5), giving average values of 1.64 ± 0.33, 1.87 ± 0.35 and 1.69 ± 0.33, respectively.

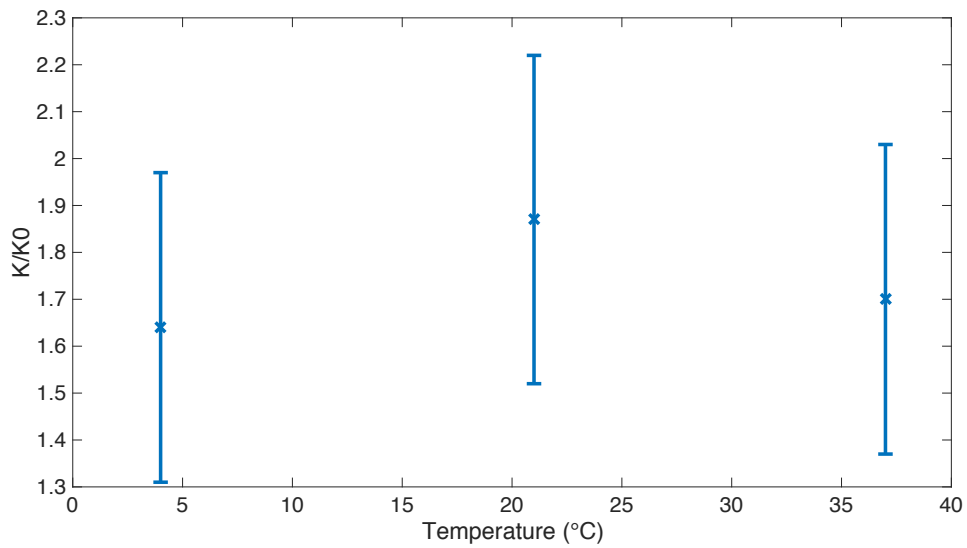

Figure 4.15 The normalised bending modulus of the red blood cell membrane, treated with graphene oxide for ½ h, at different temperatures.

These results show that the interaction of graphene oxide and red blood cells is not temperature dependent.

The effect of the graphene oxide on the mechanical properties of the RBC membrane is likely to arise from reorganisation of the lipid bilayer. The Langmuir monolayer measurements [Chapter 2] suggested that the GO interacts with the outer leaflet of the RBC membrane, with repulsive forces between PS head groups of the inner leaflet and GO preventing further incorporation of GO.

An increase in bending modulus of the red blood cell membrane also occurs in cells exposed to oxidative stress (131) and this may also occur after GO exposure since it has been reported to induce oxidative stress in *P. aeruginosa* cells (143) through the production of superoxide radicals and also in A549 cells, inducing slight loss of cell viability (59). However, there are significant differences between the cell types so GO may interact differently.

4.3.2 Absorbance Analysis

Initially, absorbance measurements were carried out using the same method as the fluctuation experiments, via buffer exchange of the graphene oxide. However, red blood cell membranes tend to stiffen after long exposures to the 420 nm light, meaning the light had to be turned off between acquisitions. Without a continuous light source cells dropped out of sight, limiting the number of measurements taken on cells treated with graphene oxide. To overcome this, the method was altered. Measurement of red blood cells, without graphene oxide treatment were first taken, changing cell sample for each measurement to avoid long exposures to the light. Red blood cells were then added to the graphene oxide suspension before being added to the microscope chamber. They were left for ½ h, added to the microscope chamber, then the videos were taken over a representative number of cells. The absorbance was then calculated at different points across the cell to reconstruct the shape profile of the RBC (using ImageJ and MATLAB). Figure 4.16 shows the average absorbance intensity (n=5) for normal red blood cells and red blood cells treated with graphene oxide. A decrease in the radius is observed but little change in absorbance.

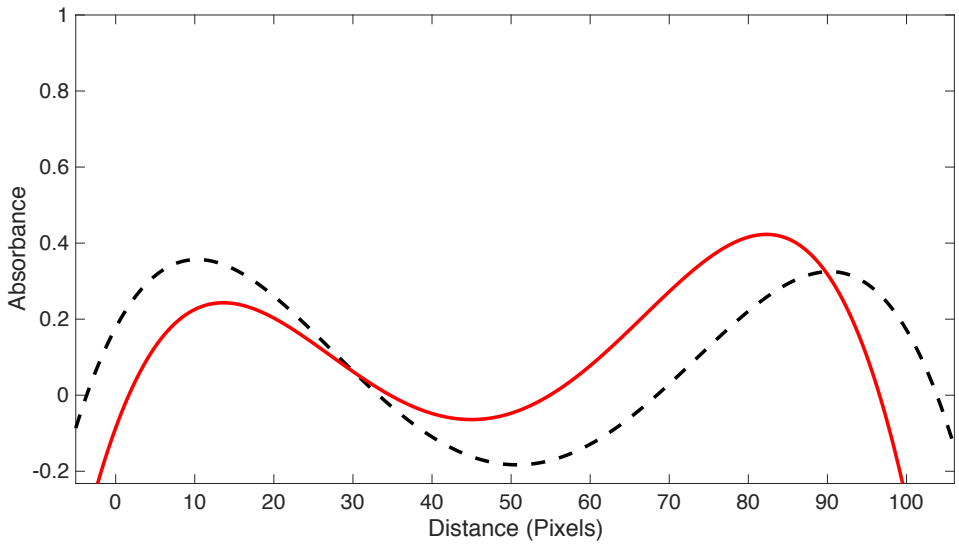

Figure 4.16 Averaged radial absorption of a red blood cell, before (black) and after treatment with 1 mg/ml graphene oxide (red) (14 pixels = 1 µm).

The RBC profiles suggest GO alters the shape of the red blood cell but does not cause any haemoglobin leakage, because the integrated areas of the curve are the same. This suggests GO does not penetrate through the whole membrane. A decrease in absorbance would be observed if there was a loss of haemoglobin from inside the cell. This contradicts some of the literature **(60)**, where loss of haemoglobin was reported due to GO damaging the RBC membrane. However, this study measured large populations of RBCs. In this thesis, only single cell measurements were conducted.

The RBC profiles show a decrease in radius of cells treated with GO. This observation is consistent with radial measurements acquired during the fluctuation spectroscopy experiments previously discussed. The radius was measured for all cells before addition of the graphene oxide, and at selected time points after graphene treatment over ½ h. This was repeated for all control cells. Figure 4.17 shows the normalised average radius (n=10) as a function of time, with a small decrease in radius observed for red blood cells treated with graphene oxide.

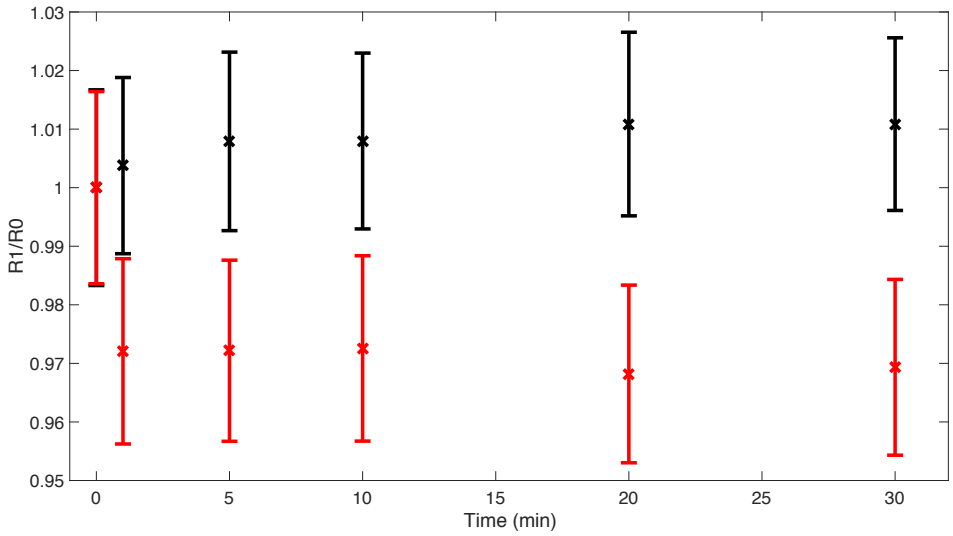

Figure 4.17 Normalised average radius of red blood cells treated with graphene oxide (red) and without (black), over 1/2 h.

A decrease in R_1/R_0 suggests a loss in membrane surface area, which can indicate loss of lipids from the membrane. This provides further evidence that graphene interacts with the lipids of the membrane, or alters the structure of the membrane.

From the fluctuation and absorbance analysis, we suggest that graphene oxide adsorbs onto the red blood cell membrane but does not enter the cell. There are several factors that could drive the adhesion of graphene oxide to the cell membrane. Graphene oxide and the cell membrane have similar flexibility which could facilitate the two being held together. Theoretical studies have shown the bending rigidity of graphene to be similar to the lipid bilayers of cells (144). The association of graphene oxide on the membrane could induce interactive forces, including electrostatic and hydrophobic interactions, in order to hold the two together.

Graphene oxide has previously been found to interact specifically with aquaporin proteins within the cell membrane (145), a protein in high abundance in the RBC membrane (146). The authors found GO to enhance membrane permeability without penetrating the cell in the breast cancer cell line MCF-7, but caused haemolysis in red blood cells (145). Haemolysis has not been observed in our work, but it is possible the graphene oxide is interacting with the aquaporin proteins. Aquaporin is important in RBCs in determining cell water transport to

regulate cell volume. A change in cell volume was not found in our work, so it seems unlikely that the activity of this channel is affected.

4.3.3 Raman Spectroscopy

To date, there has been no spectroscopic study investigating the interactions of GO with RBCs. The main aim of the present work was to use Raman mapping of the graphene peaks to investigate the distribution of graphene in or on the cells. Obtaining Raman spectra for RBCs proved challenging. One issue was finding a cell with GO associated to it, due to a large sample size of cells measured without detection of GO (this was not a problem for previous experiments because the RBC was found first then treated with GO). Another problem was finding an intact RBC. In Figure 4.18 abnormal RBCs can be observed with a serrated membrane. These cells are known as echinocytes and can be a result of the 'glass-effect' which causes morphological changes to RBCs (140). Although, this was not a problem with previous experiments, suggesting the RBCs were more sensitive to the laser.

A typical Raman spectrum of graphene oxide is shown in Figure 4.7, with its two characteristic peaks (G-peak: 1580 cm^{-1} and the D-peak: 1350 cm^{-1}). Figure 4.8 shows the Raman spectrum of an oxygenated RBC which shows characteristic peaks in the same regions as GO. Raman images at selected peaks were taken in order to investigate the position of graphene oxide within the cell. The peaks chosen to investigate were 1350 cm^{-1} and 1580 cm^{-1} (the GO peaks) and 2940 cm^{-1} (the C–H band). Figure 4.18 shows a snapshot of the cell analysed in this example.

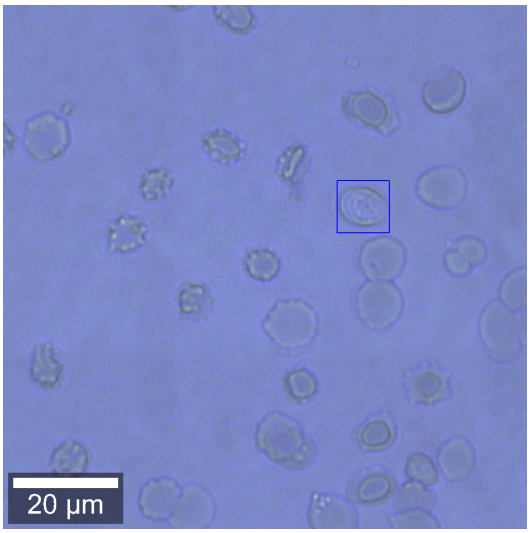

Figure 4.18 A snapshot of the red blood cell chosen for Raman analysis: most of the other cell were becoming echinocytic. The sample was incubated with 1 mg/ml graphene oxide for 1h at room temperature.

Figure 4.19 shows the recorded single spectra of RBCs treated with GO at bands 1350 cm^{-1}, 1580 cm^{-1} and 2940 cm^{-1}. Spectra a) and b) were taken at 1350 cm^{-1} and 1580 cm^{-1}, respectively. The results show clear peaks at both wave numbers, characteristic of graphene oxide. However, when compared to the spectra obtained for the control RBC [Figure 4.8] peaks were observed in the same positions resulting in some ambiguity to which component was producing the Raman signal. This limited the information that could be gained from using Raman analysis. There appears to be a GO flake in the Raman image scans produced in a) and b) shown by a cluster of high intensity [Figure 4.19]. These clusters were also observed in all the RBCs successfully analysed (n=4). However, the spatial resolution was inadequate to confirm whether the GO is inside or outside the cell. In future experiments, depth scans of the sample could provide further information on whether the GO is inside the cell, but these would take a very long time and the cell might not survive. The Raman image scan obtained for control cells [Figure 4.8] shows the 2940 cm^{-1} C–H band, representing C–H vibrations, is concentrated towards the middle of the cell. This is possibly from the heating effects of the laser causing the cell to shrink, therefore concentrating the C–H material. For future Raman analysis, new imaging modalities might be required, for example restricting the imaging to specific

peaks, that require less laser power to analyse the cell. This could minimise cell damage without losing spectral details.

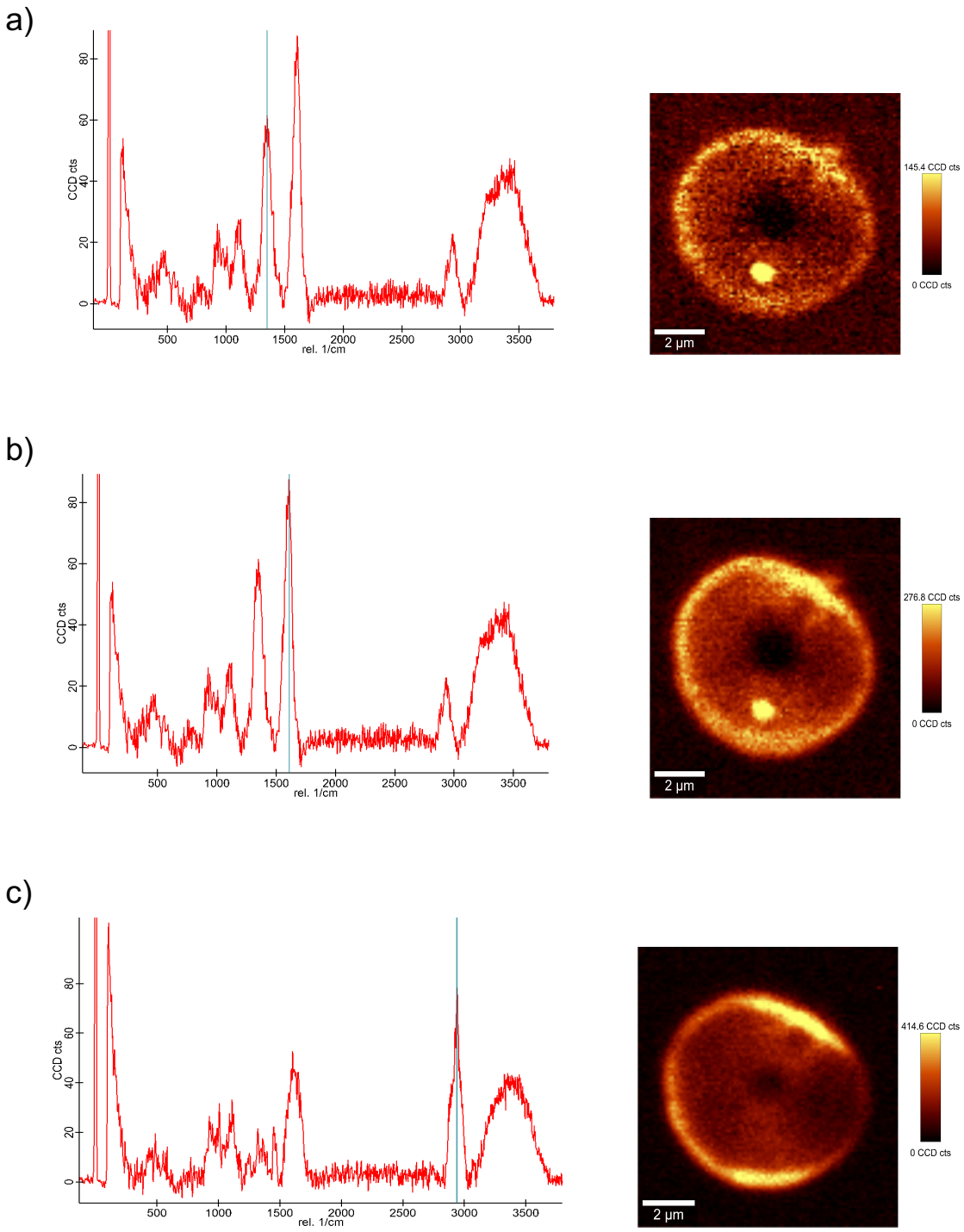

Figure 4.19 Single Raman spectra obtained using 532 nm excitation wavelength of a red blood cell treated with GO. The signal intensities were recorded at the following peaks a)1350 cm^{-1} b)1580 cm^{-1} and c)2940 cm^{-1} (left), with the corresponding Raman image scans (right).

4.4 Conclusions

Fluctuation spectroscopy was used to measure and extract values for the bending modulus in both red blood cells, and red blood cells treated with graphene oxide. The presence of 1 mg/ml graphene oxide suspension increased the bending modulus two-fold and is not temperature dependent. The bending modulus was calculated at several time points and showed no change. This implies graphene oxide adsorption occurs instantaneously. The good reproducibility of the results suggests fluctuation spectroscopy can provide a reliable method to quantitatively measure the effects of graphene oxide on the red blood cell and on the lipid bilayer mechanics. Absorbance analysis shows a decrease in the radius of red blood cell, in line with the radial analysis conducted during the fluctuation spectroscopy. With no change in absorbance, it is concluded that graphene oxide adsorbs to the red blood cell membrane, but does not lead to loss of haemoglobin, suggesting that it may not enter the penetrate the membrane. This is consistent with the limited information obtained using Raman imaging.

Chapter 5 Discussions, Conclusions and Further Work

This thesis employed a number of techniques to investigate the interaction of graphene with cell membranes. From analysing the interactions of graphene oxide with Langmuir monolayers of mixed lipid compositions, it was determined that the addition of graphene oxide increased the overall surface pressure of the monolayers, whilst also decreasing the compressibility. The insertion of GO is evident by the increase in trough area observed with GO addition. The nature of the interaction depended on the lipid composition of the monolayer. For the inner leaflet, initial GO insertion was dependent on pressure, with little GO insertion at the condensed pressure phase. The outer leaflet was more permeable to GO, suggesting a significant interaction between GO and the negatively charged PS head groups present in the inner leaflet mixture.

Permeability experiments using bilayer vesicles have shown GO to permeate vesicles, without causing full lysis. Using two preparations of vesicles, it has been found that permeability can be affected by the composition and properties of the vesicles, showing higher permeability with simple vesicles made with only one type of lipid. From using simple DOPC vesicles, it can be suggested that GO may have a specific interaction with PC head groups. Permeability has also been shown to be dependent on GO concentration, with an increase in permeability as a result of increasing GO concentration. Steady rates of permeation have been found over time, which could suggest GO saturates the vesicles, resulting in initial permeation with no further interactions.

Further investigation into GO interactions with model cells (RBCs) showed GO to be non-toxic resulting in no haemolysis of the cells, and in contrast to the vesicles we found no evidence of membrane penetration. Fluctuation spectroscopy analysis found GO to increase the bending modulus of RBC cell membranes, meaning the membrane became more rigid, probably because of the interactions observed in the Langmuir trough. Radial and absorbance analysis showed the adsorption of GO decreased the radius of the cell, suggesting possible loss in membrane surface area. The absorbance results also showed no loss of haemoglobin from the cells, suggesting GO does not

completely permeate the membrane, consistent with the results of Raman imaging.

GO has shown promise as a good biocompatible nanomaterial. The present results suggest that when GO interacts with biological cells it will interact with the outer leaflet of the membrane, but not the inner. Vesicle analysis also showed good permeability using vesicles composed of lipids found in the outer leaflet. No haemolysis was shown with RBCs indicating the membrane is not fully permeated, suggesting possible interactions with the outer leaflet of the membrane but not the inner. This provides further evidence of strong repulsive forces between GO and PS head groups. There is a decrease in the radius suggesting there could be loss of membrane area from the outer leaflet. GO has been shown to extract phospholipids from the membranes of *E.coli* (147). However, in this work lipid extraction from both inner and outer leaflet has been reported, resulting in complete loss of membrane integrity. The 'self-healing' property used to describe the action of permeated DOPC vesicles (117) could be considered as a possible mechanism for GO interactions with RBCs. It is possible the GO extracts lipids from the outer leaflet which then 're-seals' resulting in an increase in the bending modulus of the membrane.

Further investigation is required to determine how the GO interacts with the membrane, and whether, as we hypothesise, PS is the specific component of the lipid mixtures used in the present study which interacts with GO.

5.1 Future Work

5.1.1 Complementary Techniques for Langmuir Monolayer Studies

There are several techniques that can be used to further investigate the effects of the graphene oxide on the inner and outer membrane leaflet. Fluorescence microscopy using fluorescently labelled lipids provides a strong contrast between domains (148). Fluorescently labelled lipids can be incorporated into the lipid mixtures to allow visualisation of lipid domains and their spatial distribution within the monolayer. This technique could be used to determine whether any changes

in domain properties are observed after addition of GO. The domain structure of cell membranes is believed to be very important to their function so establishing whether this is disrupted by GO will be important in further assessing its biological properties.

Brewster angle microscopy (BAM) can also be used to detect domain structure, as well as observing phase changes and phase separation. It is a dark field microscopy technique (149) utilising polarised light to observe changes in the refractive index of the water subphase in the presence of lipid molecules which provides a contrast between lipid domains. An advantage of using this technique is that no addition of fluorescent lipids or probes to the monolayer is required, therefore giving a true representation of the lipid monolayer being studied. Further development of BAM has also lead to the accurate measurement of the tilt angles in lipid phases (150).

The Langmuir-Blodgett technique can also be used to deposit lipid monolayers with GO incorporated onto solid substrates to further probe the monolayer. Using techniques such as AFM can provide information of the morphology of the deposited film and can confirm whether GO has been incorporated into the monolayer. Due to the width of GO flakes, it has been proposed the GO will interact “edge-on”. Langmuir-Blodgett deposition could be used to confirm the orientation of the GO, and to help understand the mechanism in which GO inserts into the membrane.

5.1.2 Graphene Oxide Interaction with Phosphatidylserine

Several techniques used in this thesis can be applied to investigate GO interactions with PS head groups. A series of experiments investigating different compositions of bilayer vesicles can provide further evidence of GO permeability. Forming pure DOPS GUVs, as well as mixed vesicles containing PS lipids, will determine GO permeability, consequently giving information on its permeability towards the inner leaflet of the membrane. Fluctuation spectroscopy can also be used to determine whether GO affects the bilayer mechanics of the vesicles. Using this technique on a range of vesicles with different lipid compositions could distinguish specific interactions of GO with a specific lipid. Further Langmuir

monolayer analysis can also be used on one lipid systems to investigate the individual components of the inner/outer membrane leaflet.

5.1.3 Graphene Oxide Interaction with Proteins

Little is known about how GO may interact with the proteins of the cell membrane. It is possible to form vesicle and monolayer systems with integral trans-membrane proteins and/or membrane associated proteins, which would allow further characterisation of the physical effects of graphene oxide on the cell membrane using the techniques previously described in Chapters 2 and 3. The addition of proteins systematically to lipid systems can be used as a tool to investigate any specific interactions that may occur between GO.

One point for discussion was a previous study reporting GO to interact specifically with aquaporin proteins (a water channel protein) within cell membranes (145). To investigate this, vesicles can be constructed incorporating the protein into the bilayer to determine whether this increases membrane permeability, or in fact causes haemolysis according to the previous results. Interactions with the proteins of the RBC cytoskeleton are also of great interest to further research the interactions of GO with RBCs.

5.1.4 Complementary Techniques for Red Blood Cell Measurements

One of the questions unanswered in this thesis is the extent to which GO interaction disrupts the organisation of membrane lipids, in addition to its potential effect on domain structure as discussed above. There are a number of techniques which could be employed for this, which include: measuring the membrane dipole potential using ratiometric fluorescence imaging, and measuring the membrane surface electrostatic potential using a specific fluorescent probe that is sensitive to changes in charge density (151). These techniques could test our hypothesis of charge interactions between GO and PS head groups.

To assess the possibility GO may cause oxidative stress to RBCs, which has previously been associated with an increase in the bending modulus of RBC

membranes (131), the generation of reactive oxygen species (ROS) could be measured at the single cell level using oxidant-sensitive dyes (143) (59).

5.1.5 Interactions of Graphene Oxide with Endothelial and Epithelial Cells

To extend this research to other biological cells, to further investigate its biocompatibility, it would be interesting to study how graphene oxide interacts with cells with a more complex structure. An obvious starting point would be to look at endothelial and epithelial cells, a first point of contact for GO entering the body. Endothelial cells line the interior surface of blood vessels, forming an interface between circulating blood or lymph in the lumen and the rest of the vessel wall. Epithelial cells would be the first barrier for GO entering the lungs or digestive system.

BIBLIOGRAPHY

1. *Production, Properties and Potential of Graphene.* **Soldano, C., Mahmood, A., Dujardin, E.** 2010, Carbon, Vol. 48, pp. 2127-2150.

2. *Applications of Graphene in Electrochemical Sensing and Biosensing.* **Bahadir, E. B., Sezginturk, M. K.** 2016, Trends in Analytical Chemistry, Vol. 76, pp. 1-14.

3. *Electric Field Effect in Atomically Thin Carbon Films.* **Novoselov, K. S., Geim, A. K., Morosov, S. V., Jiang, D., Zhang, Y., Dubonos, S. V., Grigorieva, I. V., Firsov, A. A.** 2004, Science, Vol. 306, pp. 666-669.

4. *The Rise of Graphene.* **Geim, A. K., Novoselov, K. S.** s.l. : Nature Materials, 2007, Vol. 6, pp. 183-190.

5. *Experimental Observation of Quantum Hall Effect and Berry's Phase In Graphene.* **Zhang, Y. B., et al.** 2005, Nature, Vol. 438, pp. 201-204.

6. *Graphene: New Bridge Between Condensed Matter Physics and Quantum Electrodynamics.* **Katsnelson, M. I., Novoselov, K. S.** 2007, Solid State Commun, Vol. 143, pp. 3-13.

7. *Two-Dimensional Gas of Massless Dirac Fermions In Graphene.* **Novoselov, K. S., et al.** 2005, Nature, Vol. 438, pp. 197-200.

8. *The Structure of Suspended Graphene Sheets.* **Meyer, J. C., et al.** 2007, Nature, Vol. 446, pp. 60-63.

9. *Field Emission of Single-Layer Graphene Films Prepared by Electrophoretic Deposition.* **Wu, Z-S., et al.** 2009, Adv. Mater., Vol. 21, pp. 1756-1760.

10. **Sood, A. K., et al.** Review of Graphene Technology and Its Applications for Electronic Devices. *Graphene - New Trends and Developments.* s.l. : Intech.

11. *Graphene Based Electrochemical Sensors and Biosensors: A Review.* **Shao, Y., et al.** 10, 2010, Electroanalysis, Vol. 22, pp. 1027-1036.

12. *A Critical Review of Glucose Biosensors Based on Carbon Nanomaterials: Carbon Nanotubes and Graphene.* **Zhu, Z., et al.** 2012, Sensors, Vol. 12, pp. 5996-6022.

13. *Measurement of the Elastic Properties and Intrinsic Strength of Monolayer Graphene.* **Lee, C., Wei, X., Kysar, W. J., Hone, J.** 2008, Science, Vol. 321, pp. 385-388.

14. *Graphene and Graphene Oxide: Synthesis, Properties, and Applications.* **Zhu, Y., et al.** 2010, Adv. Mater., Vol. 22, pp. 3906-3924.
15. *Graphene as a flexible electronic material: mechanical limitations by defect formation and efforts to overcome.* **Lee, S-M., Kim, J-H., Ahn, J-H.** 6, 2015, Materials Today, Vol. 18, pp. 336-344.
16. *Effect of defects on the intrinsic strength and stiffness of graphene.* **Zandiatashbar, A., et al.** 3186, 2014, Nature Communications, Vol. 5, pp. 1-9.
17. *Wettability and Surface Free Energy of Graphene Films.* **Wang, S., Zhang, Y., Abidi, N., Cabrales, L.** 18, 2009, Langmuir, Vol. 25, pp. 11078-11081.
18. *Wettability of Graphene.* **Parobek, D., Liu, H.** 2015, 2D Mater., Vol. 2, p. 032001.
19. *Tailoring the hydrophobicity of graphene for its use as nanopores for DNA translocation.* **Schneider, G. F., et al.** 2013, Nature Communications, Vol. 4, pp. 1-7.
20. *A Roadmap for Graphene.* **Novoselov, K. S., Fal'ko, V. I., Colombo, L., Gellert, P. R., Schwab, M. G., Kim, K.** 2012, Nature, Vol. 490, pp. 192-200.
21. *Roll-to-roll production of 30-inch graphene films for transparent electrodes.* **Bae, S. et al.** 2010, Nature Nanotechnology, Vol. 5, pp. 574-578.
22. *Preparation of Graphitic Oxide.* **Hummers, W. S., Offeman, R. E.** 6, 1958, J. Am. Chem. Soc., Vol. 80, p. 1339.
23. *Atomic and electronic structure of graphene-oxide.* **Mkhoyan, A. K., Contryman, W. A., Silcox, J., Stewart A. D., Eda, G., Mattevi, C., Miller, S., Chhowalla, M.** 3, 2009, Nano Lett, Vol. 9, pp. 1058-1063.
24. *The reduction of graphene oxide.* **Pei, S., Cheng, H-M.** 9, 2012, Carbon, Vol. 50, pp. 3210-3228.
25. *Evolution of Surface Functional Groups in a Series of Progressively Oxidised Graphite Oxides.* **Szabo, T., et al.** 11, 2006, Chem. Mater. , Vol. 18, pp. 2740-2749.
26. *Structure of Graphite Oxide Revisited.* **Lerf, A., He, H., Forster, M., Klinowski, J.** 1998, J. Phys. Chem. B., Vol. 102, pp. 4477-4482.
27. *A New Structural Model for Graphite Oxide.* **He, H., Klinowski, J., Forster, M., Lerf, A.** 1998, Chemical Physical Letters, Vol. 287, pp. 53-56.
28. *Recent Advances in Graphene-Based Biosensors.* **Kuila, T., Bose, S., Khanra, P., Mishra, A. K., Kim, N. H., Lee J. H.** 2011, Biosensors and Bioelectronics, Vol. 26, pp. 4637-4648.

29. *Electronic properties of high oriented pyrolitic graphite: Recent discoveries.* **Pantin, V., et al.** 2006, Journal of Physics and Chemistry of Solids, Vol. 67, pp. 546-551.
30. *Understanding the intrinsic water wettability of graphite.* **Kozbial, A., et al.** 2014, Carbon, Vol. 74, pp. 218-225.
31. *Superhydrophobic to Superhydrophilic Wetting Control in Graphene Films.* **Rafiee, J., et al.** 2010, Adv. Mater., Vol. 22, pp. 2151–2154.
32. *Novel Method for Grafting Alkyl Chains onto Glassy Carbon. Application to the Easy Immobilization of Ferrocene Used as Redox Probe.* **Jouikov, V., Simonet, J.** 2012, Langmuir, Vol. 28, pp. 931-938.
33. *The preferential electrocatalytic behaviour of graphite and multiwalled carbon nanotubes on enediol groups and their analytical implications in real domains.* **Crevillen, G. A., Pumera, M., Gonzalez, M. C., Escarpa, A.** 2009, Analyst, Vol. 134, pp. 657-662.
34. *Electrochemistry Using Self-Assembled DNA Monolayers on Highly Oriented Pyrolytic Graphite.* **Gorodetsky, A. A., Barton, J. K.** 2006, Langmuir, Vol. 22, pp. 7917-7922.
35. *Reduction of Dioxygen Catalyzed by Pyrene-Wired Heme Domain Cytochrome P450 BM3 Electrodes.* **Udit, A. K., et al.** 2004, J. Am. Chem. Soc., Vol. 126, pp. 10218-10219.
36. **McDermott, T. M., Kneten, K., McCreery, L. R.** 1992, J. Phys. Chem., Vol. 96, pp. 3124-3130.
37. A New View of Electrochemistry at Highly Oriented Pyrolytic Graphite. **Patel, A. N., et al.** 2012, J. Am. Chem. Soc., Vol. 134, pp. 20117-20130.
38. Thin-Film Diamond Part B. **Haenni, W., Rychen, P., Fryda, M., Comninellis, C.** 2004, Semiconductors and Semimetals series, p. 149.
39. Co-Doping of Diamond with Boron and Sulfur. **Eaton, C. S., et al.** 2002, Electrochem. SolidState Lett., Vol. 5, pp. G65-G68.
40. UPS of Boron-Sulfur Co-Doped N-Type Diamond Electrodes. **Vaddiraju, S., Eaton-Magana, S., Chaney, A. J., Sunkara, K. M.** 2004, Electrochem. Solidstate Lett., Vol. 7, pp. G331-G334.
41. Characterization of heavily boron-doped diamond films. **Zhang, R. J., Lee, S. T., Lam, Y. W.** 11, 1996, Diamond and Related Materials, Vol. 5, pp. 1288-1294.
42. Doped Diamond: A Compact Review on a New, Versatile Electrode Material. **Kraft, A.** 2007, Int. J. Electrochem. Sci., Vol. 2, pp. 355-385.

43. Application of diamond electrodes to electrochemical processes. **Panizza, M., Cerisola, G.** 2005, Electrochemica. Acta., Vol. 51, pp. 191-199.

44. https://avantilipids.com/. [Online] Avanti Polar Lipids, Inc. .

***45.** A Correlation Between Lipid Domain Shape and Binary Phospholipid Mixture Composition in Free Standing Bilayers: A Two-photon Fluorescence Microscopy Study.* **Bagatolli, L., Gratton, E.** 1, 2000, Biophysical Journal, Vol. 79, pp. 434-447.

***46.** The State of Lipid Rafts: From Model Membranes to Cells. .* **Edidin, M.** 2003, Annual Review of Biophysics and Biomolecular Structures, Vol. 32, pp. 257-283.

***47.** The Fluid Mosaic Model of the structure of cell membranes.* **Singer, S. J., Nicolson, G. L.** 1972, Science, Vol. 175, pp. 720-731.

***48.** Membrane structure.* **Robertson, J. D.** 1981, J. Cell. Biol., Vol. 91, pp. 191s-204s.

***49.** Current models for the structure of biological membranes.* **Stoeckenius, W., Engelman, D. M.** 1969, J. Cell. Biol., Vol. 42, pp. 613-646.

***50.** Membrane structure: some general principals.* **Bretscher, M. S.** 1973, Science, Vol. 181, pp. 622-829.

***51.** Fast flip-flop of cholesterol and fatty acids in membranes: implications for membrane transport proteins.* **Hamilton, A. J.** 2003, Curr. Opin. Lipidol., Vol. 14, pp. 263-271.

***52.** A microscopic interaction model of maximum solubility of cholesterol in lipid bilayers.* **Huang, J., Feigenson, W. G.** 1999, Biophys. J., Vol. 76, pp. 2142–2157.

***53.** Ceramide drives cholesterol out of the ordered lipid bilayer phase into the crystal phase in 1 - palmitoyl - 2 - oleoyl - sn - glycero - 3 - phosphocholine / cholesterol / ceramide ternary mixtures.* **Ali, R. M., Cheng, H. K., Huang, J.** 2006, Biochemistry, Vol. 45, pp. 12629–12638.

***54.** Physical Properties of Surfactant Bilayer Membranes: Thermal Transitions, Elasticity, Rigidity, Cohesion, and Colloidal Interactions.* **Evans, E., Needham, D.** 1987, J. Phys. Chem., Vol. 91, pp. 4219-4228.

***55.** Toxicity of Graphene and Graphene Oxide Nanowalls Against Bacteria.* **Akhavan, O., Ghaderi, E.** 10, 2010, ACS Nano, Vol. 4, pp. 5731-5736.

***56.** Graphene-Based Antibacterial Paper.* **Hu, W., Peng, C., Luo, W., Lv, M., Li, X., Li, D., Huang, Q., Fan, C.** 7, 2010, ACS Nano, Vol. 4, pp. 4317-4323.

57. *Antibacterial Efficiency of Graphene Nanosheets against Pathogenic Bacteria via Lipid Peroxidation.* **Krishnamoorthy, K., Veerapandian, M., Zhang, L-H., Yun, K., Kim, S-J.** 2012, J. Phys. Chem., Vol. 116, pp. 17280-17287.

58. *What is Oxidative Stress?* **Betteridge, D. J.** 2000, Metabolism , Vol. 49, pp. 3-8.

59. *In vitro toxicity evaluation of graphene oxide on A549 cells.* **Chang, Y., et al.** 2011, Toxicology Letters, Vol. 200, pp. 201-210.

60. *Cytotoxicity of Graphene Oxide and Graphene in Human Erythrocytes and Skin Fibroblasts.* **Liao, K-H., Lin, Y-S., Macosko, C. W., Haynes, C. L.** 2011, ACS. Appl. Mater. Interfaces, Vol. 3, pp. 2607-2615.

61. *Recent Advances in Electrochemical Biosensors Based on Graphene Two-Dimensional Nanomaterials.* **Song, Y., Luo, Y., Zhu, C., Li, H., Du, D., Lin, Y.** 2016, Biosensors and Bioelectronics, Vol. 76, pp. 195-212.

62. *Electrical Detection of DNA Hybridization with Single-Base Specificity using Transistors based on CVD-Grown Graphene Sheets.* **Dong, X., Shi, Y., Huang, W., Chen, P., Li, L-J.** 2010, Adv. Mater., Vol. 22, pp. 1649-1653.

63. *Graphene Platform for Hairpin-DNA-Based Impedimetric Geosensing.* **Bonnani, A., Pumera, M.** 3, 2011, ACS Nano, Vol. 5, pp. 2356-2361.

64. *Glucose Oxidase - An Ideal Enzyme.* **Wilson, R., Turner, A. P. F.** 1992, Biosens. Bioelectron. , Vol. 7, pp. 165-185.

65. *Graphene Fluorescence Resonance Energy Transfer Aptasensor for the Thrombin Detection.* **Chang, H., Tang, L., Wang, Y., Jiang, J., Li, J.** 2010, Anal. Chem., Vol. 82, pp. 2341-2346.

66. *Flow Sensing of Single Cell by Graphene Transistor in a Microfluidic Channel.* **Ang, P. K., et al.** 2011, Nano. Lett., Vol. 11, pp. 5240-5246.

67. *Pyrene-Wired Antibodies on Highly Ordered Pyrolytic Graphite as a Label-Free Impedance Biosensor for the Sepsis Biomarker Procalcitonin.* **Mahe, L. S. A., Green, S. J., Winlove, C. P., Jenkins, A. T. A.** 2014, J. Solid State Electrochem., Vol. 18, pp. 3245-3249.

68. *DNA-Mediated Electrochemistry of Disulfides on Graphite.* **Gorodetsky, A. A., Barton, J. K.** 2007, J. Am. Chem. Soc., Vol. 129, pp. 6074-6075.

69. *Electrochemical Biosensor Based on Boron-Doped Diamond Electrodes with Modified Surfaces.* **Yu, Y., Zhou, Y., Wu, L., Zhi, J.** 2012, International Journal of Electrochemistry, pp. 1-10.

70. *Boron-doped diamond nano/microelectrodes for bio-sensing and in vitro measurements.* **Dong, H., et al.** 2015, Front Biosci. (Schol. Ed.). , Vol. 3, pp. 518-540.

71. *Physical Properties of Lipid Bilayer Membranes: Relevance to Membrane Biological Functions.* **Subczynski, W., Wisniewska, A.** 2000, Acta. Biochimica. Polonica. , Vol. 47, pp. 613-625.

72. *Effect of cholesterol nanodomains on monolayer morphology and dynamics.* **Kim, K., et. al.** 2013, PNAS, pp. E3054–E3060.

73. *Phase Behavior of Lipid Monolayers Containing DPPC and Cholesterol Analogs.* **Stottrup, B. L., Keller, S. L.** 2006, Biophysical Journal, Vol. 90, pp. 3176–3183.

74. *Cholesterol Stabilizes the Crystal-Liquid Interface in Phospholipid Monolayers.* **Weis, R. M., McConnell, H. M.** 1985, J. Phys. Chem., Vol. 89, pp. 4453-4459.

75. *On Biomolecular Layers of Lipoids on the Chromocytes of the Blood.* **Gortel, E., Grendel, F.** 1925, J. Exp. Med. , Vol. 41, p. 439.

76. *The role of lipids in pulmonary surfactant.* **Veldhuizen, R., et al.** 2-3, 1998, Biochimica et Biophysica Acta, Vol. 1408, pp. 90-108.

77. *Langmuir monolayers and Differential Scanning Calorimetry for the study of the interactions between camptothecin drugs and biomembrane models.* **Casado, A., et al.** 2016, Biochimica et Biophysica Acta, Vol. 1858, pp. 422-433.

78. *Cholesterol Modifies Huntingtin Binding to, Disruption of, and Aggregation on Lipid Membranes.* **Gao, X., et al.** 2016, Biochemistry, Vol. 55, pp. 92-102.

79. *Seeding "one dimensional crystallization" of amy- loid: a pathogenic mechanism in Alzheimer's and scrapie.* **Jarret, J. T., Lansbury Jr, P. T.** 1993, Cell, Vol. 73, pp. 1055-1058.

80. *Surface Chemistry of Alzheimer's Disease: A Langmuir Monolayer Approach.* **Thakur, G., Micic, M., LeBlanc, R. M.** 2009, Colloids and Surfaces B: Biointerfaces, Vol. 74, pp. 436 – 456.

81. *Surface Chemistry and Spectroscopy of the β-Galactosidase Langmuir Monolayer.* **Crawford, F. N., Micic, M., Orbulesco, J., LeBlanc, R. M., Weissbart, D.** 2015, Journal of Colloid and Interface Science, pp. 1-19.

82. *Surface Chemistry and Spectroscopy of Human Insulin Langmuir Monolayer.* **Johnson, S., et al.** 2012, Journal of Physical Chemistry, Vol. 116, pp. 10205 – 10212 .

83. *Structure and phase transitions in Langmuir monolayers.* **Kaganer, V. M., Mohwald, H., Dutta, P.** 3, 1999, Rev. Mod. Phys., Vol. 71, pp. 779-819.

84. *Physical Chemistry of Surfaces.* **Adamson, A.** 1967, Interscience Publishers.

85. *Dynamical measurements of dilational properties of a liquid interface.* **Lucassen, J., van der Tempel, M.** 1972, Chem. Eng. Sci. , Vol. 27, pp. 1283-1291.

86. *Head Groups of Lipids Govern the Interaction and Orientation between Graphene Oxide and Lipids.* **Li, S., et al.** 2013, J. Phys. Chem. C, Vol. 117, pp. 16150-16158.

87. *Reduced Graphene Oxide as the Support for Lipid Bilayer Membrane.* **Tsuzuki, K., et al.** 2012, Journal of Physics: Conference Series, Vol. 352, p. 012016.

88. *A Bioelectronic Platform Using a Graphene Lipid Bilayer Interface.* **Ang, P. K., et al.** 12, 2010, ACS Nano, Vol. 4, pp. 7387-7394.

89. *Solvent-Assisted Lipid Bilayer Formation on Silicon Dioxide and Gold.* **Tabaei, S. R., et al.** 34, 2014, Langmuir, Vol. 30, pp. 10363-10373.

90. *A Review of Membrane-Based Biosensors for Pathogen Detection.* **van den Hurk, R., Evoy, S.** 2015, Sensors, Vol. 15, pp. 14045-14078.

91. *Phospholipid−Graphene Nanoassembly as a Fluorescence Biosensor for Sensitive Detection of Phospholipase D Activity.* **Liu, S-J., et al.** 2012, Anal. Chem., Vol. 84, pp. 5944-5950.

92. **Langmuir, I., Schaefer, V. J. s.l. :** Journal of American Chemical Society, 1938, Vol. 60, pp. 1351-1360.

93. *Langmuir-Blodgett Deposition Ratios.* **Honig, E. P., et al.** 1, 1973, Journal of Colloid and Interface Science, Vol. 45, pp. 92-102.

94. *Graphene Oxide Dispersions in Organic Solvents.* **Parades, J. I., et al.** 2008, Langmuir, Vol. 24, pp. 10560-10564.

95. *Synthesis and exfoliation of isocyanate-treated graphene oxide nanoplatelets.* **Stankovich, S. et al.** 2006, Carbon, Vol. 44, pp. 3342-3347.

96. *Effect of graphene oxide doping on superconducting properties of bulk MgB2.* **Bhalothia, S., et al.** 2013, Superconductor Science and Technology, Vol. 26, p. 095008.

97. *Structure and fluctuations of charged phosphatidylserine bilayers in the absence of salt.* **Petrache, H. L., et al.** 2004, Biophysical Journal, Vol. 86, pp. 1574-1586.

98. *Order and Interactions in Model Biological Membranes.* **Thompson, J.** 2006, PhD. Thesis, University of Exeter, Exeter, UK.

99. *Reduced graphene oxide directed self-assembly of phospholipid monolayers in liquid and gel phases.* **Rui, L.** 2015, Biochimica et Biophysica Acta, Vol. 1848, pp. 1203–1211.

100. *Visible-light sensitization of boron-doped nanocrystalline diamond through non-covalent surface modification.* **Krysova, H., et al.** 2015, Phys. Chem. Phys. Chem., Vol. 17, pp. 1165-1172.

101. *A Comparative ATR-Wettability Study of Langmuir-Blodgett and Adsorbed Films on Flat Substrates and Glass Microbeads.* **Maoz, R., Sagiv, J.** 1984, Journal of Colloid and Interface Science, Vol. 100, pp. 465-496.

102. **Bard, A. J., Rubinstein, I.** Electroanalytical Chemistry: A Series of Advances. New York : Marcel Dekker, 2003. p. 213. Vol. 22.

103. *Giant Vesicles: Preparations and Applications.* **Walde, P., et al.** 2010, ChemBioChem, Vol. 11, pp. 848-865.

104. *Liposome Electroformation.* **Angelova, I. M., Dimitrov, S. D.** 1986, Farad.Disc.Chem.Soc., Vol. 81, pp. 303-311.

105. *Preparation of giant vesicles by external ac electric-fields - kinetics and applications.* **Angelova, M. I., et al.** 1992, Progr. Colloid. Polym. Sci., Vol. 89, pp. 127-131.

106. *Physical basis of self-organization and function of membranes: Physics of vesicles.* **Sackmann, E.** 1995, Elsevier Science Publishers B. V., pp. 213-303.

107. *Budding and Fission of Vesicles.* **Dobereiner, H. G., et al.** 1993, Biophysical Jounral, Vol. 65, pp. 396-403.

108. *Spontaneous curvature of fluid vesicles induced by trans-bilayer sugar asymmetry.* **Dobereiner, H. G., et al.** 1999, European Biophysical Jounal, pp. 174-178.

109. *Budding transitions of fluid-bilayer vesicles: the effect of area-difference elasticity.* **Miao, L., et al.** 1994, Physical Review E, Vol. 49, pp. 5389-5407.

110. *Shape deformation of ternary vesicles coupled with phase separation.* **Yanagisawa, M., et al.** 2008, Phys. Rev. Lett. , Vol. 100, p. 148102.

111. *Protein–protein and protein–lipid interactions in domain-assembly: Lessons from giant unilamellar vesicles.* **Kahya, N.** 2010, Biochimica et Biophysica Acta, Vol. 1798, pp. 1392-1398.

112. *Elastic properties of lipid bilayers: theory and possible experiments.* **Helfrich, W.** 11, 1973, Zeitschrift für Naturforschung. Teil C: Biochemie, Biophysik, Biologie, Virologie, Vol. 28, pp. 693-703.

113. *Dependence of norfloxacin diffusion across bilayers on lipid composition.* **Purushothaman, S., Cama, J., Keyser, U. F.** 2016, Soft Matter, Vol. 12, pp. 2135-2144.

114. *Investigating the lytic activity and structural properties of Staphylococcus aureus phenol soluble modulin (PSM) peptide toxins.* **Laabei, M., et al.** 2014, Biochimica et Biophysica Acta, Vol. 1838, pp. 3153 – 3161.

115. *Evidence That Clustered Phosphocholine Head Groups Serve as Sites for Binding and Assembly of an Oligomeric Protein Pore.* **Valeva, A., et al.** 36, 2006, The Journal of Biological Chemistry, Vol. 281, pp. 26014-26021.

116. *Molecular Architecture and Functional Analysis of NetB, a Pore-forming Toxin from Clostridium perfringens.* **Savva, C. G., et al.** 5, 2013, J. Biol. Chem. , Vol. 288, pp. 3512-3522.

117. *Interactions of Graphene Oxide with Model Cell Membranes: Probing Nanoparticle Attachment and Lipid Bilayer Disruption.* **Liu, X., Chen, K. L.** 2015, Langmuir, Vol. 31, pp. 12076-12086.

118. *Cascades of transient pores in giant vesicles: Line tension and transport.* **Karatekin, E., et al.** 2003, Biophys J. , Vol. 84, pp. 1734-1749.

119. *Influence of lipid composition on physicochemical properties of nanoliposomes encapsulating natural dipeptide anti- oxidant L-carnosine.* **Maherani, B., et al.** 2012, Food Chem, Vol. 134, pp. 632-640.

120. *Red blood cell membrane disorders.* **Tse, W. T., Lux, S. E.** 1, 1999, British Journal of Haemotology, Vol. 104, pp. 2-13.

121. *The sickle syndrome. In: Haldin, RI, Lux SE and Stossel TP (Eds.).* **Platt, O.** S. Philadelphia, PA: Lippincott : s.n., 1995, Blood: Principles and Practice of Hematology, pp. 1592-1700.

122. *Regulation of red cell membrane protein interactions: Implications for red cell function.* **Takakuwa, Y.** 2, 2001, Current Opinion in Hematol., Vol. 8, pp. 80-84.

123. *Molecular maps of red cell deformation: Hidden elasticity and in situ connectivity.* **Discher, D. E., Mohandas, N., Evans, E. A.** 1994, Science, Vol. 266, pp. 1032-1035.

124. *Mechanics of the human red blood cell deformed by optical tweezers.* **Dao, M., Lim, C. T., Suresh, S.** 2003, Journal of the Mechanics and Pysics of Solids, Vol. 51, pp. 2259-2280.

125. *Frequency spectrum of the flicker phenomenon in erythrocytes.* **Brochard F., Lennon, J. F.** 1975, J Phys-Paris, Vol. 36, pp. 1035-1047.

126. *Flicker in erythrocytes. "vibratory movements in the cytoplasm"?* **Parpart, A. K., Hoffman, J. H. F.** 2, 1956, Journal of Cellular Physiology, Vol. 472, pp. 295-303.

127. *Configurations of fluid membranes and vesicles.* **Seifert, U.** 1997, Advances in Physics, Vol. 46, pp. 13-137.

128. *Mechanics of the Cell.* **Boal, D.** 2002, Cambridge University Press.

129. *Bending elastic moduli of lipid bilayers: modulation by solutes.* **Duwe, H., Kaes, J., Sackmann, E.** 1990, J. Phys. France, Vol. 51, pp. 945-962.

130. *Advanced Flicker Spectrocopy of Fluid Membranes.* **Dobereiner, H-G., et al.** 4, 2003, Physical Review Letters, Vol. 91, p. 048301.

131. *Effect of Hydroperoxides on Red Blood Cell Membrane Mechanical Properties.* **Hale, J. P., Winlove, C. P., Petrov, P. G.** 2011, Biophysical Journal, Vol. 101, pp. 1921-1929.

132. *Bilayer bending elasticity measured by fourier analysis of thermally excited surface undulations of flaccid vesicles.* **Engelhardt, H., Duwe, H. P., Sackmann, E.** 8, 1985, Journal de Physique Lettres, Vol. 46, pp. 395-400.

133. *The thermal fluctuations of red blood cells.* **Hale, J.** 2009, PhD. Thesis, University of Exeter, Exeter, UK.

134. *Refined contour analysis of giant unilamellar vesicles.* **Pécréaux, J., et al.** 2004, Eur. Phys. J. E , Vol. 13, pp. 277-290.

135. *Absorption spectra of human fetal and adult oxyhemoglobin, de-oxyhemoglobin, carboxyhemoglobin, and methemoglobin.* **Zijlstra, W. G., Buursma, A., Meeuwsen-van der Roest, W. P.** 9, 1991, Clin. Chem., Vol. 37, pp. 1663-8.

136. *Raman Spectra of Graphite Oxide and Functionalized Graphene Sheets.* **Konstantin, N. K., et al.** 1, 2008, Nano Lett. , Vol. 8, pp. 36-41.

137. *Raman excitation wavelength investigation of single red blood cells in vivo.* **Wood, B. R., McNaughton, D.** 2002, Journal of Raman Spectroscopy, Vol. 33, pp. 517-523.

138. *Resonance Raman spectroscopy of red blood cells using nearinfrared laser excitation.* **Wood, B. R., et al.** 2007, Anal Bioanal Chem, Vol. 387, pp. 1691-1703.

139. *Distribution and biocompatibility studies of graphene oxide in mice after intravenous administration.* **Zhang, X., et al.** 2011, Carbon, Vol. 49, pp. 986-995.

140. *On the shape of human red blood cells interacting with flat artificial surfaces--the 'glass effect'.* **Eriksson, L. E.** 3, s.l. : Biochim Biophys Acta, 1990, Vol. 1036, pp. 193-201.

141. *Theoretical and phase contrast microscopic eigenmode analysis of erythrocyte flicker: amplitudes.* **Peterson, M. A., Strey, H., Sackmann, E.** 1992, J. Phys. II France, Vol. 2, pp. 1273-1285.

142. *Measurement of erythrocyte membrane elasticity by flicker eigenmode decomposition.* **Strey, H., Peterson, M. A., Sackmann E.** 1995, Biophys. J., Vol. 69, pp. 478-488.

143. *Oxidative stress-mediated antibacterial activity of graphene oxide and reduced graphene oxide in Pseudomonas aeruginosa.* **Gurunathan, S. et al.** 2012, International Journal of Nanomedicine, Vol. 7, pp. 5901-5914.

144. *Bending Rigidity and Gaussian Bending Stiffness of Single-Layered Graphene.* **Wei, Y., et al.** 2013, Nano Lett., Vol. 13, pp. 26-30.

145. *Vacuolization in Cytoplasm and Cell Membrane Permeability Enhancement Triggered by Micrometer-Sized Graphene Oxide.* **Wu, C., et al.** 8, 2015, ACS Nano, Vol. 9, pp. 7913-7924.

146. *Identification, Purification, and Partial Characterization of a Novel Mr 28,000 Integral Membrane Protein from Erythrocytes and Renal Tubules.* **Denker, B. M., et al.** 1988, J. Biol. Chem. , Vol. 263, pp. 15634 –15642.

147. *Destructive extraction of phospholipids from Escherichia coli membranes by graphene nanosheets.* **Tu, Y., et al.** 2013, Nature Nanotechnology, Vol. 8, pp. 594-602.

148. *Characterisation of of lipid domains in erythrocyte membranes.* **Rodgers, W., Glaser, M.** 1991, Proc. Natl. Acad. Sci. USA, Vol. 88, pp. 1364-1368.

149. *Microscope at the brewster angle: Direct observation of first-order phase transitions in monolayers.* **Henon, S. Meunier, J.** 4, 1991, Review of Scientific Instruments, Vol. 62, pp. 936-939.

150. *Determination of alkyl chain tilt angles in Langmuir monolayers: A comparison of brewster angle autocorrelation spectroscopy and x-ray diffraction.* **Lautz, C., et al.** 11, 1998, Journal of Chemical Physics, Vol. 108, pp. 4640-4646.
151. *Red Blood Cell Susceptibility to Pneumolysin: Correlation with Membrane Biochemical and Physical Properties.* **Bokori-Brown, M., et al.** 2016, The Journal of Biological Chemistry, pp. 1-38.
152. *Factors Controlling the Electrodeposition of Metal Nanoparticles on Pristine Single Walled Carbon Nanotubes.* **Day, T. M., Unwin, P. R., Macpherson, J. V.** 1, 2007, Nano. Lett., Vol. 7, pp. 51-57.